Dynamics of Particle Precipitation in the Auroral Ionosphere

Paul Wild MPhys (Hons)

A Thesis
Submitted for the Degree of
Doctor of Philosophy

AUGUST, 2011

Space Plasma Environment and Radio Science Group
Department of Physics
Lancaster University
Lancaster, UK

Dynamics of Particle Precipitation in the Auroral Ionosphere

A Thesis
Submitted for the Degree of
Doctor of Philosophy

by

Paul Wild, MPhys (Hons)

Abstract

Energetic electrons deposit significant amounts of energy into the ionosphere during precipitation events. Riometers provide a means of monitoring this precipitation by measuring the associated cosmic noise absorption. Individually however they cannot provide any details about the energies of the precipitating electrons. The first study in this thesis looks at estimating the characteristic energy of the precipitating electrons by the means of two imaging riometers with overlapping fields of view. Two methods of calculating the height of maximum cosmic noise absorption are developed, a method of height triangulation and tomographic reconstruction of the absorption events. These methods show a marked improvement when compared with a previously published method. A case study comparing the calculated height of maximum cosmic noise absorption with a deduced absorption profile from an EISCAT electron density profile shows good correlation. Using the height of maximum cosmic noise absorption estimates are made of the characteristic energy for three case studies; a morning absorption event, a substorm spike and an afternoon absorption event. The estimated energies for these events were 5keV, 17-20keV and 100+keV respectively.

The second study concerns the statistics and mechanisms of daytime absorption events. Statistics of absorption during the course of a day show a deep minimum during the afternoon sector. However there are a number of discrete cases that do occur during this afternoon minimum. A statistical analysis of the time period, 12-16UT at Kilpisjärvi is undertook. They are found to be short lived, highly localised events. This is in agreement with previous studies. They tend to occur during periods of weak geomagnetic activity. A portion of these are found to be early onset substorms, and account for 7.4% of the events. To understand the mechanisms behind the rest of the events one year of data was analyised in greater detail. A portion of these events seem to agree with previous studies, that these events are reltavistic preciptiation events caused by **E**lectro**M**agnetic **I**on **C**yclotron (EMIC) wave scattering. However a greater number of the events seem to be due to the precipitation of lower energy electrons during dispersed electron injections of the radiation belts; a more localized and later occurring version of morning absorption caused by the eastward drift and scattering of lower energy (10-100keV) substorm injected electrons.

Contents

List of Figures

Acknowledgments

Firstly I would like to thank my supervisor Professor Farideh Honary for the opportunity to study for this PhD, the guidance and support given over the four years.

Secondly I would like to thank Andrew Kavanagh, without whose support, help and guidance I would not have been able to complete this thesis. Andrew Senior for the answers to the many maths and science questions I had. Steve Marple for his computer and riometer help and to the rest of the members of the Space Plasma Environment and Radio Science group.

I would also like to thank STFC for the funding to complete my studies.

Special thanks goes to my parents for the unwaivering support and confidence in my abilities.

And finally thanks to my friends for their support, for always being able to put a smile on my face and for keeping me in high spirits.

Declaration

I declare that the thesis is my own work, and has not been submitted in substantially the same form for the award of a higher degree elsewhere. Some research has led to the publication of the following scientific paper in a referred journal:

Wild, P. F. Honary, A.J. Kavanagh and A. Senior. (2010) Triangulating the height of cosmic noise absorption: A method for estimating the characteristic energy of precipitating electrons. *Journal of Geophysical Research, 115,* A12326, doi:10.1029/2010JA015766.

Chapter 1

The Solar Terrestrial Environment

1.1 Introduction

The solar-terrestrial environment refers to parts of the Earth's atmosphere, ionosphere and magnetosphere as well as the Sun, solar emissions and solar wind. The study of the solar-terrestrial environment is primarily concerned with observing the interactions between charged energetic particles, electric fields, magnetic fields and the resulting effects. The study of the solar-terrestrial environment is old, originating in the 19th century, with observations of solar activity, for example, through the measurement of sunspot number and the relationship with magnetic disturbances on the Earth's surface. The advent of new technologies in the twentieth century such as radar and satellite observations has allowed for greater progress in research and understanding of this complex and dynamic system.

This chapter aims to introduce and outline the fundamental concepts and processes of the solar-terrestrial environment from the Sun, through to the Earth's ionosphere.

1.2 The Sun

The Sun, (pictured in figure 1.1) at an age of over 4.5 billion years bathes the Earth and the solar system with its radiative glow, emitting 4×10^{26} W of electromagnetic radiation. At a distance of 1.4597×10^{11} m from the Earth the Sun is a giant ball (radius of 696,000 km) of plasma held together by its own gravitational force. The solar interior is composed of hydrogen (90%) and helium (10%) with heavier elements such as carbon, nitrogen and oxygen making up 0.1% of the mass of the Sun.

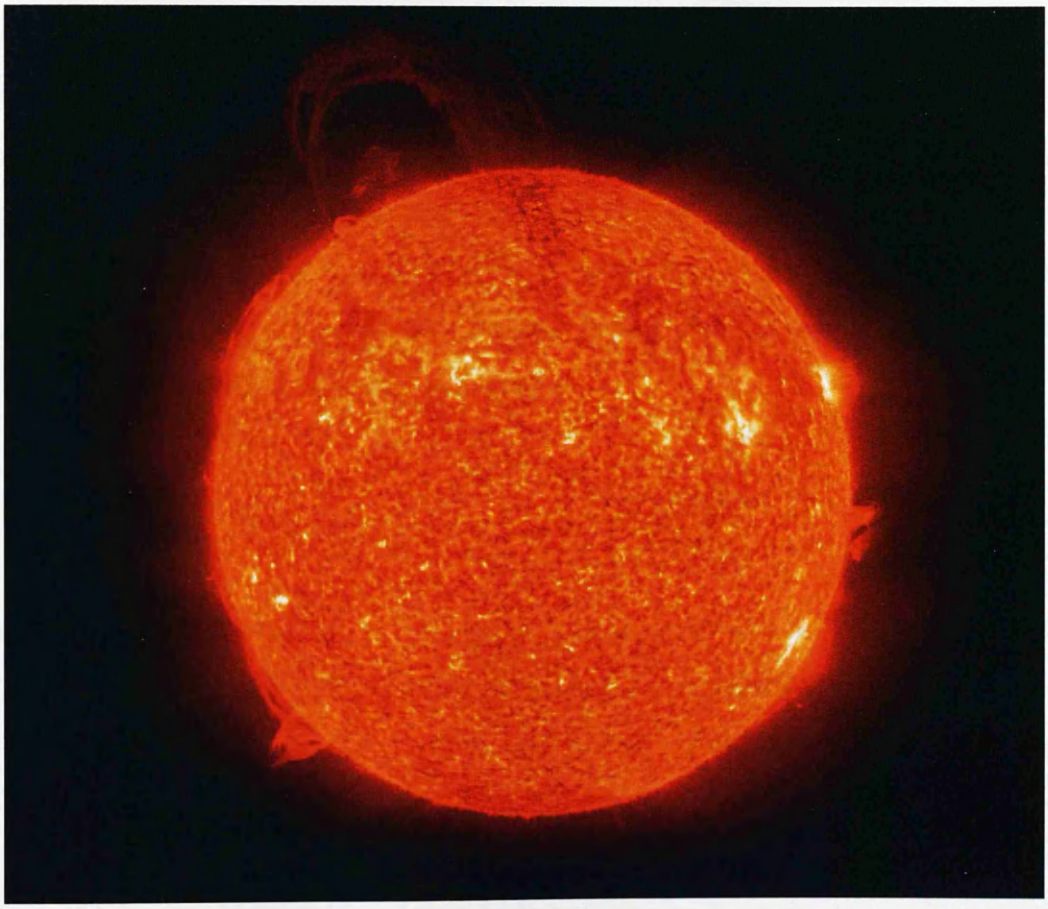

Figure 1.1: Ultraviolet image of the Sun taken from the SOHO satellite.

At the center of the Sun is the core, a solidly rotating mass with a temperature exceeding 16 million Kelvin. The core extends from the center of the Sun to 0.25

solar radii ($R_\odot$). It is here that the Sun's energy is generated by nuclear fusion; converting hydrogen into helium. Between 0.27-0.7$R_\odot$ is the radiative zone, energy from the core is transferred by radiation here. This radiation undergoes numerous scattering meaning energy transfer is extremely slow. Between 0.7-1$R_\odot$ is the convection zone. The temperature decrease in the convection zone is so great (from 5×10^5k to 6×10^3k) that it causes unstable and turbulent convection. The convection zone has a differential rotation with a period of 26 days near the equator to 37 days near poles. (*Yohsuke and Abraham* (2007)).

The solar atmosphere is composed of three layers: the photosphere, chromosphere and corona. The photosphere is the uppermost layer of the convection zone. Covered in granulation due to the turbulent convection this is where most of the visible light from the Sun originates. The lowest temperature in the photosphere is around 4.2×10^3k. The chromosphere and corona lie above the photosphere. The chromosphere has a density of $10^{15}m^{-3}$. The temperature gradually increases from the photosphere and can reach 2×10^6k kelvin. The corona extends from the chromosphere to out far beyond the planets.

1.2.1 Solar Activity

Differential rotation and plasma convection produce intense electric and magnetic fields in the Sun, created through a dynamo action (*Tobias* (2002)). There is a distinct variability in the magnetic fields of the Sun. This pattern follows a 22 year cycle, which coincides with a reversal of the polarity of the Sun's magnetic poles (*Schunk and Nagy* (2000)). One of the main manifestations of the solar activity is sunspots. They appear on the photosphere as black spots due to lower temperatures compared to the surrounding photosphere. They can be both unipolar and bipolar regions and are due to the emergence of magnetic flux from the solar interior and are areas of very strong magnetic fields (up to 3×10^3G). These active bipolar regions are generally oriented in an East-West direction, tilted in latitude

and only appear in low-middle latitudes, below 45° (*Solanki et al.* (2006)). Unipolar regions however are found around the poles and are mainly due to the break up and spread of bipolar regions. Sunspots can last between several days to a few months. The existence of sunspots has been known for an extremely long time, with records of their occurrences from the 17th century. Figure 1.2 shows average sunspot number from 1750-2008, with the solar cycle clearly visible.

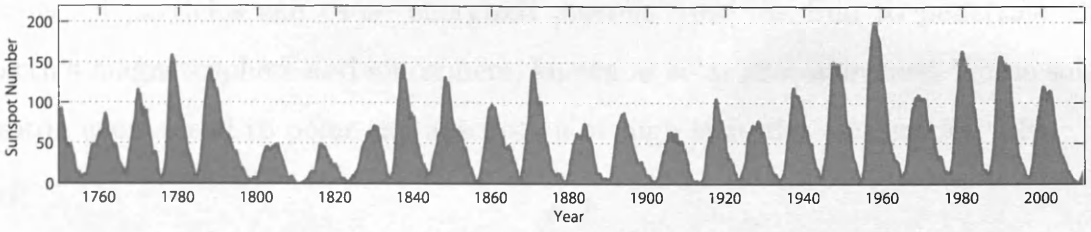

Figure 1.2: Average sunspot numbers from 1750 to 2008. (Data from Solar Influences Data Analysis Center)

1.2.2 Solar Flares

Solar flares are a sudden brightening that occurs on the photosphere and can last between a few minutes to several hours (*Hudson* (2010)). A solar flare is a source of particle and electromagnetic emission that can affect the Earth's upper atmosphere. A solar flare will typically contain three phases: the preflare phase, the rise phase and the main phase. During the preflare phase there occurs a slow rising prominence due to some weak eruptive instability or non equilibrium. This phase will usually last for half an hour and is accompanied with soft X-ray brightening. At the rise phase the stretched field lines start to break and reconnect, this causes the prominence to erupt more quickly with a steep rise in Hα and soft X-ray emissions. The main phase lasts for many hours, with a decline in intensity, the reconnection point rises, hot x-ray loops and Hα ribbons at the footprints are created. Figure 1.3 shows a schematic of the flare loop and ribbons caused by reconnection.

A flare will typically release around 10^{25}J or electromagnetic energy and another 3×10^{25}J as particles. This energy is stored in the coronal structure before the flare is triggered. This triggering method of a solar flare is still currently unknown and an area of current research (eg. *Kusano et al.* (2004)). Effects on the Earth from solar flares can be very serious, hard X-rays emitted from the flare increase the ionization of the upper atmosphere and can damage satellites. The release of particles can cause energized protons from the Sun to penetrate the Earth's magnetosphere and ionosphere, known as solar proton events. These solar proton events lead to polar cap absorption at high latitudes (see section 1.8).

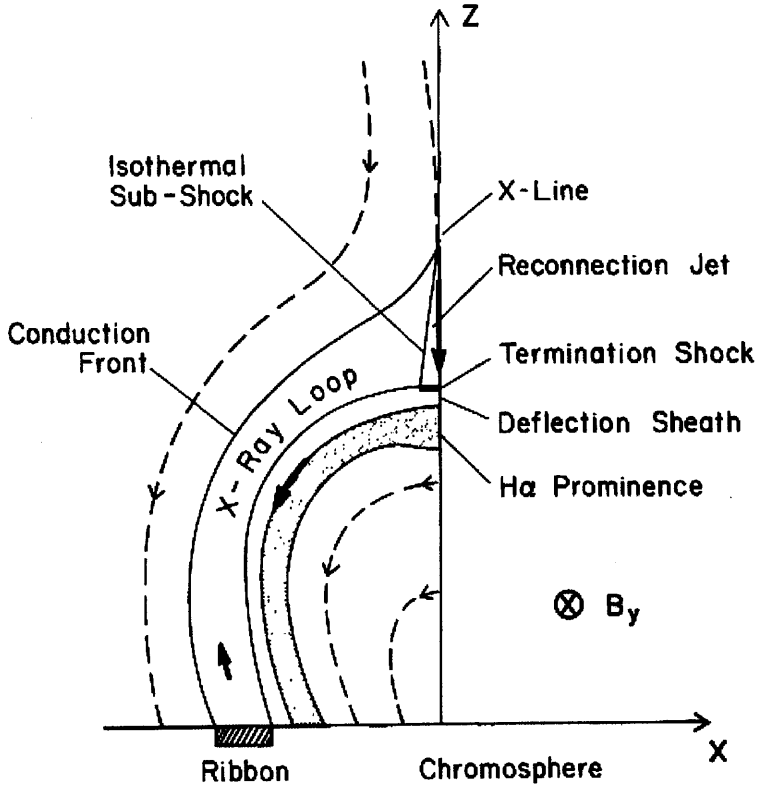

Figure 1.3: Solar flare loops and ribbons caused by reconnection. As field lines reconnect, the loops grow in size, propagating outwards (*Forbes et al.* (1988))

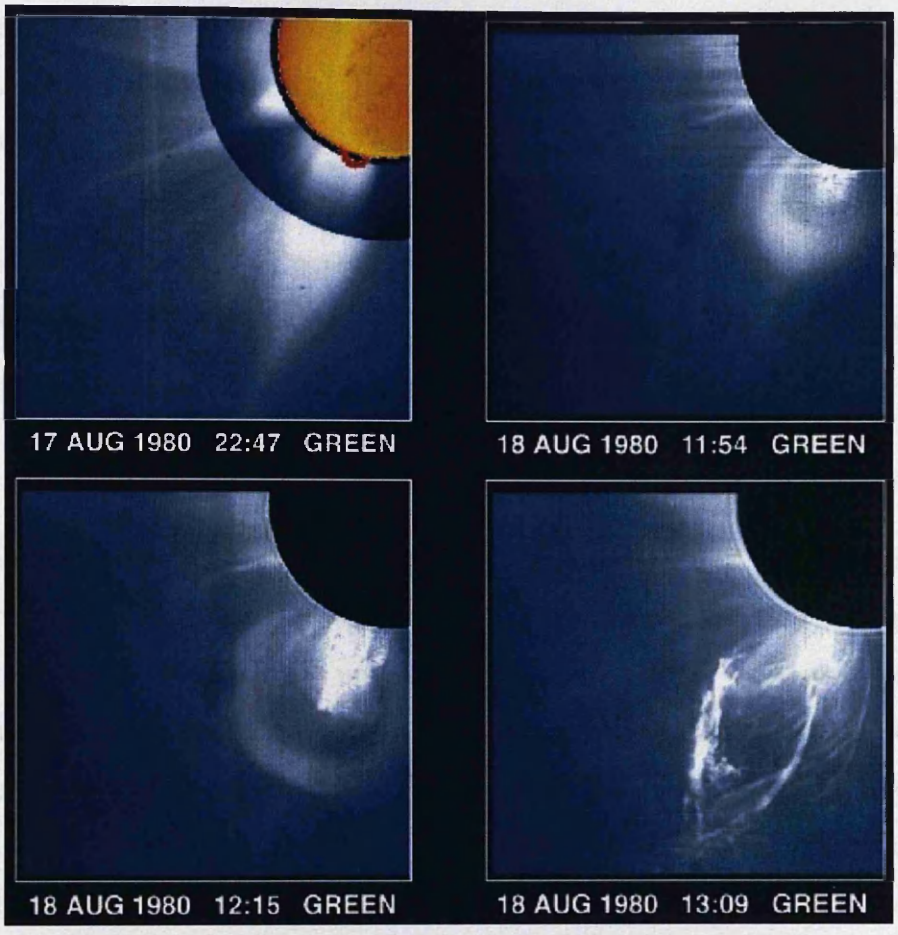

Figure 1.4: Coronal Mass Ejection, August 18, 1980. Aug 17 22.47: The panel shows a streamer that has been swelling outwards. Aug 18 11.54: The panel shows the the bright frontal loop. 12.15: The panel shows the bright frontal loop that has propagated outwards, a dark cavity and a bright core which is associated with the prominence that has also erupted. 13.09: The Panel shows the eruption of the CME. (After *Zhang and Low* (2005))

1.2.3 Coronal Mass Ejection

Coronal mass ejections (CMEs) constitute a major part of solar activity. They are expulsions of large amount of plasma and magnetic flux from the corona into the solar wind. (*Yohsuke and Abraham* (2007)). Figure 1.4 shows an example of a CME through coronagraph images. The speed of CMEs is wide ranging from $1\times10^4 \mathrm{ms}^{-1}$ up to $2\times10^6 \mathrm{ms}^{-1}$ with a median speed of $4.5\times10^5 \mathrm{ms}^{-1}$ (*Zhang and Low* (2005)). The occurrence of CMEs is dependent on the solar cycle. During a solar

minimum there are on average 0.2 CMEs a day, whereas at solar maximum there are on average 2-5 CMEs a day. During the solar minimum CMEs will normally originate from the solar equator, while during the solar maximum they can occur from a wide range of latitudes. CME masses unlike their velocities are relatively constant across events, with masses occupying a narrow range around 3×10^{12} kg. Coronal holes are closely related with solar flares and erupting prominences.

1.2.4 Coronal Hole

Coronal holes are areas of the Sun that emit less radiation at all wavelengths then surrounding regions, first discovered with X-ray telescopes showing dark patches on the Sun's surface. They are unipolar areas, that is areas with open magnetic field lines that go far out into interplanetary space and do not reconnect with the Sun, but with other magnetic phenomena, such as the earth's magnetosphere and heliopause. The field lines are either all inwards or all outwards. At solar minimum coronal holes are confined to the magnetic poles but can occur anywhere at other times. Coronal holes co-rotate with the Sun and can last for several rotations. Coronal holes are the origins of fast solar wind (see section 1.3).

1.3 Solar Wind

The solar wind, discovered in the 1960s is an ever present flow of ionized plasma from the Sun. Resulting from the large pressure difference between the solar corona and interstellar space, the plasma is forced outwards. The solar wind primarily consists of ionized hydrogen with a small percentage (>5%) of ionized helium, and even smaller percentage of heavier atoms. The solar wind is highly variable, with the velocity steadily increasing as the plasma moves away from the Sun. At 1AU the solar wind velocity can vary between $2\times10^{5}\text{ms}^{-1}$ and $1\times10^{6}\text{ms}^{-1}$, with an average velocity of $4.5\times10^{5}\text{ms}^{-1}$.

Table 1.1: Solar wind Parameters (*Schunk and Nagy* (2000))

Parameter	Average	Low-speed	High-speed
$n(\mathrm{cm}^{-3})$	8.7	11.9	3.9
$u(\mathrm{km\ s}^{-3})$	468	327	702
$nu(\mathrm{cm}^{-2}\mathrm{s}^{-1}$	3.8×10^{8}	3.9×10^{8}	2.7×10^{8}
$T_\mathrm{p}(\mathrm{K})$	1.2×10^{5}	0.34×10^{5}	2.3×10^{5}
$T_\mathrm{e}(\mathrm{K})$	1.4×10^{5}	1.3×10^{5}	1.0×10^{5}

Table 1.3 shows some of the solar wind parameters near the Earth for low-speed, high speed and average conditions. Shown are the plasma densities ($n = n_\mathrm{e} = n_\mathrm{p}$), drift velocity ($u = u_\mathrm{e} = u_\mathrm{p}$), number flux ($nu$) and proton and electron temperatures (T_p(K),T_e(K)) (*Schunk and Nagy* (2000)).

1.3.1 Interplanetary Magnetic Field

The solar magnetic field, which close to the Sun resembles a dipole, is carried outwards along with the solar wind. This is known as the interplanetary magnetic field. This weak magnetic field is deemed to be 'frozen in', that is the magnetic flux through a moving patch of plasma is constant. The idea of the frozen in flux was first described by Alfven in 1942, with the discovery of the interplanetary magnetic field being made in 1963 by the Interplanetary Monitoring Platform (*Hargreaves* (1992)).

The slow rotation of the Sun ($2.7\ \times10^{-6}\mathrm{rad\ s}^{-1}$) causes the plasma to spiral outwards, bending the magnetic field as it progresses. *Parker* (1958) theorized this phenomena of which an idealized diagram is shown in figure 1.5; this is known as the Parker spiral. At the Earth's orbit the spiral angle is approximately at a 43° angle with respect to the Sun and Earth. In three dimensions the spirals can be described by the ballerina model, as shown in figure 1.6. This model represents the heliospheric current sheet. The current sheet is the point at which the polarity of the magnetic field reverses. As the different drapes of the 'skirt' interact with

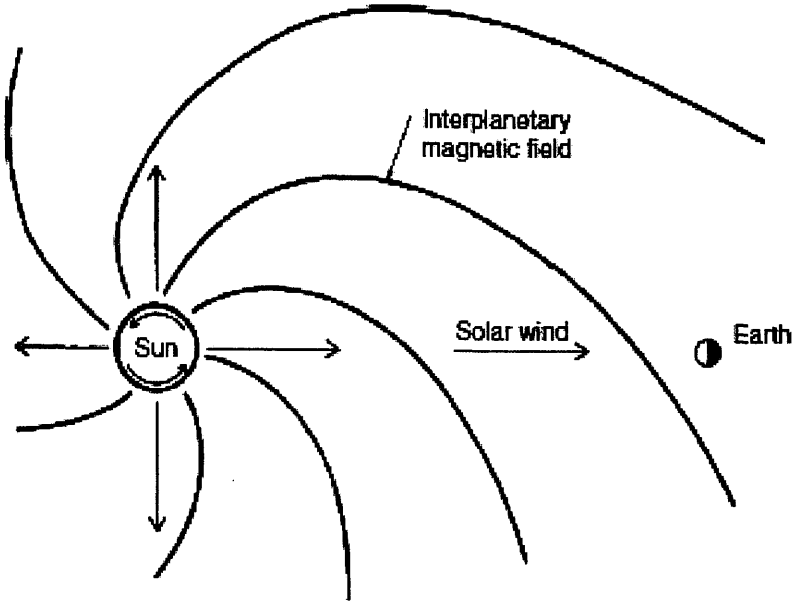

Figure 1.5: Solar wind and interplanetary magnetic field in the Sun's ecliptic plane (After *Schunk and Nagy* (2000)).

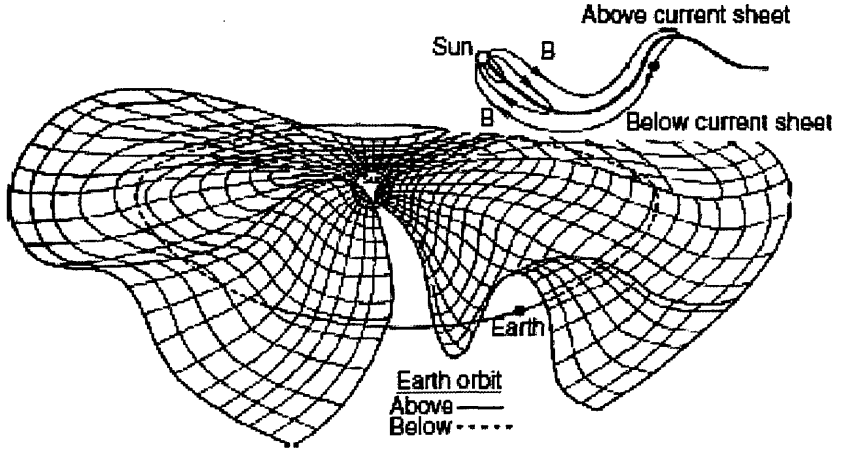

Figure 1.6: Ballerina model of the current sheet in the solar wind. The inset at the top of the figure shows the opposite polarities of the magnetic fields on the two sides of the current sheet. (After *Schunk and Nagy* (2000))

solar bodies, the bodies are exposed to different polarity configurations of the interplanetary magnetic field. This is an important factor when the IMF interacts with the Earth's geomagnetic field (Section 1.4.1).

1.3.2 Solar Wind Shocks

Formation of shocks in the solar wind can effect the ionosphere due to the strong impulsive forces associated with them. Shocks are formed from the interaction between fast solar wind streams and the slow solar wind. Figure 1.7 shows the interaction of the fast and slow solar wind. As the fast solar wind overtakes the slow ambient solar wind it creates a density compression in front of the fast stream and a rarefaction in its wake. If the velocity of the fast solar wind is great enough it can form a forward and rear shock. The source of the fast solar wind is from coronal holes and typically has speeds of around $7.5\times10^5 ms^{-1}$. The interaction region and the following high speed solar wind is referred to as a co-rotating interaction region (CIR) and can cause particle precipitation into the Earth's ionosphere (eg *Longden et al.* (2008)).

Shocks can also be formed by CMEs. Some CMEs can become isolated magnetically from the Sun, becoming plasmoids. If the plasmoid is moving fast enough shocks form in front in the ambient plasma. The ambient plasma is forced around the plasmoid, dragging the IMF around with it creating closed magnetic loops and forming an isolated magnetic cloud.

1.4 Magnetosphere

The Earth's magnetic field can be to a first approximation described by a magnetic dipole. The poles of the magnetic dipole can be found at and around 79° N, 70° W, and 79° S and 70° E. The Earth's magnetic field is thought to be generated

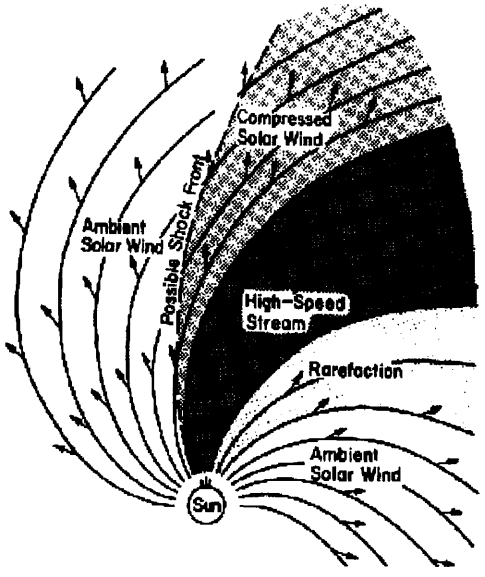

Figure 1.7: Interaction of fast and slow solar wind. The fast solar wind compresses the solar wind in front of the high speed stream and rarefaction in its wake. The interaction of the fast and slow solar wind are bounded by a forward shock. (After *Holzer* (1979, p103))

by a dynamo action from the motion of a fluid core. (*Gubbins* (1974)). The magnetosphere is determined by interaction of the Earth's magnetic field, the solar wind and the IMF. Figure 1.8 shows a cross section of the magnetosphere, with the main constituent parts labeled.

The **magnetopause** is the boundary between the solar wind and the Earth's geomagnetic field. To a first approximation it is the point where the magnetic pressure of the Earth's magnetic field ($B^2/2\mu_0$) is balanced by the dynamic pressure of the solar wind. Along the Sun-Earth line the boundary for the magnetopause is around $10R_e$. The Earth's geomagnetic field is severely distorted by this process, there is compression of field lines on the day side, with elongation of the night side. Field lines in the polar regions on the day side can be swept backwards 'down tail', and finally there is a point in both hemispheres that meet the magnetopause that has zero flux density known as the **neutral points**.

Outside of the magnetopause is the **magnetosheath**. This region extends

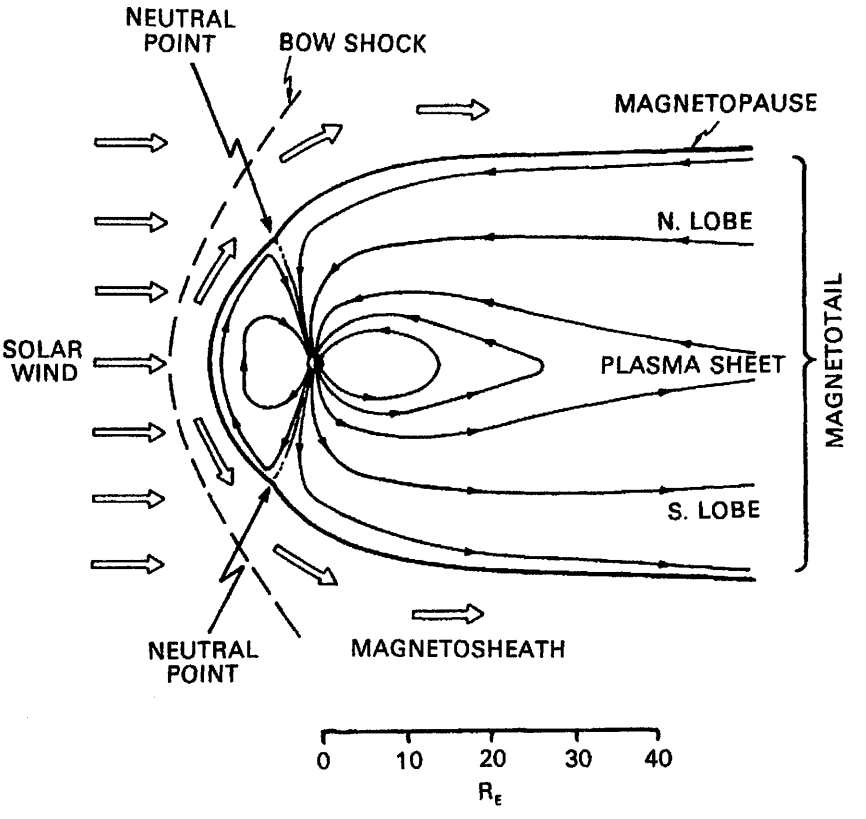

Figure 1.8: Cross section of the magnetosphere and external plasma flow. Figure shows the prominent features of the magnetosphere. (After *Vasyliunas* (1983))

from the magnetopause towards the Sun for about 2-3R_e and is fronted by the **bow shock**. The magnetosheath is a region of turbulent plasma, with a density that is greater than is found in the preceding solar wind. The plasma velocity within the magnetosheath is greater than any wave velocities that can propagate through it. The bow shock is a discontity between the solar wind and the magnetosheath. As the solar wind passes through the bow shock the solar wind plasma is slowed down to around $2.5\times10^5 ms^{-1}$, transferring the lost kinetic energy into heat.

The two neutral points as described earlier are points where the magnetosphere and magnetopause meet with zero flux. These are regions of great interest as they are the only points that connect the Earth's surface with the magnetopause. The field lines of the magnetopause all converge on these two points. They are points

where particles from the solar wind can directly enter the magnetosphere. Observations of such particles have been made for example by *Heikkila and Winningham* (1971). The location of the cusp can change in latitude between 70° to 86° , with particles being observed around 5° around the neutral points. These are extended regions and not just points and are known as the **polar cusps**. The size of the polar cusps vary due to solar wind parameters, such as solar wind density (*Zhou et al.* (2000)).

Due to the effect of the solar wind the Earth's geomagnetic field is dragged out antisunwards creating the **magnetotail**. In the northern hemisphere of the magnetotail, the magnetic field points towards the Earth while in the southern hemisphere the magnetic field is pointed away from the Earth. These two sections of the magnetotail are known as the **magnetospheric lobes**. There is a central plane where the field reverses direction, known as the **neutral sheet**. The magnetotail flux is around 20nT but is much weaker at the reversal boundary (*Hargreaves* (1992)).

1.4.1 Magnetosphere - IMF Coupling

Connections between the magnetosphere and the IMF were first proposed by *Dungey* (1961, 1963), creating two models both including the polar cusps but also being able to drive circulation in the magnetosphere. Figure 1.9 shows the Dungey models for reconnection. The first model is with the IMF having a northward magnetic field, reconnection occurs tailward of the polar cusps and closed flux tubes are added to the dayside magnetosphere. The second situation is when there is a southward facing IMF. When this occurs geomagnetic field lines connect with IMF field lines, transferring plasma over the poles into the tail. On the nightside of the Earth the field lines reconnect and return to the dayside. The southward IMF allows transfer of mass, momentum and energy into the magne-

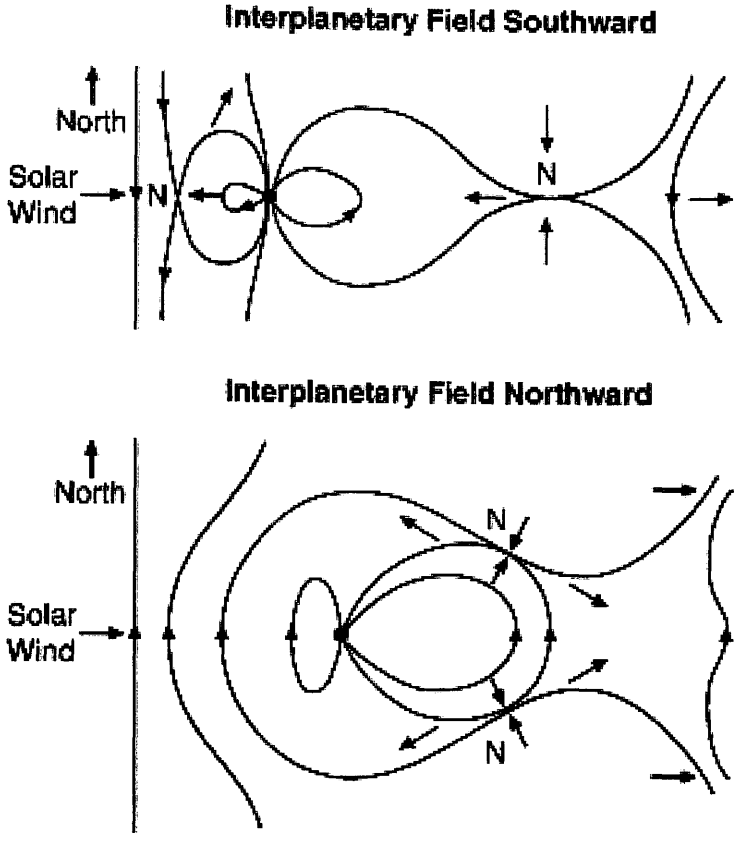

Figure 1.9: Dungey model of reconnection for northward (bottom) and southward IMF (top) (after *Dungey* (1963))

tosphere (*Russell* (1999)). This process can explain storms and substorms. (see sections 1.6 and 1.7).

The momentum transfer between the IMF and magnetosphere is dominated by the effects of the southward IMF, during northward IMF the process of viscous interaction, (*Axford and Hines* (1961)) has a role to play. In this process the momentum of the magnetosheath is transferred between and across the magnetopause by waves and diffusion, creating a viscosity. One such viscous interaction that is an efficient method of momentum transfer into the magnetosphere is the Kelvin-Helmholtz instability, caused by the shear velocity imposed form the solar wind flowing around the magnetosphere, (*Smets et al.* (2002)).

1.4.2 Particles in the Magnetosphere

The magnetosphere contains within it several distinct distributions of populations of charged particles. These are the **plasmasphere, plasma sheet** and **Van Allen belts**. Figure 1.10 shows the plasma populations in the magnetosphere as well as the current systems (section 1.4.9). The source of particles for the magnetosphere are the Solar wind and the ionosphere.

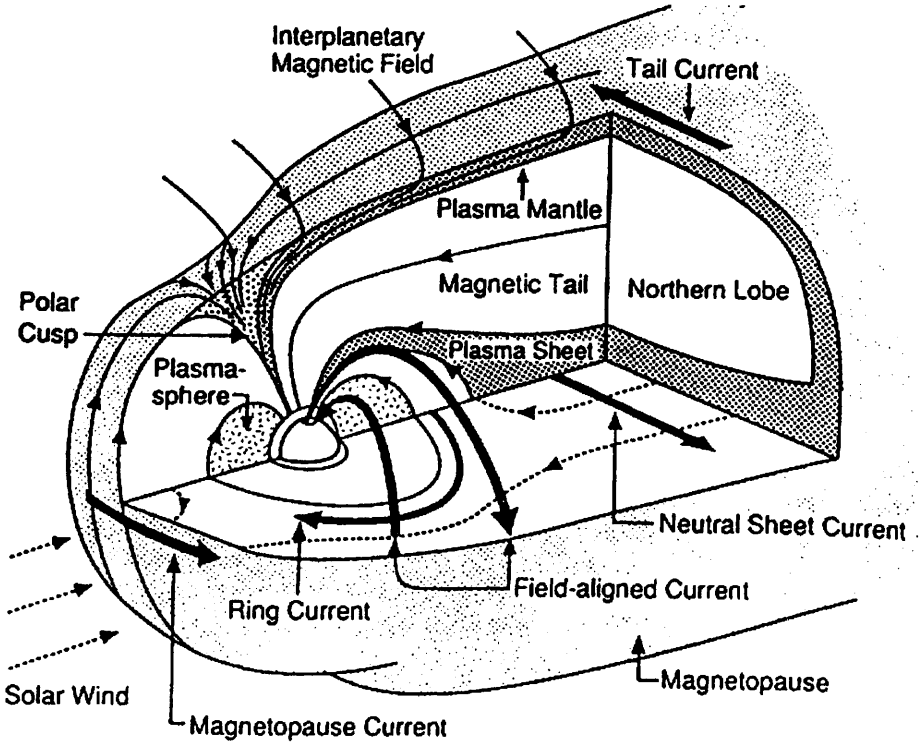

Figure 1.10: Plasma populations and current systems in the magnetosphere (*Shirley and Fainbridge* (1997))

Plasmasphere

The plasmasphere was discovered by *Carpenter* (1963), through the analysis of 'whistler' waves observed on the Earth. It is a region of high density, ($\sim 10^3 \mathrm{cm}^{-3}$) cold plasma (energy $\sim$1eV). The whistlers showed a sharp boundary at 3-5R_e.

This boundary, known as the **plasmapause** is where the cold dense plasma suddenly terminates. The population of the plasmasphere is from the 'polar wind', a steady flow of plasma upwards from the planet emanating from the high latitude ionosphere. The plasmasphere is a magnetically aligned structure, which has an asymmetrical shape, having a dusk side bulge (*Carpenter* (1970)).

Plasma sheet

The plasma sheet is located along closed field lines in the equatorial magnetotail, at the reversal boundary. The average density of the plasma sheet is 0.3-0.4 cm^{-3}, with temperatures of 5×10^7K close to the neutral sheet (*Baumjohann et al.* (1989)). The plasma sheet is separated from the tail lobes by the plasma sheet boundary layer. The plasma sheet is an important region as it maps down to the auroral oval.

Van Allen Belts

Discovered in 1958 the radiation belts or Van Allen belts, are regions of trapped high intensity charged particles (*Van Allen* (1959)). The Van Allen belts consist of two distinct regions of particles, the inner and outer zone. The inner belt is located between 1.1-3.3R_e in the equatorial plane. The inner zone consists mainly of protons, with energies exceeding 10MeV. The particles are created by the decay of neutrons, which themselves come from primary cosmic ray protons (*Hargreaves* (1992)). The inner zone is a fairly stable population with variations due to the 11 year solar cycle and large geomagnetic storms.

The outer zone is located between 3-9 R_e in the equatorial plane and is more dynamic than the inner zone. The outer zone contains mainly electrons with energies up to 1MeV. The generation of the outer belts is from injection and acceleration of particles from geomagnetic storms. Figure 1.11 shows the distributions of trapped

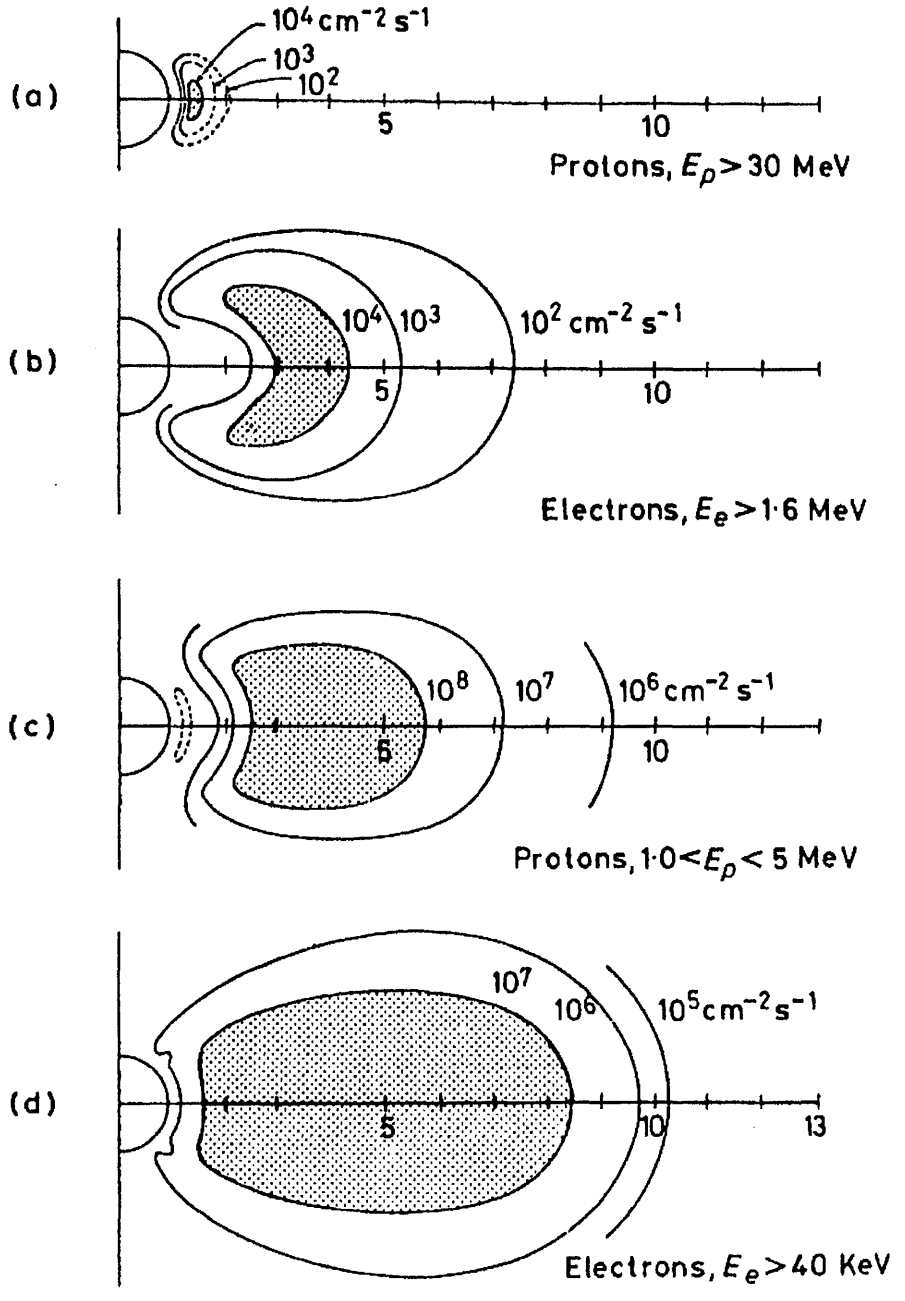

Figure 1.11: Distribution of trapped protons and electrons for a range of energies. (After *Hess* (1968))

protons and electrons in the magnetosphere for various energy ranges. Figure 1.11 a. shows the inner zone distribution of protons Figure 1.11 b. c. and d. show the distributions for electrons and protons in the outer zone. The maximum flux for

the inner zone is around $2R_e$ and $4R_e$ for the outer zone. Between 3-4 R_e there is a flux minimum, of a factor of 10-10^4 depending on energy. This is known as the **slot region**. The slot region can fill up in periods of enhanced geomagnetic activity, with a gradual return to normal levels in the following days.

1.4.3 Particle Motion

This section describes the motion of particles in the magnetosphere. The motion of a charged particles is governed by three parameters: the magnetic field **B**, electric field **E** and a non-electromagnetic force **F**, and is given by:

$$\frac{d\mathbf{p}}{dt} = q\left(\mathbf{v} \times \mathbf{B} + \mathbf{E}\right) + \mathbf{F} \tag{1.1}$$

Where **p**, **v** and q are the particle's momentum, velocity and charge respectively. Equation 1.1 can be simplified under certain conditions. There can be up to three distinct periodicities (i) cyclotron motion, (ii) bounce motion and (iii) drift motion. While (i) can readily occur without the presence of either (ii) or (iii), (ii) and (iii) require specific conditions to occur. A particle in a magnetic field that has the capability of bounce motion (i) is said to be in a trapping field. If as well the particle is capable of drift motion then it is said to be stably trapped (*Roederer* (1970)). The mechanisms that allow the trapping of particles are best expressed in terms of adiabatic invariants, these are a series of terms that do not change providing some other quantity does not change or changes at a sufficiently slow rate.

1.4.4 Cyclotron Motion

A charged particle in a uniform magnetic field without any other external forces will undergo cyclotron motion. Thus equation 1.1 can be rewritten as:

$$\frac{d\mathbf{p}}{dt} = q\mathbf{v} \times \mathbf{B} \tag{1.2}$$

This equation is known as the Lorentz equation of magnetic force. In the absence of non magnetic forces the particles velocity $\mathbf{v}$ and mass m will remain constant. If there is no parallel component of velocity with respect to the magnetic field the particle will just circle the magnetic field line. If there is a parallel velocity component the particle will precess along the magnetic field line in a helical motion. Figure 1.12 shows the helical motion of a positive particle along a magnetic field line. Also shown in figure 1.12 is the particles pitch angle α, this is the angle

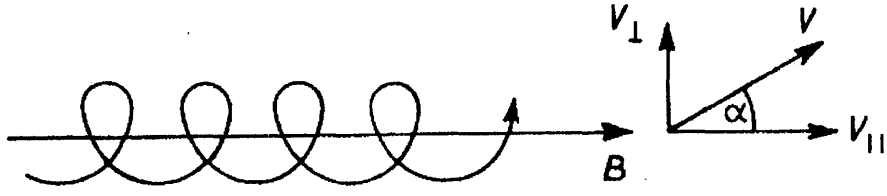

Figure 1.12: Motion of a Positive particle along a magnetic field line. (After *Hargreaves* (1992))

between $\mathbf{v}$ and $\mathbf{B}$. The pitch angle is defined as:

$$\sin(\alpha) = \frac{v_\perp}{v} \text{ or } \cos(\alpha) = \frac{v_\parallel}{v} \tag{1.3}$$

Where $v_\perp$ and $v_\parallel$ are the perpendicular and parallel velocity components to the magnetic field respectively. The circular motion caused by the Lorentz force can be equated to the centripetal force $\mathbf{F} = mv_\perp^2/r_B$ allowing us to define the gyroradius,

r_B:

$$r_B = \frac{mv_\perp}{q\mathbf{B}} \tag{1.4}$$

r_B is valid relativistically, as long as the mass of the particle is the relativistic mass, $m = m_0\gamma$.

As long as no work is done on or by the particle the magnetic flux through the particles orbit (Φ_m) is constant, therefore:

$$\Phi_m = \mathbf{B}\pi r_B^2 = \frac{2\pi m \mathrm{E}_\perp}{q^2\mathbf{B}} = const. \tag{1.5}$$

where $\mathrm{E}_\perp$ is the kinetic energy associated with $v_\perp$:

$$\mathrm{E}_\perp = \frac{mv^2}{2} \tag{1.6}$$

If you consider the magnetic moment of the current loop represented by the particle and substituting in equation 1.4 and equation 1.6 where appropriate: (eg. *Hargreaves* (1992) eq. 5.28)

$$\mu = \text{current} \times \text{area of the loop} = \frac{qv_\perp}{2\pi r_B}\pi r_B^2 = \frac{mv_\perp^2}{2\mathbf{B}} = \frac{E_\perp}{\mathbf{B}} \tag{1.7}$$

Equation 1.5 showed that $\mathrm{E}_\perp/\mathbf{B}$ is constant, thus it follows that the magnetic moment is constant, this is the first adiabatic invariant (*the magnetic moment is constant*). This is true as long as the magnetic field does not change significantly during one period of rotation. The kinetic energy in the perpendicular direction can be written in terms of the pitch angle α and overall velocity v using equation 1.3, therefore:

$$\frac{\mathrm{E}_\perp}{\mathbf{B}} = \frac{mv_\perp^2}{2\mathbf{B}} = \frac{m}{2}\frac{v^2\sin^2\alpha}{\mathbf{B}} = const. \tag{1.8}$$

It follows then that:

$$\sin^2\alpha \propto \mathbf{B} \tag{1.9}$$

1.4.5 Bounce Motion

As the particles move away from the equator and approach higher latitudes of the Earth's dipole field the magnetic flux density **B** increases, thus the pitch angle also increases (equation 1.9). When the pitch angle reaches 90° the forward motion of the particle will stop and the particle will reverse direction. This point of reversal is called the mirror point. The total energy of the particle does not change during this process, as no acceleration processes are at work on the particle. As the particle approaches the mirror point the parallel energy decreases, with a transfer of energy into the perpendicular component. It is the conservation of the first adiabatic invariant that allows the trapping of the particles in this non-uniform magnetic field. The mirror point of a particle can be described by the pitch angle of the particle at the equator (α_0), as:

$$\frac{\mathbf{B}_0}{\mathbf{B}_m} = \sin^2 \alpha_0 \tag{1.10}$$

where $\mathbf{B}_0$ and $\mathbf{B}_m$ are the magnetic flux densities at the equator and mirror point respectively. The trapping of particles due to bounce motion is shown in figure 1.13.

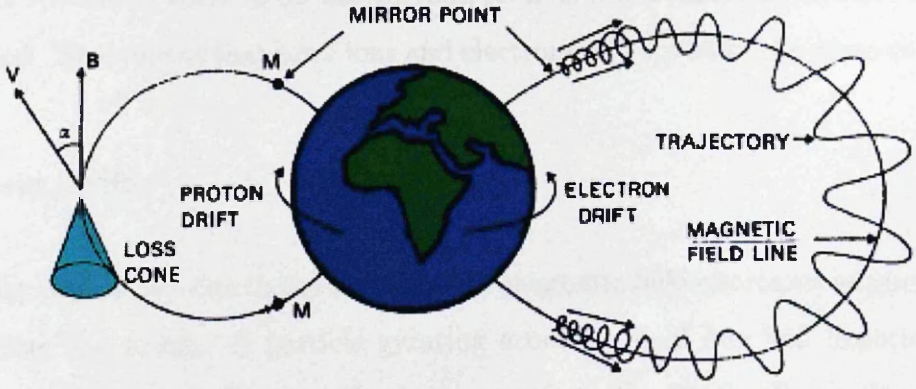

Figure 1.13: Trajectories of particles on trapped field lines. (After *Lemaire* (1982))

If the particle does not reach it's mirror point before it enters the Earth's atmosphere then it will be lost to the atmosphere. The equatorial pitch angles of particles that will be lost to the atmosphere define the loss cone.

1.4.6 Drift Motion

In addition to the gyration of charged particles around field-lines and bounce motion, charged particles in the magnetosphere are subject to three primary drift motions, (i) $\mathbf{E}\times\mathbf{B}$ drift, (ii) gradient drift and (iii) curvature drift. These three drift motions cause the particles to drift around the Earth.

$\mathbf{E}\times\mathbf{B}$ drift

If a charged particle is in a magnetic field ($\mathbf{B}$) with an Electric Field ($\mathbf{E}$) that has a perpendicular component with respect to $\mathbf{B}$, then the particles will drift with a velocity, ($\mathbf{v}$) given by:

$$\mathbf{v} = \frac{\mathbf{E}\times\mathbf{B}}{|\mathbf{B}|^2} \tag{1.11}$$

The vector $\mathbf{v}$ will act normal to $\mathbf{E}$ and $\mathbf{B}$, and will have a magnitude of $\mathbf{E}/\mathbf{B}$. $\mathbf{E}\times\mathbf{B}$ is special as there is no net current, as it is independent of electric charge and mass. This means that both ions and electrons will travel at the same velocity.

Gradient Drift

Gradient drift arises due to the fact that the magnetic field decreases as you move away from the Earth. A particle gyrating around a field line will experience a weaker magnetic field when it is furthest away from the Earth. This will cause a shift in the orbit of the gyrating particle, causing it to move laterally around the Earth. Figure 1.14 shows the drift due to a magnetic field gradient. The speed at

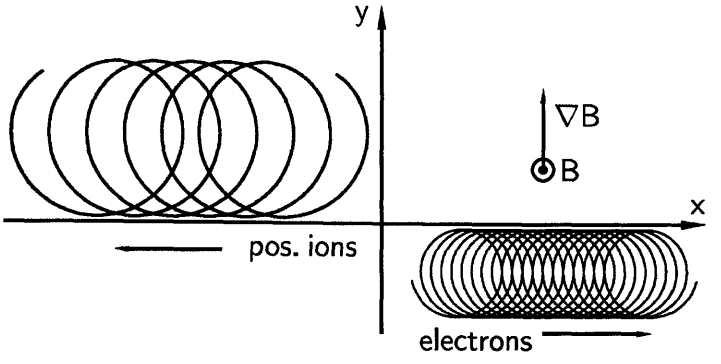

Figure 1.14: Longitude drift caused by a gradient in geomagnetic field intensity (After *Piel* (2010))

which the particles will drift is given by:

$$\mathbf{V}_G = \frac{mv_\perp^2}{2q\mathbf{B}^2}\mathbf{e} \times \nabla_\perp \mathbf{B} \tag{1.12}$$

where $\mathbf{e}$ is a unit vector in the direction of $\mathbf{B}$. The charge dependence of equation 1.12 leads to charge separation and the formation of a current across the magnetic field. see *Roederer* (1970) or *Piel* (2010) for a derivation of equation 1.12.

Curvature drift

Curvature drift is caused by the curvature of the field lines. Particles experience a centrifugal force of:

$$\mathbf{F}_c = \frac{mv_\parallel}{r_B}\mathbf{n} \tag{1.13}$$

where $\mathbf{n}$ is the unit normal vector directed along field line's radius of curvature. This force causes a drift velocity at right angle to itself and has a velocity of:

$$\mathbf{V}_c = \frac{mv_\parallel^2}{qr_B B}\mathbf{n} \times \mathbf{e} \tag{1.14}$$

For curl-free fields: (*Roederer* (1970))

$$\nabla_{\perp} B = -\frac{B}{r_B}\mathbf{n} \tag{1.15}$$

Therefore equation 1.14 can be written as:

$$\mathbf{V}_c = \frac{mv_{\parallel}^2}{qB^2}\mathbf{e} \times \nabla_{\perp} B \tag{1.16}$$

The combination of gradient drift and curvature drift is commonly known as gradient-curvature drift. As equation 1.12 and 1.16 act in the same direction they can be combined to form an equation for velocity caused by both effects:

$$\mathbf{V}_{gc} = \frac{1}{2}\frac{mv^2}{qB^2}\left(1 + \cos^2\alpha\right)\mathbf{e} \times \nabla_{\perp}\mathbf{B}. \tag{1.17}$$

If the Earth was a true dipole gradient-curvature drift would only serve to distribute the particles to all longitudes. However the Earth is not a true dipole and the drift paths are more complicated. The path can be calculated using the second adiabatic invariant. The second adiabatic invariant states that: *the integral of the parallel momentum over one bounce between mirror points is constant* (*Hargreaves* (1992)), or:

$$\mathbf{J} = 2\int_{l_1}^{l_2} mv_{\parallel}\mathrm{dl} = const. \tag{1.18}$$

This is true only if the magnetic field does not change significantly during one bounce period. The final adiabatic invariant states: *the total geomagnetic flux enclosed by the drift orbit is constant* (*Hargreaves* (1992)). This invariant is a lot less robust than the first two as it depends on there not being any significant changes over the drift period.

The particle motions allow for stably-trapped regions of particles in the magnetosphere, which make up the Van Allen belts. However there are regions where particles will not complete their drift around the Earth. These particles are said to be in quasi-trapping regions. The quasi-trapping regions arise from the varia-

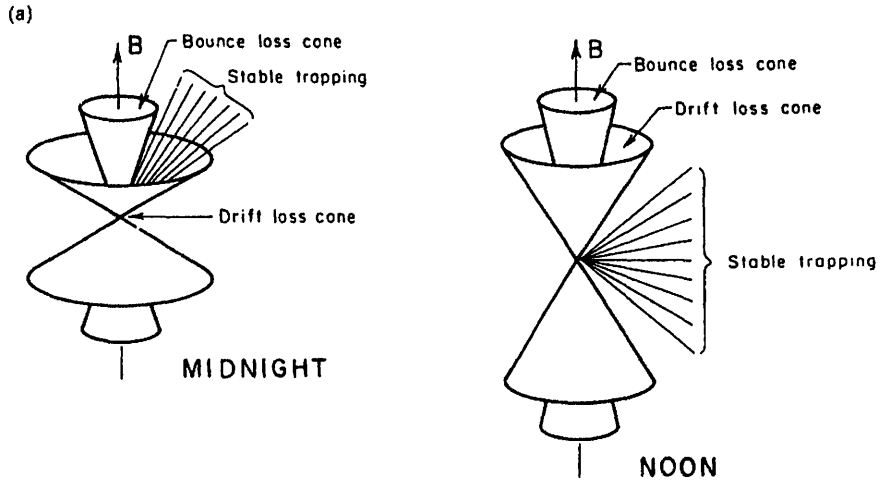

Figure 1.15: Drift and bounce loss cones for the midnight and noon meridians. (After *Roederer* (1970))

tions in the magnetic field. Particles that are injected at the midnight meridian and are mirroring around $\alpha = 90°$, will move out when entering the day side magnetosphere to remain at a constant field intensity. This is due to the increase of magnetic field strength from the compression of the magnetosphere by the solar wind. Therefore some of these particles will leave the magnetosphere before reaching the noon meridian. The second region of quasi-trapping arises from particles will small pitch angles, mirroring at high latitudes. These particles entering at the noon meridian run into the tail before completing one full drift. Figure 1.15 shows these drift loss cones as well as the previously discussed bounce loss cones for the noon and midnight meridians.

1.4.7 Particle Diffusion

The radiation belts are subject to two main diffusion processes, radial diffusion and pitch angle diffusion. Radial diffusion displaces particles across field lines and pitch angle diffusion moves a particles pitch angle along the field line. Radial

diffusion occurs when the third adiabatic invariant is broken, that is the magnetosphere changes in times smaller than the drift period. This is accompanied with acceleration if the first two adiabatic invariants are preserved. As particles mirror at higher B-values in the inward radial displacement, their kinetic energies increase accordingly. (*Roederer* (1970)).

Pitch angle diffusion is a major cause of particle loss from the outer zone. The particles mirror points are spread along field and can drive trapped particles into the loss regions of the atmosphere. This occurs when the second adiabatic invariant is violated due to interaction with electrostatic and electromagnetic waves that act over time periods shorter than the bounce period.

1.4.8 L-Parameter

The L-parameter is a parameter that describes a set of planetary magnetic field lines. It is a development of the second adiabatic invariant and was introduced by *Mcllwain* (1961). The L-parameter describes magnetic field lines that cross the Earth's magnetic equator at integer values of R_e. For example L=1 is a magnetic field line that is 1 R_e away at the magnetic equator. This parameter describes magnetic field lines for a dipole field. For closed field lines the L-parameter is constant to around 1% and therefore is usefull for descrbing field lines even though they are not a true dipole. An invariant Latitude may be described in terms of the L-parameter:

$$\Lambda = \cos^{-1}\left(\frac{1}{L}\right)^{\frac{1}{2}} \tag{1.19}$$

where Λ is the invariant latitude, and L is the L-parameter.

1.4.9 Current Systems

There are several current systems that are produced by the plasma and electric fields in the magnetosphere. These are, (i) magnetopause current, (ii) tail current, (iii) ring current and (iv) Birkeland current. Figure 1.16 shows the current systems for (i)-(iii).

Magnetopause current

The magnetopause or (Chapman-Ferraro) current system is located on the edge of the magnetosphere. Seen in figure 1.16.a the current system is such to cancel out the geomagnetic field outside the magnetopause boundary.

Ring Current

The second current system is the ring current, seen in figure 1.16.b. It is produced by the drift of trapped particle, as described in section 1.4.6. The westward drift of protons and eastward drift of electrons produce a clockwise(viewed looking down on the North Pole) current system. The particles responsible are usually low energy (10-100keV) protons, with H^+ being the major ion. The location of the ring current is between 4-6R_e. The ring current flows in a direction so that it's magnetic field opposes the geomagnetic field, depressing it and thus can be monitored by ground based magnetometers.

Tail Current

The third current system is the tail current, this is a current system that crosses the plasma sheet from the dawn to dusk. The current system is shown in figure 1.16. The tail is bounded, and the current has to be a closed circuit so flows in a double solenoid shape.

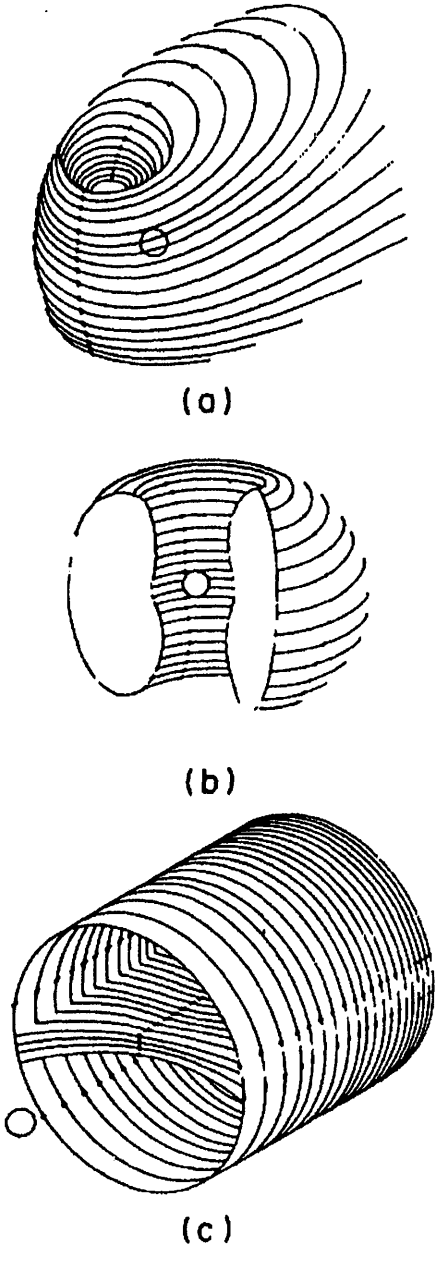

Figure 1.16: Magnetospheric current systems: (a) magnetopause; (b) ring; (c) tail. (After *Olsen* (1982))

Birkeland Currents

The idea of field aligned currents was put forward by *Birkeland* (1908), whom they are named after. They are ionospheric-magnetospheric currents that flow

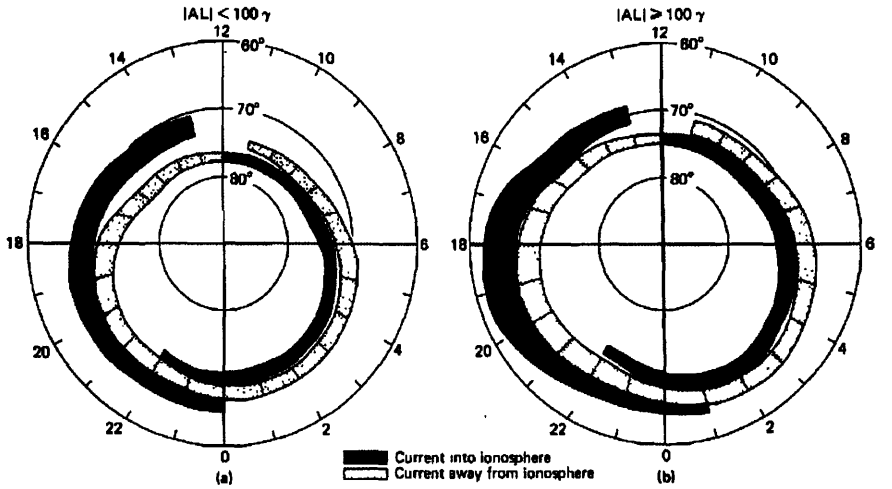

Figure 1.17: Distribution of Birkeland currents during (a) weak and (b) active disturbances. (After *Iijima and Potemra* (1978))

along the geomagnetic field lines. Originally dismissed they were observed in the 1970s by satellite measurements. Passing over the auroral zone the satellites observed a westward magnetic field extending over 2-3° of latitude. To explain this magnetic field the satellites must have passed through two electric sheets, one directed upwards and the other downwards. Figure 1.17 show the distribution of the Birkeland currents in the ionosphere during weak and active disturbances. The effects of Birkeland currents on the ionosphere are described in section 1.5.3.

1.5 Ionosphere

The Earth's atmosphere stretches up from the ground to over 10000km above the Earth's surface, held in place by the Earth's gravity. The neutral atmosphere contains 5 principle layers: troposphere (6-20km), stratosphere (20-50km), mesosphere (50-85km), thermosphere (85-690km) and finally the exosphere (690-10000km). The main neutral constituents of the thermosphere are N_2, O_2 and O. The ionosphere is the ionized part of the atmosphere, reaching from 60-1000km

and contains significant number of free electrons and positive ions. The ionosphere is split up into four main regions, the D, E, F1 and F2 regions. The D region stretches from 60-90km, E region 105-160km, F1 region 160-180km, and F2 region 160km+. Figure 1.18 shows average electron density profiles for the ionosphere for night and day, and solar minimum and maximum. During the night time the D and F1 regions disappear and the E and F region densities are smaller.

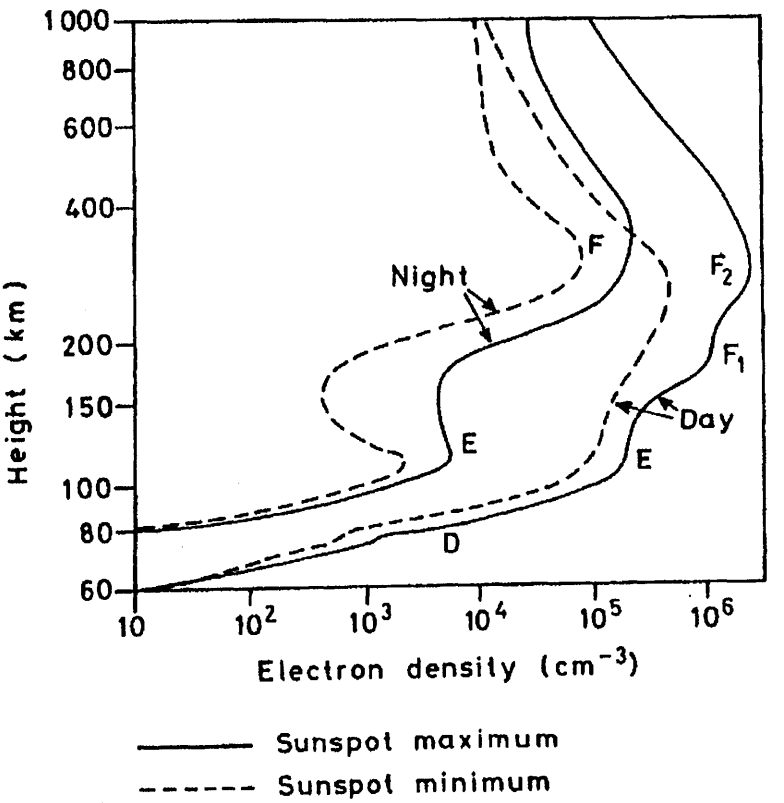

Figure 1.18: Typical electron density profiles in the mid-latitude ionosphere. For night time and day time conditions at solar minimum and solar maximum (After W. Swider, Wallchart Aerospace Environment, US Air Force Geophysics Laboratory)

The formation of the ionosphere is a dynamic equation balancing the production, loss and transport of electrons. The continuity equation for the rate of change

of electron density is given by:

$$\frac{dN}{dt} = q - L - \nabla N\mathbf{v} \tag{1.20}$$

where q is the production rate, L is the loss rate due to recombination and $\nabla N\mathbf{v}$ is the loss of electrons due to transport, where $\mathbf{v}$ is the mean drift velocity of the electrons.

1.5.1 Production Processes

There are two main production processes that contribute to the production of the ionosphere, (i) ionization by solar radiation in the EUV and x-ray spectrum and (ii) ionization by precipitating particles. Photoionization is the dominant process for ionization by radiation and for the three major species:

$$\begin{aligned} N_2 + h\nu(< 796\mathring{A}) &\rightarrow N_2^+ + e \\ O_2 + h\nu(< 1026\mathring{A}) &\rightarrow O_2^+ + e \\ O + h\nu(< 911\mathring{A}) &\rightarrow N_2^+ + e \end{aligned} \tag{1.21}$$

where h is Planck's constant and ν is the frequency of the photon. The stated wavelengths are the ionization thresholds for the production of ions in their ground electronic state. As well as photoionization, dissociative ionization is an additional source of atomic ions and electrons:

$$\begin{aligned} O_2 + h\nu(< 662\mathring{A}) &\rightarrow O^+ + O + e \\ N_2 + h\nu(< 510\mathring{A}) &\rightarrow N^+ + N + e \end{aligned} \tag{1.22}$$

The values for the photon threshold are from *Rees* (1989) and are for electronic ground state, but a a substantial fraction of ions come from electronically excited states so would have different threshold values. The rate of production of ion-

electron pairs can be described by the Chapman production formula

$$q = \eta \alpha n I \tag{1.23}$$

where I is the intensity of the ionizing radiation, n is the number of atoms and molecules available for ionization, α is the absorption cross section and η is the ionization efficiency. The derivation of the Chapman function makes the assumptions: (i) The atmosphere is composed of a single species exponentially distributed, (ii) There is no variations in the horizontal plane, (iii) Solar radiation is absorbed in proportion to the concentration of gas particles and (iv) the absorption coefficient is constant, or there is monochromatic radiation (*Hargreaves* (1992)). These assumptions mean that the Chapman function may not describe a true ionosphere, as they are more complicated than the assumptions state, but is a simple start to ionospheric theory, and interpreting observations.

Production sources for the E and F regions are primarily solar EUV radiation between 200-1027$\mathring{A}$, and soft x-rays between 10-100$\mathring{A}$, ionizing most major and minor species. The D region ionosphere is a lot more complicated, chemically and thus has numerous sources of ionization. The ionization sources, listed from *Hargreaves* (1992) are:

1. Lymann-α line at 1215$\mathring{A}$ ionizes nitric oxide.
2. EUV spectrum between 1027-1118$\mathring{A}$ ionizes an excited oxygen state.
3. EUV ionization of O_2 and N_2
4. Hard x-rays, 2-8$\mathring{A}$ ionizing all constituents
5. Galactic cosmic rays

The contribution of each effect varies on latitude, time and level of solar activity.

At low latitudes the ionosphere production is dominated by radiation processes, with little or no input from particle precipitation. However at higher latitudes in and above the auroral oval, particle precipitation plays a large role in the production of ions in the ionosphere. Section 1.8 discusses the various forms of particle precipitation into the ionosphere.

Electrons entering the atmosphere will ionize neutral particles as they pass through the ionosphere. These electrons are usually auroral electrons. As the electrons progress through the atmosphere they will encounter increasing densities. The total number of ion-electron pairs an electron can create depends on $E/\Delta E$, where E is the initial energy and and ΔE is the energy required for each ionization. Figure 1.19 shows the production rates for a model atmosphere for a range of monoenergetic electrons of various energies. Integrating over energy would give a more realistic production spectrum. Another source of precipitat-

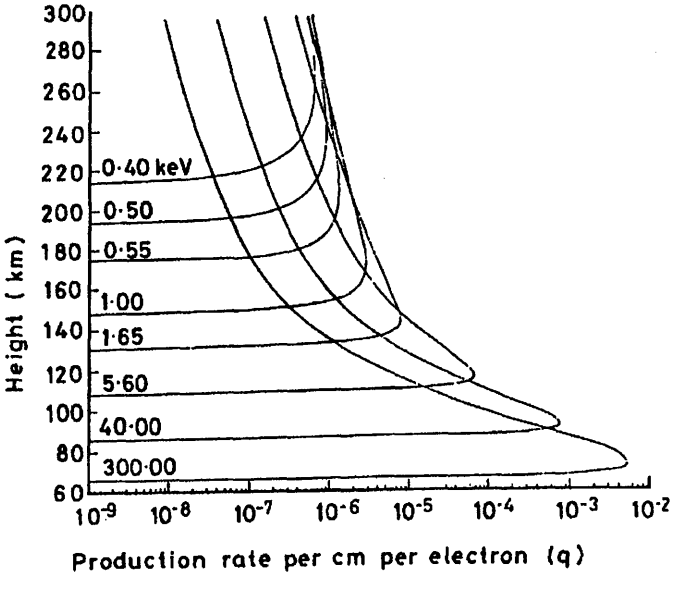

Figure 1.19: Production rates of monoenergetic electrons of various initial energies. Energies given in MeV (After *Rees* (1963)

ing particles are protons released from the Sun during a solar flare. Figure 1.20 shows the production rates for protons of various initial energy. The protons are

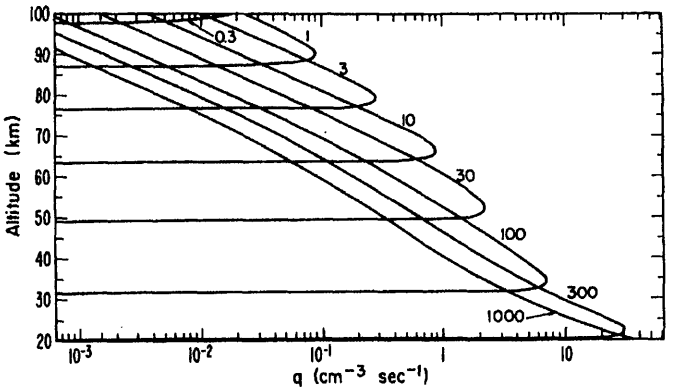

Figure 1.20: Production rates of monoenergetic protons of various initial energies (After *Reid* (1974)

more energetic than the auroral electrons, and lose energy with interactions with particles generally in the mesosphere. Proton events will ionize at lower altitudes than auroral electrons.

1.5.2 Loss Processes

The dominant loss processes in the ionosphere are dependent on altitude. At high altitudes recombination is dominated by positive ions. Electrons recombine with positive ions, in a process known as radiative recombination:

$$X^+ + e \rightarrow X \tag{1.24}$$

where X is species in the atmosphere, then the rate of electron loss is:

$$L = \alpha \left[X^+\right] N = \alpha N^2 \tag{1.25}$$

where N is the electron density, and is equal to the ion density $[X^+]$ and α is the recombination coefficient. At equilibrium:

$$q = \alpha N^2 \tag{1.26}$$

Combining with the Chapman production function this describes the α-Chapman layer. Electrons attaching to neutral particles to form negative ions is another form of electron loss. This process becomes a dominant process at higher latitudes. This process is described by:

$$M + e = M^- \tag{1.27}$$

where M is the neutral molecules. The rate of electron loss is:

$$L = \beta N \tag{1.28}$$

where β is the attachment coefficient. At equilibrium, again L=q and applying the Chapman production function this is described as a β-Chapman layer. β varies with height as it depends on the concentration of the neutral molecules in the atmosphere. The height h_t at which the behavior of recombination between α and β processes changes is:

$$\beta(h_t) = \alpha N \tag{1.29}$$

For the loss processes of the D region the significance of negative ions should be taken into account. Electrical neutrality means that N_e+N_-=N_+ where N_e is concentration of electrons, N_- is the concentration of negative ions and N_+ is the concentration of positive ions. As the negative ions can recombine with the positive ions the balance between the loss and production is expressed as:

$$q = \alpha_e N_e N_+ + \alpha_i N_- N_+ \tag{1.30}$$

where α_e is the recombination coefficient for positive ions and electrons and α_i is the recombination coefficient for positive and negative ions. The ratio between the negative ion and electron concentration is represented by λ (although it is not related to wavelength). Therefore in terms of λ, N_-=λN_e and N_+=$(1+\lambda)N_e$, and

the production rate becomes:

$$q = (1 + \alpha)(\alpha_e + \lambda\alpha_i)N_e^2 \tag{1.31}$$

Even in the presence of negative ions the electron density is still proportional to the square root of the production rate, only the magnitude is changed. $(1+\alpha)(\alpha_e+\lambda\alpha_i)$ is often referred to as the effective recombination coefficient, and is usually calculated either empirically or experimentally due to the complex nature of the D region ionosphere.

In the E and F1 layers the dominant process is dissociative recombination:

$$e + XY^+ \rightarrow X + Y \tag{1.32}$$

Dissociative recombination in the E and F1 layers is 10^5 times faster than radiative recombination. The primary ions in the E region are N_2^+, O_2^+ and O^+. Therefore the main recombination reactions are:

$$\begin{aligned} e + O_2^+ &\rightarrow O + O \\ e + N_2^+ &\rightarrow N + N \\ e + NO_2^+ &\rightarrow N + O \end{aligned} \tag{1.33}$$

Heavier ions such as Fe^+, Mg^+, Ca^+ are also present in the E region. These ions cannot recombine dissociatively and have a recombination coefficient typical for radiative recombination. This means that relatively they have a long lifetime. The F region primary ion is O^+ which is converted into a molecular ion by a charge exchange process:

$$O^+ + N_2 \rightarrow NO^+ + N \tag{1.34}$$

The molecular ion then reacts with an electron in the usual manner:

$$NO^+ + e \rightarrow N + O \tag{1.35}$$

The final term in the continuity equation expresses the loss of electrons due to transport. The transport of electrons can be in both horizontal and vertical directions. Vertical transport is an important loss mechanism in the F2 region where the O^+ chemical lifetime is comparable to the vertical transport time. Ions 'stored' in the F2 region from the day, due to the plasma lifetime of the F region being several hours, slowly diffuse downwards and resupply the F_1 region, until they reach a point where they can recombine through dissociative recombination (*Shirley and Fainbridge* (1997)). At polar latitudes there is the 'polar wind'; a constant outflow of plasma along the field lines.

1.5.3 Ionospheric Convection

The connection between the solar wind and the magnetosphere constrains the magnetospheric plasma to have a convection pattern that maps down to the high latitude ionosphere. The electric field from the solar wind is mapped down into the ionosphere causing $\mathbf{E} \times \mathbf{B}$ plasma drift that is known as convection. For a southward IMF, when a closed geomagnetic field lines connect with the IMF on the dayside magnetosphere the open field lines and plasma convect antisunward across the polar cap. When the foot of this field line has moved from the polar cusp boundary on the dayside to the nightside boundary the magnetic field which is now located in the magnetotail reconnects, the newly formed closed field line then convects around the polar cap back to the day side magnetosphere. The associated $\mathbf{E} \times \mathbf{B}$ drift in the ionosphere caused by the magnetospheric electric current is shown in figure 1.21. This is a idealized two cell convection pattern that can be seen under some conditions but is usually more complicated. As well as this convection the ionospheric plasma has a tendency to co-rotate with the Earth and needs to be taken into account when plotting plasma convection.

The high-latitude ionospheric convection pattern is dependent on the solar wind, and in particular the orientation of the IMF (*Belenkaya* (1998)). When

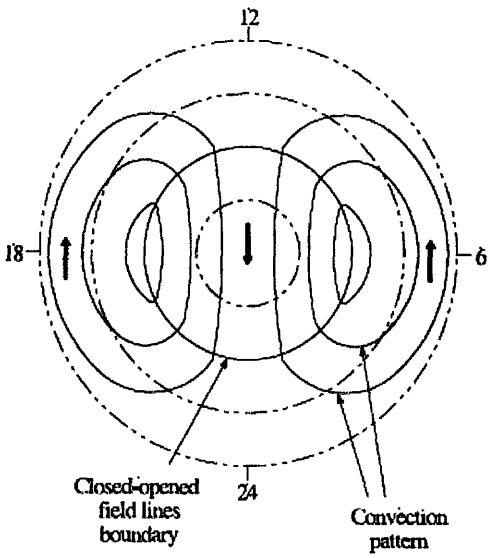

Figure 1.21: Scheme of high latitude two-cell convection. Motion is generally antisunward in the polar cap region, from noon to midnight, with return flow in the auroral region. The closed field line boundary is approximately where the motion changes from antisunwards to Sunwards. (After *Yohsuke and Abraham* (2007))

the IMF is southward, $B_z < 0$ the two cell convection pattern is exhibited. The potential drop across the solar wind which determines the convection speed varies with solar wind and dynamic pressure (*Schunk and Nagy* (2000)). The direction of B_y however describes how the potential drop is distributed across the two cells. For $B_y \approx 0$, the potential drop is symmetrical across both convection cells and the pattern is the one seen in figure 1.21. When $B_y \neq 0$ the two-cell convection pattern is asymmetrical with enhanced convection in the dusk cell for $B_y < 0$ and enhanced convection in the dawn cell for $B_y > 0$ in the northern hemisphere. Figure 1.22 shows a model of the convection patterns for a southward IMF in the northern ionosphere for $B_y > 0$ and $B_y < 0$. In the southern hemisphere the asymmetry in the convection cells is reversed for a given B_y.

For a northward IMF the convection patterns become more complicated and distorted, with Sunward convection occurring in the polar cap. The structure of the convection originally thought to be a highly distorted two cell convection

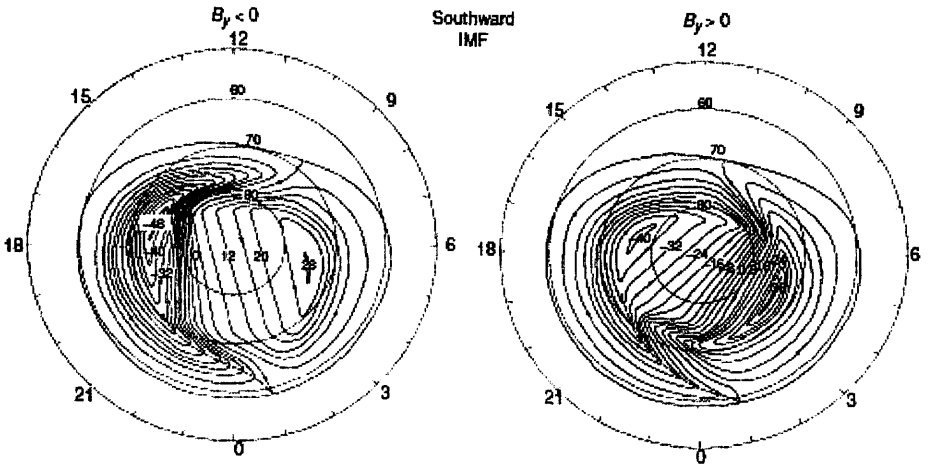

Figure 1.22: Plasma convection in northern polar region for southward IMF. Left pane is for negative IMF B_y and right pane for positive IMF B_y (After *Heppner and Maynard* (1987)

pattern, is now thought to have a multi-cell structure. For $B_y = 0$ a four cell pattern occurs, when there is either a negative or positive B_y one of the convection cell expands while another cell shrinks, giving at large value of B_y the appearance of a three cell convection pattern. Figure 1.23 shows a model of the convection patterns for southern hemisphere for varying B_y during northward B_z.

1.5.4 Ionospheric Currents

Electrical conductivity of the ionosphere is important to the study of the magnetosphere-ionosphere coupling process. Conductivity occurs due to collisions from ions and neutrals in the ionosphere allowing electron-ion drift due to the electric field and the geomagnetic field (*Maeda* (1977),*Senior et al.* (2007)). The currents flow in accordance to Ohm's law:

$$\mathbf{J} = \sigma \mathbf{E} \tag{1.36}$$

In the ionosphere there are three different conductivities, (i) Pedersen, (ii) Hall and (iii) parallel. The Pedersen conductivity is the plasma conductivity in the

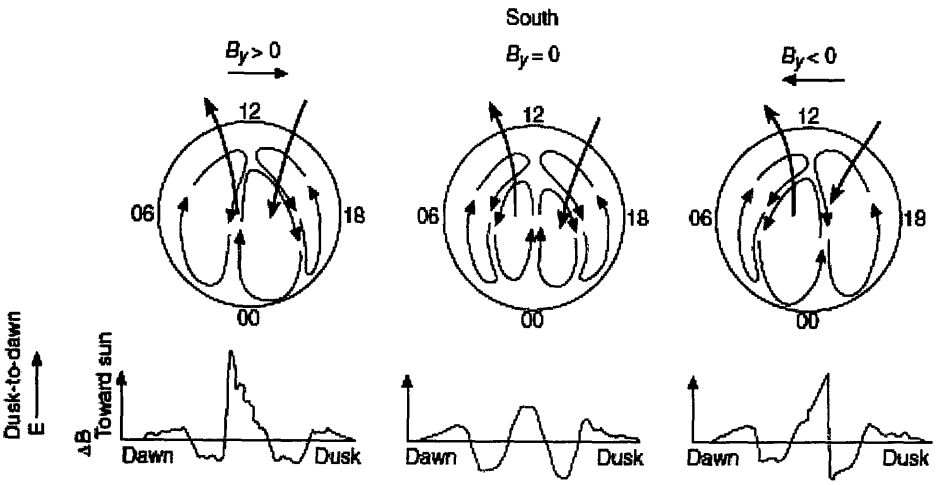

Figure 1.23: Plasma convection in southern polar region for strongly northward IMF. Left pane is for positive IMF B_y, middle plane is for B_0=0, right pane for negative IMF B_y. The traces of $\Delta\mathbf{B}$ observed by a dawn to dusk orbiting satellite are shown at the bottom (After *Potemra et al.* (1984)

direction of $\mathbf{E}_\perp$, the electric field perpendicular to the magnetic field. The Hall conductivity is the conductivity of the plasma in the direction that is perpendicular to both the electric field and magnetic field. The parallel conductivity is the plasma conductivity in the direction of the magnetic field $\mathbf{B}$.

The three conductivities depend on the electron density N_e and thus are close to zero where the concentration is low. The conductivities can be separated into three regions. Below 80km the electron-ion (υ_i) and electron-neutral (υ_e) collision frequencies (section 1.5.6), are greater than the ion gyrofrequency (ω_i) and electron gyrofrequency (ω_B) respectively. In this region the collisions with neutrals dominates and the particles don't feel the magnetic field. In this regions the conductivities are very low, due to the low concentration of N_e. σ_H is very small and $\sigma_p \approx \sigma_\parallel$.

Between 90 and 120km, $\upsilon_i \gg \omega_i$ and $\upsilon_e \ll \omega_B$. In this region the electrons are trapped in the magnetic field lines and cannot move freely across them. Ions are dominated by collisions with neutrals. In this region currents perpendicular

to **B** are likely to form due to the difference between the ions and electrons. The conductivities perpendicular to the magnetic field (σ_p, σ_H) maximize in this region around 110km, where the perpendicular current maximizes.

The final region, above 150km, $\upsilon_i \ll \omega_i$ and $\upsilon_e \ll \omega_B$ all charged species are trapped in the magnetic field and cannot move freely perpendicular to the magnetic field. The perpendicular conductivities in this region become negligible, while the parallel conductivities increase to a constant value around 50km. Figure 1.24 shows typical vertical profiles for the three conductivities. Hall conductivities are dominated by electrons, whereas Pedersen conductivities are dominated by the ion species.

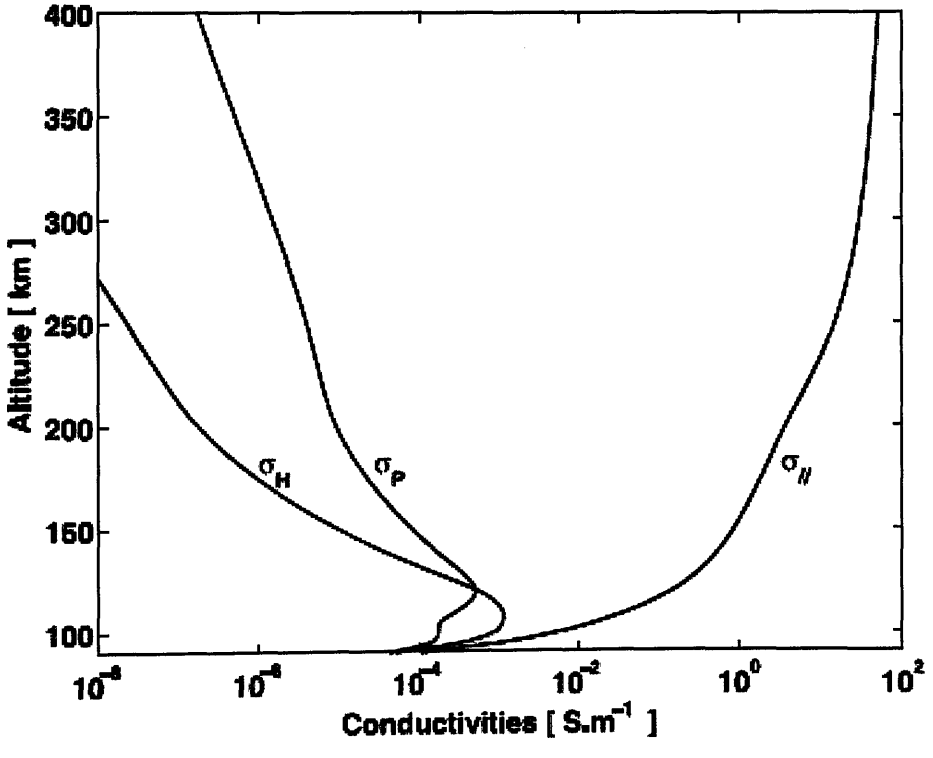

Figure 1.24: Typical vertical profiles for the ionospheric conductivities. σ_p: Pedersen conductivity, σ_H: Hall conductivity, $\sigma_\parallel$ parallel conductivity. (After *Yohsuke and Abraham* (2007))

1.5.5 Radio waves in the Ionosphere

For electromagnetic waves that travel through an ionized medium the refractive index is complex:

$$n = \mu - j\chi \tag{1.37}$$

where μ represents the real part and χ represents the imaginary part. The refractive index in this case is dispersive; waves at different frequencies travel at different speeds. The formula for the refractive index can be represented by the Appleton-Hartree equation.

$$n^2 = 1 - \frac{X}{1 - jZ - \frac{Y^2 \sin^2\theta}{2(1-X-jZ)} \pm \left[\frac{Y^4 \sin^4\theta}{4(1-X-jZ)^2} + Y^2\cos^2\theta\right]^{\frac{1}{2}}} \tag{1.38}$$

where:

$$\begin{aligned} X &= \frac{\omega_N^2}{\omega^2} \\ Y &= \frac{\omega_B}{\omega} \\ Z &= \frac{\upsilon}{\omega} \end{aligned} \tag{1.39}$$

where ω_N is the angular plasma frequency, ω_B is the electron gyrofrequency, υ is the electron collision frequency, j is $(-1)^{\frac{1}{2}}$, ω is the angular frequency of the wave and θ is the angle between the propagation direction and the geomagnetic field. The derivation of the Appleton-Hartree equation can be found in *Ratcliffe* (1959). The plasma frequency is a fundamental principle of an ionized medium and is defined as:

$$\omega_N = \left(\frac{\mathrm{Ne}}{\epsilon_0 \mathrm{m}}\right)^{\frac{1}{2}} \tag{1.40}$$

where N is electron number, e is electron charge, ϵ_0 is the permittivity of free space and m is the mass of an electron. Similarly the electron gyrofrequency is defined

as:

$$\omega_B = \frac{\mathrm{Be}}{\mathrm{m}} \tag{1.41}$$

where B is the magnetic field strength and e and m are again the electron charge and mass respectively.

If we assume that a radio wave encounters collisions, (Z≠0) and that the wave propagation is in the direction of the magnetic field $\theta \sim 0$, which for absorption in the auroral ionosphere are sensible assumptions, equation 1.38 becomes:

$$n^2 = (\mu - j\chi)^2 = 1 - \frac{X}{1 - jZ} = 1 - \frac{X}{1 + Z^2} - j\frac{XZ}{1 + Z^2} \tag{1.42}$$

The absorption coefficient for a wave is $\kappa = \omega\chi/\mathrm{c}$ (nepers/meter), it can be shown by splitting equation 1.42 into real and imaginary parts and substituting κ and ω_N that:

$$\kappa = \frac{\omega}{2c\mu}\frac{XZ}{1 + Z^2} = \frac{\mathrm{e}^2}{2\epsilon_0 \mathrm{mc}\mu}\frac{\mathrm{N}\upsilon}{\omega^2 + \upsilon^2} \tag{1.43}$$

In the ionosphere there are two special cases that apply. These are known as deviative, and non-deviative absorption.

Deviative Absorption

Deviative absorption occurs primarily in the F-region of the ionosphere, where the collision frequency, υ is small, $\mathrm{Z}^2 \ll 1$. If υ is small then $\mu^2 = 1 - X$, therefore this leads to:

$$\kappa = \frac{\upsilon}{2\mathrm{c}}\left(\frac{1}{\mu} - \mu\right) \tag{1.44}$$

When $\mu \to 0$ absorption maximizes.

Non-deviative absorption

The second case occurs mainly in the D-region ionosphere. In this case $\mu = 1$ and is known as deviative absorption as there is no bending of the waves. For this case equation 1.43 becomes.

$$\kappa = \frac{e^2}{2\epsilon_0 mc} \frac{N\upsilon}{\omega^2 + \upsilon^2} \tag{1.45}$$

Integrating equation 1.45 along the path length and multiplying by 8.69 to convert from nepers/meter to decibels/meter the total absorption due to non deviative absorption is:

$$A = 4.5 \times 10^{-5} \int \frac{N\upsilon}{(\omega \pm \omega_B)^2 + \upsilon^2} \mathrm{dl\ dB} \tag{1.46}$$

In equation 1.46 ω has been replaced by $\omega \pm \omega_B$ to distinguish between ordinary (O-mode) and extraordinary (X-mode) waves as they are not absorbed to the same extent. The 'O', or Ordinary mode has an electric field vector that is parallel to the static magnetic field. This leads to a dispersion relation that is the same if it was in an unmagnetized plasma, whereas The 'X' or extraordinary wave has an electric field vector that is perpendicular to the static magnetic field and leads to a more complicated dispersion relation, (*Piel* (2010)). Over the following chapters this thesis will deal with deviative absorption in the D-region ionosphere.

1.5.6 Collision Frequencies in the Ionosphere

Absorption in the ionosphere is dependent on the collision frequencies of electrons with the neutral and ion species present. Calculation of the effective collision frequency is done by:

$$\upsilon_{eff} = \frac{4}{3} n Q(T_e) \langle u \rangle \tag{1.47}$$

where n is the number of colliding particles, $Q(T_e)$ is the momentum transfer cross section (dependent on electron temperature) and $\langle u \rangle$ is the mean electron velocity (*Danilkin et al.* (2005)). The effective collision frequencies can be described as the

summation of the effective collision frequencies for all heavy components (x) of the plasma:

$$\upsilon_{eff} = \sum_{x} \upsilon_{effx} \tag{1.48}$$

To calculate the effective collision frequencies studies of laboratory data and theoretical derivations to obtain convenient expressions from the momentum transfer cross section are required, eg. *Banks* (1966).

1.6 Geomagnetic Storms

During geomagnetic storms the magnetic configuration of the magnetosphere is altered significantly, with stretching of the nightside magnetic field lines, increases in the flux of the magnetotail and shifting of the polar cusps to lower latitudes. (*Yohsuke and Abraham* (2007)).

A geomagnetic storm is characterized by a depression in the **H** component of the magnetic field, that can last for several days. The depression of the horizontal component can be monitored using the Dst index (section 2.7.2). A geomagnetic storm can be defined by the minimum Dst value that it obtains. *Gonzalez et al.* (1994) classifies storms in the following criteria: Dst of -100nT or less is an intense storms, -50nT to -100nT is a moderate storm and between -30nT and -50nT is a weak storm.

Panel (a) of figure 1.25 shows the Dst response to what is known as a 'classic' geomagnetic storm. The storm would commence with a sudden storm commencement (SSC), which is observed as a rapid positive increase in the **H** component of the magnetic field. The SSC is the compression of the dayside magnetosphere by enhanced solar wind pressure. This is followed by the initial phase, a period of enhanced magnetic field caused by the SSC. After the initial phase the main phase occurs, this is a period of substantial reduced field ($\sim$ 1% of the Earths equtorial

field). The main phase lasts for several hours. Finally the recovery phase is where the magnetic field slowly returns to it's original level. The recovery phase can last for several days.

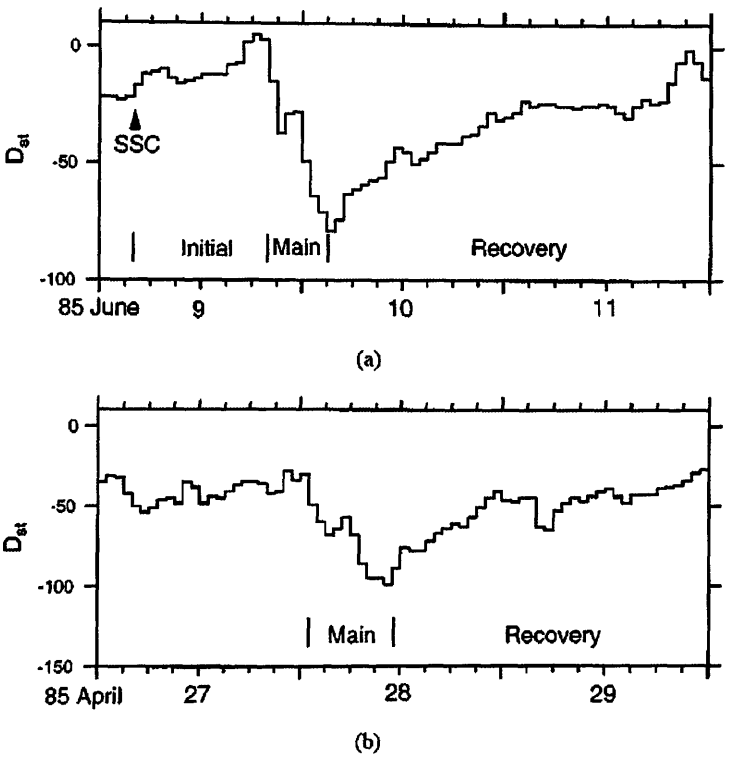

Figure 1.25: (a) Dst index for a classic geomagnetic storm which begins with a sudden storm commencement. (b) Deviation from classic geomagnetic storm, with no SSC or initial phase. (After *Lui* (2000))

Panel (b) of figure 1.25 shows a deviation from the classic storm, where the SSC and initial phase are ill defined. The initial phase after the SSC is due to the IMF. During the initial phase the IMF is northward so little energy actually enters the magnetosphere. The depression of the **H** component is due to the injection of particles into the magnetosphere causing an increase in the equatorial ring current.

Intense geomagnetic storms are driven by the dawn to dusk electric field in the solar wind (*Yohsuke and Abraham* (2007)). The electric field is controlled by the solar wind velocity and the southward IMF. Of the two parameters it seems that the southward IMF is the more important parameter due to its variability.

There are two main processes for the cause of geomagnetic storms, interplanetary coronal mass ejections and co-rotating interaction regions (see sections 1.2.3 and 1.3.2).

Brovosky and Denton (2006) compared CIR and CME driven storms and discussed the differences on geomagnetic activity produced by CIRs and CMEs. The main differences between the two drivers are that CME-driven storms are briefer than their CIR counterparts. They have stronger ring current, have solar energetic particle events and can produce new radiation belts, auroras and geomagnetically induced currents. CIR's have hotter plasma sheets and produce higher fluxes of relativistic electrons. CME events occur randomly but have a maximum occurrence rate at solar maximum, whereas CIR-driven storms occur mainly in the declining phase in the solar cycle and recur with a 27 day period.

1.7 Substorms

The substorm was first introduced by *Akasofu* (1964) to describe a series of auroral disturbances as seen from ground based observations, characteristically showing three distinct phases, (i) the growth phase, (ii) expansion phase, (iii) recovery phase. The growth phase of the substorm sees energy being stored in the near-Earth magnetotail before the onset of the expansion phase due to a southward IMF (B_z). The start of the expansion phase is known as the substorm onset and is marked with a brightening of an auroral arc, with expansion in the nightside. Part of the near-Earth magnetotail current disappears and closes themselves through ionospheric current systems (Birkeland currents), creating the substorm current wedge. In the magnetosphere high speed plasma flows are observed within the plasma sheet with plasmoids detected in the far tail and injected accelerated particles (10's of KeV) seen near geostationary orbit. During the recovery phase the

magnetosphere returns to conditions before the start of the substorm. A substorm usually lasts between 1-2 hours.

The start of the expansion phase and if it is triggered by a reduction in energy from solar wind effects such as a Northward turning IMF or a vast reduction in solar wind velocity, or by a internal trigger is a widely debated topic. *Lyons et al.* (1997) argued that nearly all expansion phase onsets can be attributed to a northward turning IMF, whereas *Henderson et al.* (1996) argues that many substorms are triggered internally. *Hsu and McPherron* (2004) show that both triggered and non-triggered substorms are possible.

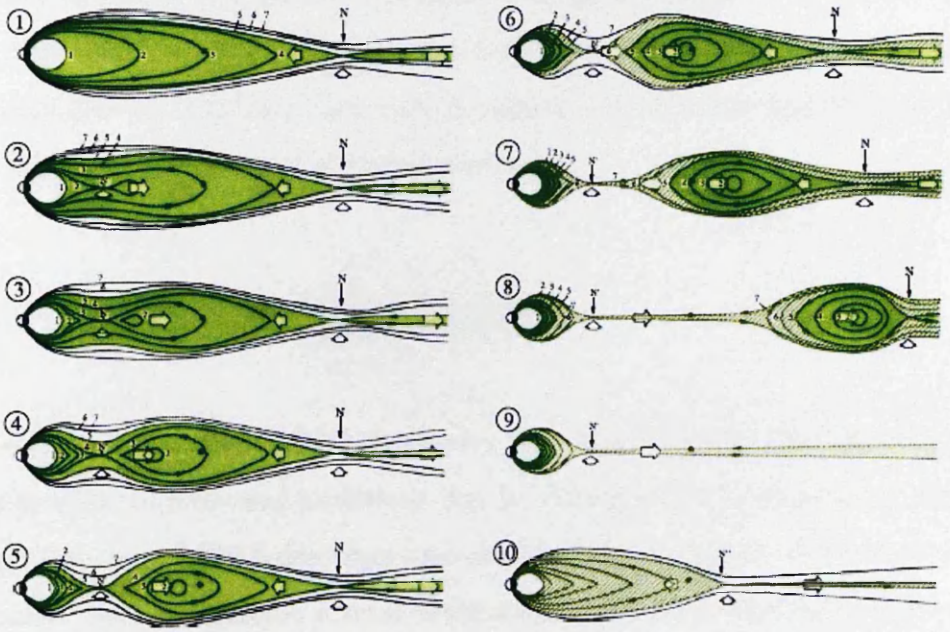

Figure 1.26: Near Earth Neutral Line sequence of events of a substorm. Green arrows indicate plasma flow (After *Hones* (1984))

The details of how a substorm occurs is a matter of scientific research and is still uncertain. The most developed model of the substorm is the **n**ear-**e**arth **n**eutral **l**ine (NENL) (eg *Baker et al.* (1996)). Figure 1.26 shows a diagram of the life cycle of a substorm according to the NENL model. The NENL model begins with a southward turning of the IMF. This causes a thinning of the plasma sheet

leading to the formation of a new neutral line close to the Earth. Closed plasma sheet field lines reconnect causing a flow pattern of earthward and tailward flow of plasma from the neutral point. At some point open field lines reconnect creating an outward flow of plasma carrying mass and energy into the solar wind, known as a plasmoid. At the same time the earthward flow provides the energy for the substorm.

A second theory for the substorm is the current sheet-disruption model (eg *Lui* (1991)). In this model the thinning of the plasma sheet is the same as in the NENL model. The cross tail current is disrupted by nonadiabatic ions creating waves in the plasma sheet that create an anomalous resistance. The tail current must flow due to a high inductance and does this by diverting through field lines. Other models for substoms have been proposed, see *Kivelson and Russell* (1995) for a description of some of the other theories.

1.8 Particle Precipitation

As described in section 1.5.5 radio waves that pass through the ionosphere are absorbed due to increased ionization due to among others precipitating electron and protons. Section 2.2 describes instrumentation to monitor absorption of cosmic noise. Here we describe several of the more common precipitation events that cause the absorption of cosmic noise.

Midnight Auroral Absorption

During the onset of a substorm, there is associated absorption in the nightside auroral oval caused by the precipitation of energetic electrons with energies of 10-100keV. Particles of these energies precipitate into the ionosphere to around 70-100km (*Stauning* (1996)). Short duration spikes associated with substorm auroral

radio absorption are discrete patches of absorption, with variable velocities of 2-3kms^{-1} and last for a few minutes (*Hargreaves et al.* (1996)). Night time spike events studied by *Aminaei et al.* (2006) where spike events were grouped into four types of event and can be seen in figure 1.27. The 4 types of spike where classified

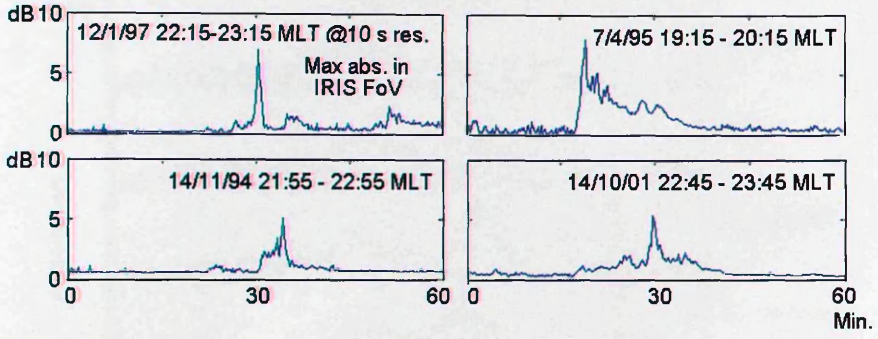

Figure 1.27: Typical examples for 4 types of absorption spike events, measured at Kilpisjärvi (After *Aminaei et al.* (2006))

as (i) spikes without injection absorption, which have the shortest duration of a few minutes, (ii) spikes followed by injection absorption, (iii) spikes that occur after absorption injection and have a duration of a few minutes and (iv) spikes embedded in injection absorption and have a duration of tens of minutes. Injection absorption is defined as the background absorption that appear alongside the spikes. The occurrence of the spikes is dependent on the geomagnetic activity.

1.8.1 Slowly Varying Absorption

A second absorption type associated with substorms is what is termed slowly varying absorption (SVA). Injected electrons during the main phase of a substorm are trapped on field lines and begin to drift due to the combined effects of the gradients in the geomagnetic field and the magnetospheric electric fields. Precipitation of these electrons into the morning sector occur due to small pulses in solar wind pressure, driving wave particle interactions (*Kavanagh et al.* (2002)). Particles are of the energies of 30-300keV, generally being hardened during the

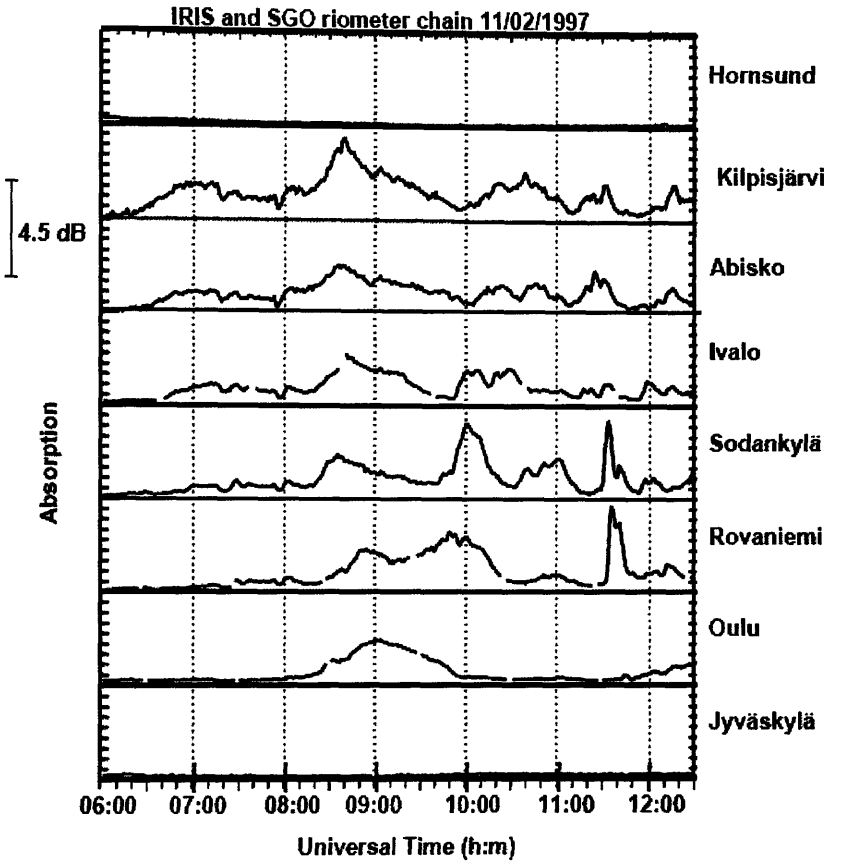

Figure 1.28: Slowly varying absorption for 11 February 1997. Instruments are listed in descending magnetic latitudes. (After *Kavanagh et al.* (2002))

drift to the dayside, Figure 1.28 shows the absorption due to a SVA event over a range of geomagnetic latitudes for the 11 February 1997. The duration of SVA events is usually between half an hour to a few hours following substorm activity.

Sudden Commencement Absorption

Increases in solar wind pressure that compress the dayside magnetosphere causes an increase in the **H** component of the Earth's geomagnetic field. Accompanying these sudden commencements can be precipitation of normally trapped electrons in the range of 30-3000keV. This enhanced ionization causes increases in radio

wave absorption. Figure 1.29 shows cosmic noise absorption over Kilpisjärvi due to a sudden commencement on the 3rd April 2004. The sudden commencement begins at 14:10UT with a fast increase in absorption, maximising at 0.8dB a few minutes later. Impulsive electron precipitation can be caused by whistler

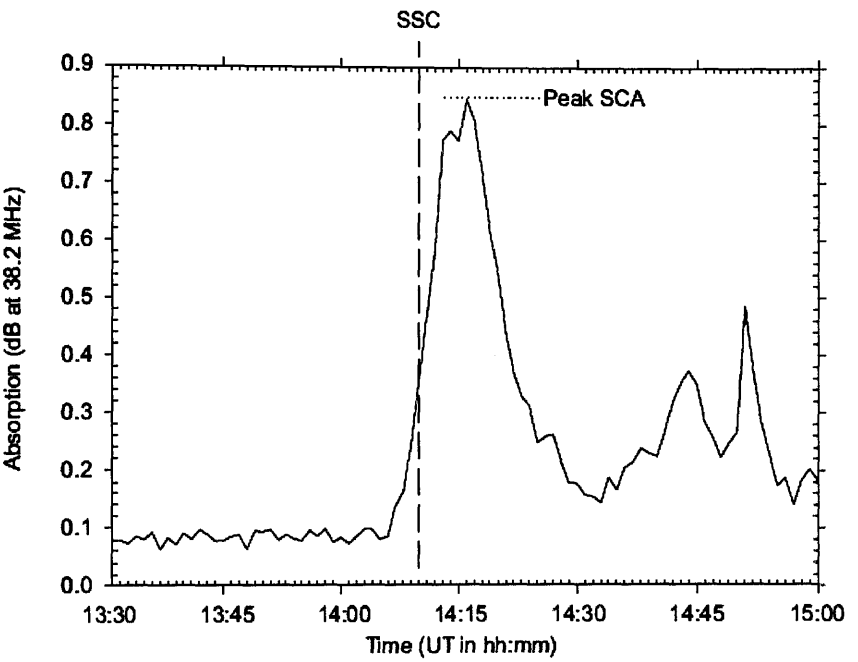

Figure 1.29: Absorption due to Sudden Commencement at Kilpisjärvi on 3rd April 2004 (After *Ritchie and Honary* (2009))

cyclotron instability (*Coroniti and Kennel* (1970)), with the magnetic compression due to high solar wind pressure being an ideal method for causing the whistler cyclotron instability. First observations of **S**udden **C**ommencement **A**bsorption (SCA) was carried out by *Brown et al.* (1961) with observations by *Ortner et al.* (1962) showing absorption was at its maximum near the central line of the auroral zone. SCA is as likely to occur during the night time as it is during the day time (*Ritchie and Honary* (2009)), but during geomagnetically quiet times the change in the Earth's geomagnetic field due to the solar wind shock must reach a certain threshold, (ΔB_{th}) for SCA to occur (*Osepian and Kirkwood* (2004)).

Dayside Absorption

Absorption during the afternoon sector is the topic of investigation in chapter 4. Investigations by *Ranta et al.* (1997) show highly localized absorption observed, with dimensions ranging from 30km by 30km up to as much as 180km by 130km. These spikes had short durations of a few minutes with some showing a southward motion. Figure 1.30 shows an example of a dayside absorption spike. The possi-

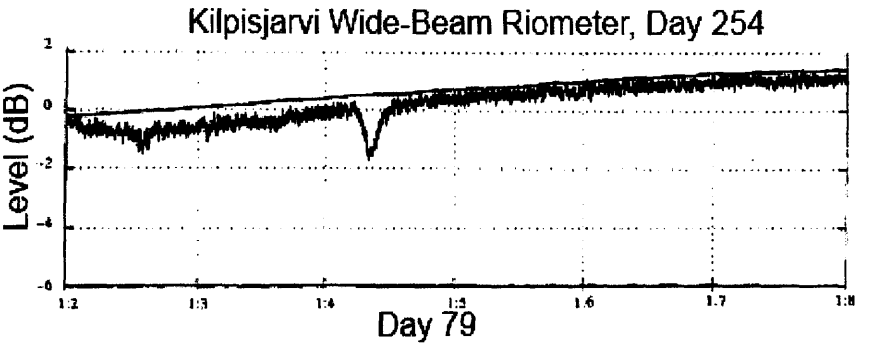

Figure 1.30: Recording of dayside absorption at Kilpisjärvi on 11 September 1994 (After *Ranta et al.* (1997))

ble cause of this precipitation was explained to be due to the eastward traveling protons after a substorm and possible electromagnetic ion cyclotron interaction causing precipitation of very hard electrons (<100keV).

Sudden Cosmic Noise Absorption

During Solar flares the emission of soft X-rays can increase by several orders of magnitude. The enhanced X-ray emissions can cause enhancements of the D and low E region ionization over the whole of the solar illuminated part of the Earth. This enhancement can cause cosmic noise absorption, which may last for the duration of the flare, 2-10 minutes (*Stauning* (1996)). Accompanying the solar flare is usually strong radio noise that can interfere with observations.

Polar Cap Absorption

Also associated with solar flares is **P**olar **C**ap **A**bsorption (PCA). During larger solar flares, the sun emits large amounts of high energy electrons, protons and α particles. Protons with energies between 1-100 MeV, (*Sellers et al.* (1977)) are the main cause of ionization, causing ionization between 30-80km. The region that is affected by PCA extends from the poles to 60° - 65° geomagnetic latitude, with PCA events lasting from a few hours to many days (*Perrone et al.* (2004)). Figure 1.31 shows an example of a PCA event with measurements of proton flux

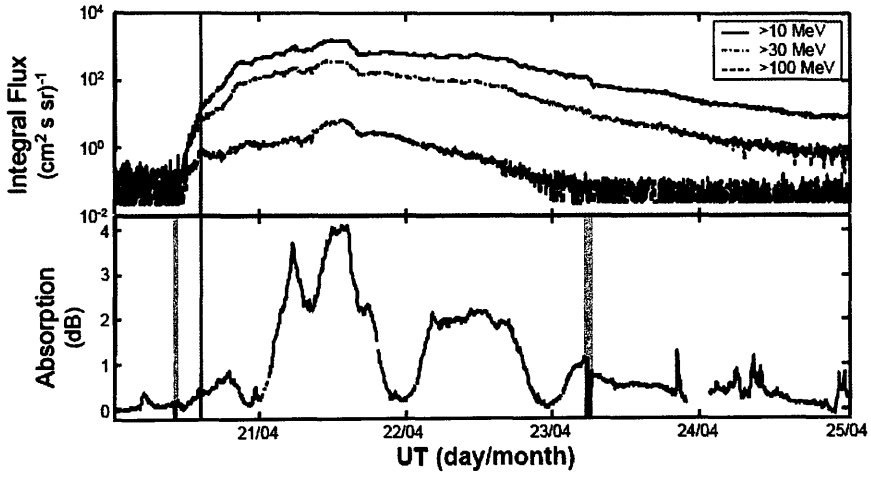

Figure 1.31: Polar cap absorption event from April 1998. Absorption is shown on the bottom panel. Top panel shows proton flux measured on GOES-8 Satellite for >10MeV, >30MeV and >100MeV. (After *Kavanagh et al.* (2004a)

at Geostationary orbit. As can be seen in figure 1.31 there is a large difference between the magnitude of absorption during the day and during the night time, due to the formation of negative ions during the night time which act to remove electrons (*Stauning* (1996)).

1.9 Summary

This chapter provides a brief overview and summary of the main areas of the solar terrestrial environment. As this thesis is primarily concerned with precipitation of electrons into the auroral ionosphere and the resultant absorption of cosmic noise, particular detail has been given to the electric fields, magnetic fields and particle motion present in the ionosphere and magnetosphere. The Appleton-Hartree equation of refractive index is presented and discussed as it is used to describe the absorption of charged particle through an ionized medium. Additionally some of the principle causes of auroral absorption are outlined.

The absorption of cosmic noise due to the precipitation of charged particles is placed in context by describing the Sun-Earth connection, through the solar wind and interaction with the Earths magnetosphere as well as some of the principle phenomena that drive this geomagnetic activity. This includes high speed solar streams that originate from coronal holes on the Suns surface, coronal mass ejections and solar flares.

Chapter 2

Instrumentation and Indicies

2.1 Introduction

This thesis is concerned with energetic particle precipitation into the atmosphere. The main instruments used for this study are the riometer, with secondary data from incoherent scatter radar, data from the AARDDVARK network of VLF receivers, and satellites. This chapter outlines these various instruments as well as the main geomagnetic indicies.

2.2 Riometry

Developed in the 1950s, the riometer (**R**elative **I**onospheric **O**pacity **METER**) is a sensitive self-balancing radio receiver used to monitor the absorption of cosmic noise in the ionosphere (*Little and Leinbach* (1959)). As the method requires propagation of radio waves through the ionosphere, the frequency must be greater than the critical frequency, known as f_0F2. Measurement of the received power is accomplished by the rapid switching between the receiver input and a local noise source. The current passing through the noise diode is constantly altered

to keep the power of the two noise sources equal. The power of the local noise source is proportional to the current passing through it. Therefore recording of the current is only required for the measurement of the antenna power. (*Little and Leinbach* (1958)). This setup uses the receiver as a null detector, meaning that measurements are not affected by variations in the receiver gain.

Absorption measured in dB is defined as the log ratio of the received power with reference to a day were no absorption has occurred. This is expressed as

$$A = -10\log_{10}\left(\frac{P}{P_0}\right) \tag{2.1}$$

Where P is the received power, and P_0 is the power in the absence of absorption. Due to the non-uniform nature of the cosmic noise power across the sky, it is necessary to create quiet day curves (QDC) which represent the variation of cosmic noise power in the absence of absorption over the course of a sidereal day. Seasonal variations in the QDC, due to solar ionization of the D-region require the regular creation of QDCs. *Browne et al.* (1995) describes a relatively simple method for the creation of the QDC. Data is arranged into 14 sidereal days. The median is then taken for 10 minute periods for each day. Then, the mean of the second and third highest values is calculated. This is usually a good estimate of the quiet day value. Interpolation between the 10 minute values allows calculation of 1 second resolution of the quiet day values. Manual adjustment of the quiet day curves can reduce errors to an accuracy in the order of 0.01dB. More sophisticated methods of QDC generation have been investigated such as including inflection point (*Krishnaswamy et al.* (1985)) and maximum density methods (*Drevin and Stoker* (1990)) which give similar accuracy. Figure 2.1 shows a typical quiet day curve.

The first riometers were widebeam directional antennas, pointed in the zenithal direction. These widebeam riometers used Yagi or dipole antennas, and had

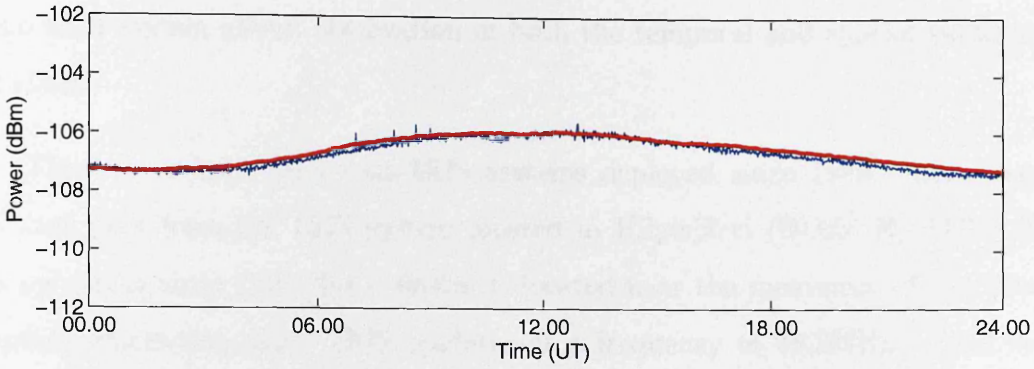

Figure 2.1: Quiet day curve for a typical quiet day. Red: quiet day curve, Blue: received power

beamwidths of around 30^o. Riometer beamwidths over the years became narrower, allowing more precise measurement of CNA (e.g. *Berkey* (1968)). The use of multiple closely located riometers pointing in different directions allowed coarse spatial measurements of particle precipitation (e.g. *Hargreaves* (1970)). Major advancement came with the development of the Butler matrix, a type of beam forming network, allowing the development of the imaging riometer. The imaging riometer has numerous narrow beams, allowing measurement of the spatial extent of CNA.

2.2.1 IRIS

The first **I**maging **R**iometer for **I**onospheric **S**tudies (IRIS) began operation in January 1988 at the South Pole station in Antarctica (*Detrick and Rosenberg* (1990)). The IRIS system comprises of 64 circularly polarized crossed dipole antennas, arranged in a 8x8 grid. Each antenna produces a vertical wide beam antenna pattern when placed a quarter wavelength above a perfect ground plane. The antennas have a horizontal separation of one half wavelength. The outputs of the antennas are fed into a phasing network, based on the Butler matrix resulting in 49 narrow beams, including a zenithly directed beam (*Browne et al.* (1995)). The beamwidths vary from 13° for the zenith beam to 16° at the corner beams.

The IRIS system allows observation of both the temporal and spatial variations of CNA.

There have been numerous IRIS systems deployed since 1989. This thesis utilizes data from the IRIS system located in Kilpisjärvi (69.05° N, 20.79° E). In operation since 1994 this riometer is located near the maximum of the mean auroral absorption zone. IRIS operates at a frequency of 38.2MHz, which is a protected scientific frequency. The IRIS beam projection is shown in figure 2.2.

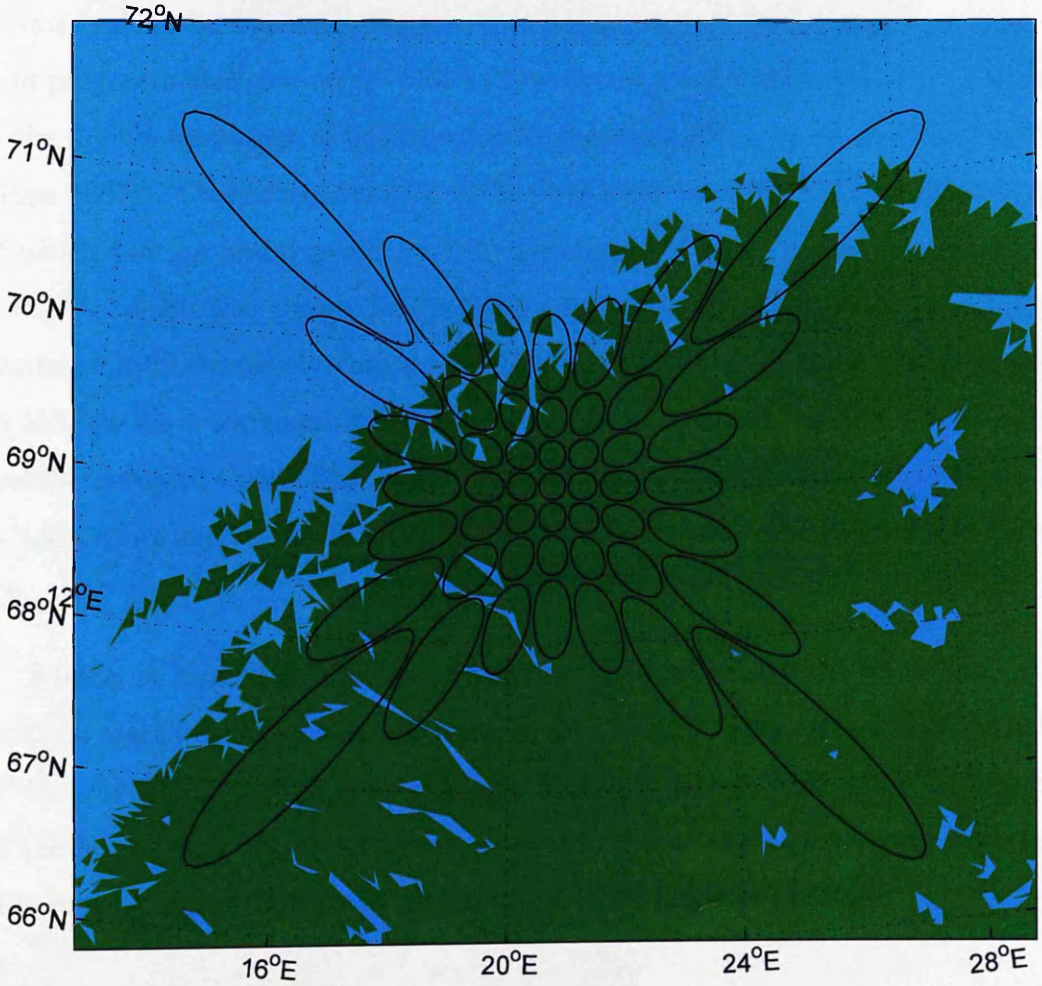

Figure 2.2: Riometer beam projection at 90km altitude for IRIS at Kilpisjärvi . The contours represent the -3dB point for each beam.

2.2.2 ARIES

The **A**dvanced **R**iometer **I**maging **E**xperiment in **S**candinavia (ARIES) system is a new development in imaging riomtery. ARIES employs a Mills cross antenna, compared to IRIS's filled array. ARIES comprises of a set of two perpendicular arms of 32 crossed dipole antennas. (*Honary et al.* (2005)). Beam forming is a two step process. The first step is to create two sets of 32 fan beams, 32 in the North-South direction and 32 in the East-West direction. The creation of fan beams is done by implementing one-dimensional digital Butler matrices using a field programmable gate array (FGPA) to evaluate a fast Fourier transform, which is the digital equivalent of analogue butler matrices, (*Honary et al.* (2011); *Grill* (June 2007)). Cross correlation of the fan beams allows 1024 beam combinations of which 556 are useful pencil beams. The beam-forming process is handled by a FGPA, which was chosen for its ability to handle the large amounts of data produced by the cross-correlation, (*Grill et al.* (2003)). Integration is comparable to IRIS, with a minimum integration time of $\sim$ 1 second, but the resolution is greatly increased with ARIES. The zenith beams of ARIES have a beam width of $\sim 4.5°$, compared to 13° for IRIS. The ARIES beam projection is shown in figure 2.3.

ARIES is located at Ramfjordmeon near Tromsø (69.63° N, 19.52° E). The location was chosen due to its proximity to the EISCAT facility and IRIS. The field of view for ARIES and IRIS overlap significantly, which will allow the estimation of the height of CNA, and the associated energies of the precipitating electrons (Chapter 3), a feat that would be impossible with just one riometer.

2.3 Incoherent Scatter Radar

Incoherent radar scatter is one of the most powerful ground based techniques for observing the ionosphere. From the early 1960s facilities have started using

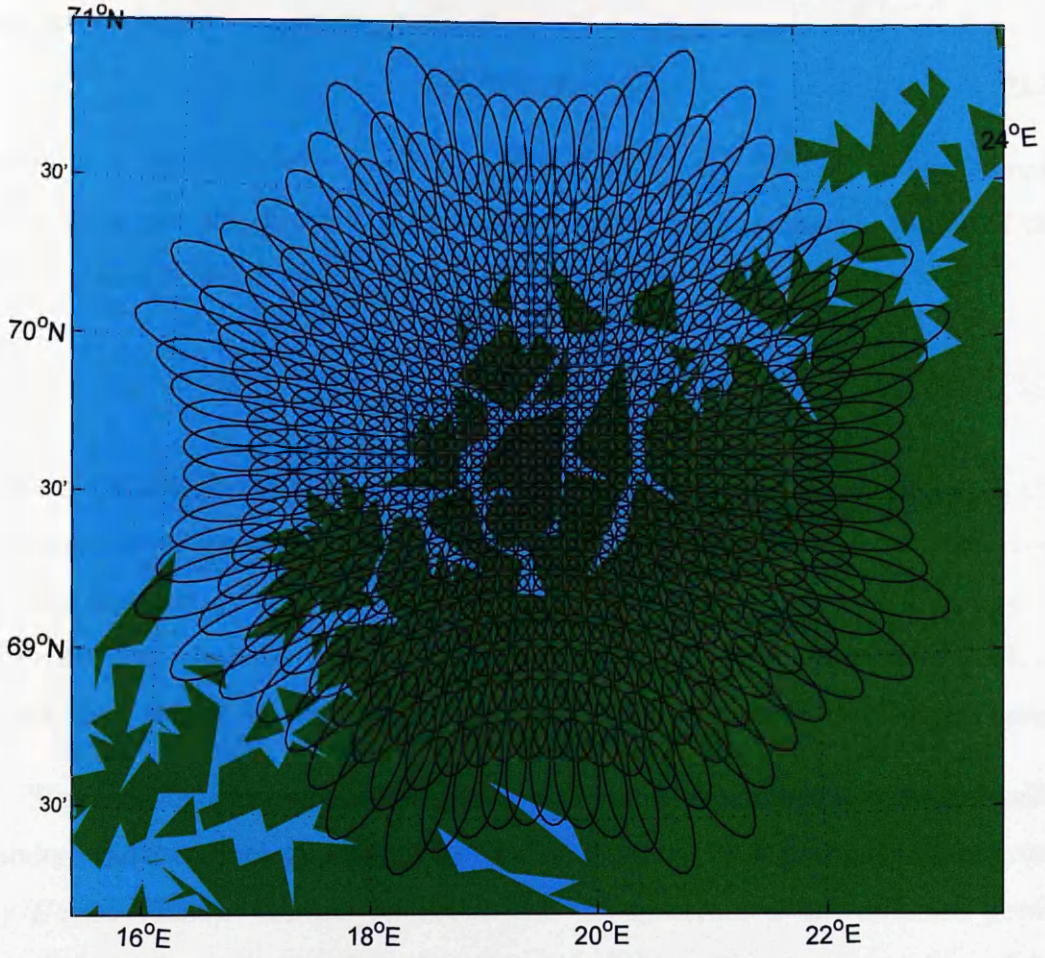

Figure 2.3: Beam projection at 90km altitude for ARIES at Ramfjordmoen. The contours represent the -3dB point for each beam.

powerful VHF and UHF radio transmitters to probe the makeup of the ionosphere. This section describes the basic theory of incoherent scatter and the facility from which data was used in this thesis.

2.3.1 Theory of Incoherent Scatter Radar

The founding principle of the Incoherent Scatter technique is based on *Thomson scatter*. In 1906 J.J. Thomson showed that the electron will scatter radiation with

a cross section:

$$\sigma_r = 4\pi \left(r_e \sin\psi\right)^2 \tag{2.2}$$

where ψ is the angle between the direction of the electric field of the electromagnetic wave and the direction of the observer and r_e is the classical radius of the electron and is defined as:

$$r_e = \frac{e^2}{4\pi\epsilon_0 m_e c^2} = 2.18 \times 10^{-15} m \tag{2.3}$$

Where e is the charge of an electron, m_e is the mass of an electron and ϵ_0 is the permittivity of free space. For the case of radar backscatter $\psi = 90^o$, the cross section becomes $\sigma_r = 4\pi r_e^2 = 1 \times 10^{-28} m^2$. For example, a sampled volume of $1.4 \times 10^{-28} m^3$ the total cross section would be $1.4 \times 10^{-5} m^2$ (*Hargreaves* (1992)), hence the need for a radar to be extremely sensitive to receive backscatter signal.

The case for using incoherent scatter as a viable experimental technique with modern radar technology was put forward by *Gordon* (1958) and put into practice by *Bowles* (1958). Gordon predicted that the spectrum of the reflected power would be of Gaussian shape and Doppler shifted due to the random motion of the electrons. The actual observed spectrum was around 200 times narrower than what was predicted by Gordon. This narrowing of the spectrum is due to the influence of the ions on the motion of the electrons. The extent of the ions influence on the electrons is defined by the Debye length:

$$\lambda_D = \left(\frac{\epsilon_0 k T_e}{N e^2}\right)^{\frac{1}{2}} \approx 69 \left(\frac{T_e}{N}\right)^{\frac{1}{2}} m \tag{2.4}$$

Where ϵ_0 is the permittivity of free space, k is the Boltzmann constant, T_e is the electron temperature and N is the electron density and e is the electron charge. Each ion influences electrons within a length of λ_D. λ_D varies with altitude ranging from a few millimeters in the F region, to around 1 cm in the D region. Organized motion in a plasma is impossible on a scale below λ_D, so observations

using wavelengths shorter than λ_D will result in a Gaussian spectrum as predicted by *Gordon* (1958). At lengths greater than λ_D the scattering is no longer from free electrons but due to density fluctuations by oscillations in the plasma (*Evans* (1968)). These fluctuations are induced by waves in the plasma, ion-acoustic waves and electron-acoustic waves. Ion-acoustic waves are induced by the presence of ions in the plasma and the electron-acoustic waves at the plasma frequency and electron gyrofrequency.

Incoherent radars are designed to primarily observe the spectrum from ion acoustic waves (ion line). Scattering is observed from ion-acoustic waves that have half the wavelength of the transmitted wavelength and are traveling vertically towards or away from the transmitter. Landau damping; the process of energy transfer between a wave and particle traveling at nearly the same speed broadens the ion line resulting in a doubled peak spectrum as shown in figure 2.4. This doubled peak spectrum is observed in the F region of the ionosphere and is related to the ratio of the electron and ion temperature (T_e/T_i). However below 100km in the ionosphere (D and E region) the collision frequency becomes too great for ion-acoustic waves to propagate in this region, resulting in a singularly peaked spectrum. A spectrum is also observed due to the electron-acoustic waves (plasma line). This produces a positive and negative frequency shift that is almost the plasma frequency. These lines are unbroadened as the electron-acoustic wave velocity is far greater than the thermal electron velocity.

Due to the complicated nature of the returned spectrum, many parameters can be determined. The parameters that can be directly observed are: electron density (N), electron temperature (T_e), ion temperature (T_i), Plasma drift velocity (V), ion composition (or mean ion mass), electric field-aligned current density (j) and ion neutral collision frequency (ν). The indirectly derived parameters are: neutral air density, ρ, neutral air wind velocity (U), Pedersen and Hall conductivities (Σ_ρ, Σ_H), energy spectrum of precipitating particles, heat flux (ψ), and photoelectron flux (ϕ). Not all of the directly observed parameters can be determined at

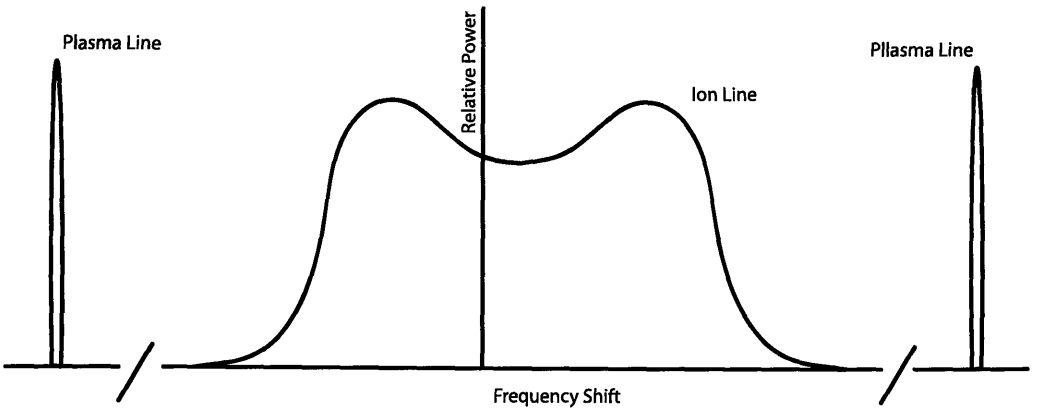

Figure 2.4: A typical observed incoherent radar spectrum (reproduced from *Hargreaves* (1992)).

all altitudes, and not all parameters can be measured accurately simultaneously (*Rishbeth and Williams* (1985)).

2.3.2 EISCAT

The **E**uropean **I**ncoherent **SCAT**ter radars in Northern Scandinavia began operating in 1981. The northern Scandinavian EISCAT has three sites, the main facility located near Tromsø has two monostatic radars, a UHF (935.5 MHz) and a VHF (224 MHz) radar. Complementing the UHF radar are two more UHF receivers at remote sites, one in Kiruna in Sweden and the other in Sodankylä. These make up a multistatic radar system that enables three independent components of ion velocity to be measured at any point in the ionosphere in the antennas line of sight (*Rishbeth and Williams* (1985)).

The UHF radar at Tromsø is a circularly polarized 32m parabolic dish that can be steered in both azimuth and zenith directions at a speed of 1.3° s^{-1}, with two klystrons giving a max power of 2MW. The VHF radar consists of four circularly polarized 30 × 40 m steerable parabolic cylinders. It is powered by one

klystron giving a max power of 1.6 MHZ and can be steered in the zenith direction. (*Rishbeth and Williams* (1985)).

In 1992 a UHF, 32m fully steerable parabolic EISCAT radar dish was built in Svalbard and has been operational since 1994. In 1999 a second 42m fixed dish radar was installed at the same location, fixed along the local magnetic field line.

EISCAT data is used in chapter 3 from the VHF antenna at Tromsø , observing the ionosphere between 60-300km.

2.4 Magnetometers

Measurements of magnetic variations on the ground and in space provide information on the solar wind and the Earth's magnetics field. The fields are the superposition of magnetic fields and current systems (*Kivelson and Russell* (1995)). The earliest magnetometer was devised by C.F gauss, consisting solely of a magnet suspended by a gold fiber. Today magnetometers can measure the vector components of the magnetic field. High latitude magnetometer chains have been used to amongst other things to; study current systems in the ionosphere (e.g. *Araki et al.* (1989), *Kavanagh et al.* (2009)), examine and monitor substorm activity (e.g. *Tanskanen* (2009); *Nose et al.* (1998)) and to detect geomagnetic pulsations (e.g. *Chernouss et al.* (1985)). This thesis contains data from three magnetometer chains.

2.4.1 IMAGE

The International Monitor for Auroral Geomagnetic Effects (IMAGE) magnetometer network is an international collaboration of 31 fluxgate magnetometers. Built as a replacement to the EISCAT cross , the 31 magnetometers located across most of Scandinavia measure the X, Y and Z components of the magnetic field

with a resolution of 1nT averaged over 10 seconds. Figure 2.6 shows the locations of all the currently operational magnetometers in the IMAGE network (red circles).

2.4.2 CARISMA

The Canadian Array for Realtime Investigations of Magnetic Activity is a network of fluxgate magnetometers that cover a range of longitudes between 220.96° E and 267.89° E and 69.54° N to 45.87 ° N. Most of the magnetometers are located on a North South meridian known as the 'Churchill Line'. This arrangement allows investigations into the radial propagation of events.

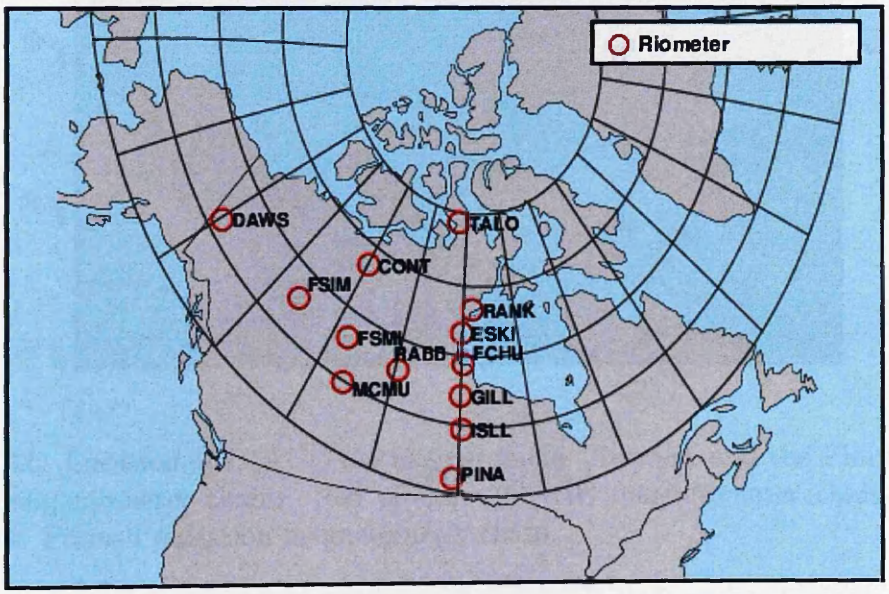

Figure 2.5: Location of CARISMA magnetometer chain.

2.4.3 Finnish Pulsation Magnetometer Chain

The Finnish pulsation magnetometer chain operated by the Sodankyla Geophysical Observatory are a chain of 6 magnetometers. These magnetometers are search

coil magnetometers, compared to the IMAGE fluxgate magnetometers. The search coil magnetometers sample data at 40Hz, giving 144000 data points per hour. This greater sampling rate allows for measurement of geomagnetic pulsations; ULF waves in the frequency range 1mHz - 1Hz which can contribute to particle precipitation into the atmosphere (*Coroniti and Kennel* (1970)). Figure 2.6 shows the locations of the 6 pulsation magnetometers (blue triangles).

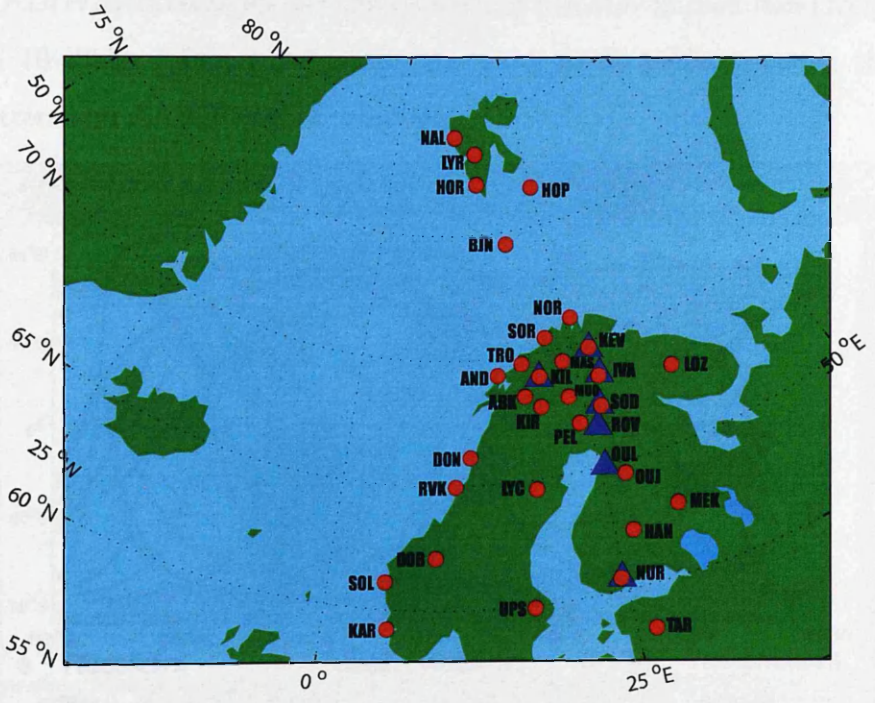

Figure 2.6: Location of IMAGE the magnetometer Network and the Finnish pulsation magnetometer chain. Red circles: IMAGE magnetometer chain. Blue triangles: Finnish pulsation magnetometer chain.

2.5 AARDDVARK

The **A**ntarctic-**A**rctic **R**adiation-belt (**D**ynamic) **D**eposition-VLF **A**tmospheric **R**esearch **K**onsortium network (AARDDVARK) is a series of ground based radio receivers, designed to continuously monitor and observe the lower ionosphere at mid to high latitudes (*Clilverd et al.* (2009)). Man made VLF transmission are

effectively 'trapped' between the ground and the ionosphere, essentially creating a wave guide between the Earth and the ionosphere. The AARDDVARK network simultaneously monitors these VLF transmissions, (usually military transmissions due to the expensive nature of running a continuous VLF transmitter) and records the phase and amplitude of the signal. Each AARDDVARK station consists of two orthogonally orientated loop antennas, a preamplifier and a VLF receiver. The AARDDVARK receivers can simultaneously measure narrow band frequencies between 10-40kHz. Figure 2.7 shows the great circle paths between the VLF transmitters and AARDDVARK receivers.

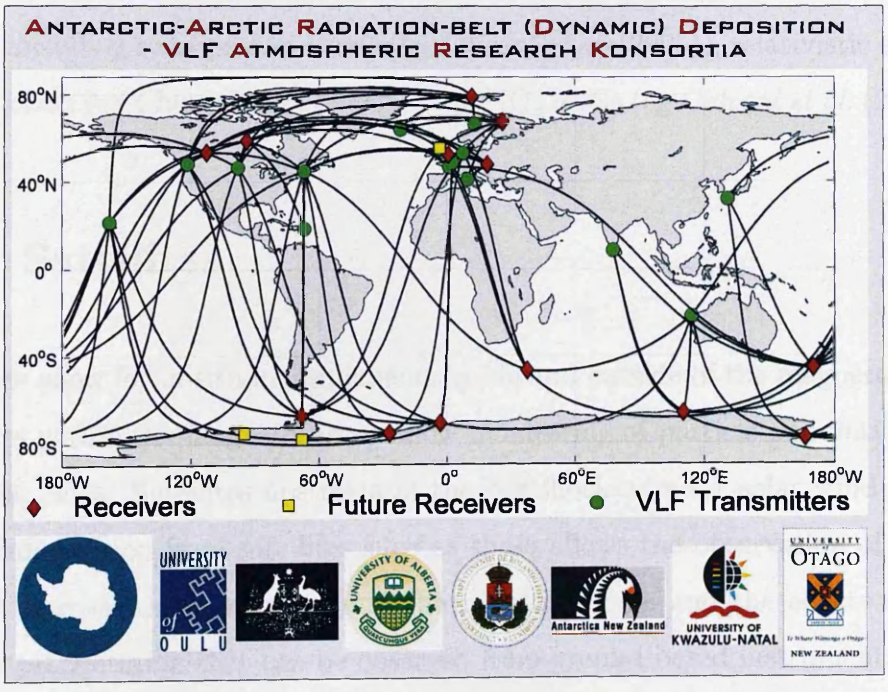

Figure 2.7: Great circle paths between monitored VLF communications transmitters (green) and AARDDVARK receiver locations (green). Image from *Clilverd et al.* (2009).

The lower part of the ionosphere (between 50-80km) makes up the upper part of the waveguide. On a geomagnetically quiet day, the amplitude and phase of VLF wave will alter in a fixed way during the course of a day, this allows a quiet day curve to be deduced. If there are alterations to the ionospheric chemistry, usually

caused by precipitating electrons and protons, this will cause a resulting change in the VLF amplitude and phase. Modeling of the VLF paths using programs such as the **L**ong **W**ave **P**ropagation **C**ode (LWPC) (*Ferguson* (1998)) which uses ionospheric and ground parameters to simulate the conditions to create a VLF transmission with a certain amplitude and phase can be used to model the ionospheric conditions at a certain time. However it is impossible to tell which part of the paths are affected by the precipitating particles without the use of crossed field paths or other instruments.

The AARDDVARK network can be used to investigate various solar terrestrial events, including solar proton events (eg *Clilverd et al.* (2005)), relativistic electron precipitation (eg *Clilverd et al.* (2006a)) and NO_x levels (eg *Clilverd et al.* (2006b)).

2.6 Satellites

Satellites allow for in-situ measurements inside and outside of the magnetosphere. Satellites within the magnetosphere allow monitoring of particle populations and magnetic fields. Satellites upstream of the bowshock monitor solar wind parameters. Information from satellites such as these allows the observation of the interplay between the solar wind and the magnetosphere and the effects such as particle precipitation that can be observed from ground based instruments. Data from two satellites have been used in this thesis, from geostationary orbit (LANL) and the solar wind monitor (ACE).

2.6.1 LANL

The **L**os **A**lamos **N**ational **L**aboratory (LANL) operate several satellites at geostationary orbit. Geostationary orbit places the satellites at 6.6Re and within the outer radiation belt. The first satellite was launched in 1987 and there have

been numerous others launched over the years, with an average of 3-5 satellites in orbit at any one time. The five current satellites (1990-095, 1994-084, LANL-97A, LANL-02A, and LANL-01A) carry the **S**ynchronous **O**rbit **P**article **A**nalyzer (SOPA) instrument (*Belian et al.* (1992)) and the **M**agnetospheric **P**lasma **A**nalyzer (MPA) instrument (*Bame et al.* (1993)). The SOPA instrument measures the electron fluxes across 10 differential channels between 50keV and 2MeV and proton fluxes across 8 differential channels between 50keV-8MeV. The MPA instrument allows measurement of 3D energy per charge distributions between 1eV-40keV, with derived parameters such as density, temperature, flow velocity.

2.6.2 ACE

The **A**dvanced **C**omposition **E**xplorer, (ACE) was launched in 1997 with a prime objective to determine and compare the elemental and isotopic composition of the solar corona, the interplanetary medium, the local interstellar medium, and galactic matter (*Stone et al.* (1998)). Located at the first Lagrangian point (L1) ACE has 9 on board instruments to measure the interplanetary particles and magnetic fields. These are the **C**osmic **R**ay **I**sotope **S**pectrometer (CRIS), **S**olar **I**sotope **S**pectrometer (SIS), **U**ltra **L**ow **E**nergy **I**sotope **S**pectrometer (ULEIS), **S**olar **E**nergetic **P**article **I**onic **C**harge **A**nalyzer (SEPICA), **E**lectron, **P**roton and **A**lpha **M**onitor (EPAM), **S**olar **W**ind **I**on **M**ass **S**pectrometer (SWIMS), **S**olar **W**ind **I**on **C**omposition **S**pectrometer (SWICS), **S**olar **W**ind **E**lectron **P**roton and **A**lpha **M**onitor (SWEPAM) and **Mag**netometer (MAG). These instruments allow measurement of solar wind parameters such as solar wind velocity, solar wind density and the IMF.

2.7 Indices

Magnetic indices allow for a simple measure of magnetic activity over a period of time (*Gubbins and Herro-Bervera* (2007)). Using measurements from magnetometers several indices have been created, either to quantify a physical processes in the ionosphere and magnetosphere, or to give a general description of magnetic activity at any given time.

2.7.1 K, K_p & A_p

The K-index was introduced by *Bartels et al.* (1939) as a 3-hourly measure of local storm-time magnetic activity. The calculation of the K-index is as follows, firstly for each 3 hour period the diurnal variations are removed from the **H** component magnetic field measurements. The range of the remaining data is measured and converted into a unitless quasi-logarithmic scale. For each station the K index is scaled in such a way as to normalize the occurrence frequency of K values across the globe.

The K_p index is a planetary measure of magnetic activity (*Menvielle and Berthelier* (1991)). The K_p index is an average of around 13 observatories' K-index, averaged to take into account local variations in the K measurement. As with the K index the K_p index is a semi-logarithmic scale with values: 0, 0.3, 0.7, 1,...9.

The A_p index is very similar to the K_p index, but is converted into a linear scale instead of a quasi-logarithmic scale. Table 2.1 shows the relationship between the K_p and A_p indexes (*Hargreaves* (1992)).

K_p	0	1	2	3	4	5	6	7	8	9
A_p	0	3	7	15	27	48	80	140	240	400

Table 2.1: Relationship between K_p and A_p indexes.

2.7.2 DST

The **D**isturbed **S**torm **T**ime index (Dst) was designed to measure the enhancement of the westward equatorial ring current. The DST index is an hourly index and is calculated using data from the **H** component of the magnetic field from 4 observatories located around the globe close to the equator. The data has the diurnal variations removed and is normalized to the magnetic equator. The average of this data is the DST index and is measured in nT. Storm time conditions are represented by negative deflections in the DST index. Although originally thought to be measuring only the westward ring current evidence indicates that the ring current may only make up a small part (*Wanliss and Showalter* (2006)) and the measurement is made up by the superposition of numerous current systems. However, it still is a good statistical descriptor of storm time activity and is a widely used index.

2.7.3 SYM-H

The SYM-H index is another index created to measure the storm time ring current. It is calculated in an almost identical manner to the DST index, except that 6 stations are used and is calculated to a 1 minute resolution instead of the DST's 1 hour resolution. Like the D_{st} index the SYM-H index is also measured in nT. *Campbell* (2004) examine the differences between the two index, showing that the SYM-H is comparable to the DST index and can be used as a high resolution alternative.

2.7.4 AE

The AE index was developed by *Davis and Sugiura* (1966) as a measure of global auroral electrojet activity. Observatories from the auroral regions are used in the calculation of the AE index. 1 minute resolution data of the horizontal **H** component of the magnetic field is used. For each observatory the average of the 5 quietest days is subtracted from the data. The total range from the observatories is calculated, The AU index is defined as the greatest value and the AL index as the smallest value. The AE index is then calculated by simply subtracting the AU index from the AL index. The AE index is measured in nT.

2.8 Summary

Riometers play a pivotal role within this thesis, being utilized in chapter 3 to estimate the height of cosmic noise absorption and subsequently the energies of the precipitating electrons, as well as being one of the primary instruments used in the statistical study of daytime absorption in chapter 4. As such the background theory and principles of operation are discussed in great detail in this chapter. The two riometers used for these studies are also presented. In addition to the riometers, a number of ground based instruments and satellites are utilized within this thesis and are all described within the chapter. These include the incoherent scatter radar EISCAT, the IMAGE and CARISMA magnetometer chains, the AARDDVARK VLF receivers, the LANL geostationary satellites and the ACE satellite.

Magnetic indices are used throughout this thesis as they allow for a simple measure of the geomagnetic activity, and as such provide a useful tool for putting events into context. The magnetic indices used are described in this chapter and they are the K, DST, SYM-H and AE indices.

Chapter 3

Height Estimation of Cosmic Noise Absorption

Firstly this chapter describes the development of two methods of calculating the height of peak CNA from riometers with overlapping fields of view and the comparison of these methods with the previously published vertical parallax technique of *Terkildsen et al.* (2004). Secondly a method for estimating the characteristic energy of precipitating electrons form the peak height of CNA is investigated and then applied to the height estimates of peak CNA absorption for three case studies.

3.1 Introduction

The precipitation of electrons into the atmosphere is an important step in the transfer of energy and momentum through the coupled solar-terrestrial environment. Electrons with energies from 10s to 100s of keV penetrate to mesospheric heights (60-100 km) enhancing the ionized D-layer of the atmosphere and affecting the resultant ion chemistry (*Rees* (1989)). These electrons are injected from the magnetotail during substorms (*Arnoldy and Chan* (1969)) and undergo gradient-

curvature drift into the dayside ionosphere; along the drift path they interact with whistler-mode chorus waves which scatter a fraction of the electron population into the bounce loss cone, resulting in a diurnal variation of precipitation maximising in the morning sector (e.g. *Kavanagh et al.* (2004b)). Direct measurement of this scattering process and loss cone electrons are difficult to obtain on a regular basis; however ground-based instruments can provide a proxy for the occurrence of electron precipitation. By monitoring the absorption of cosmic radio noise along a fixed beam path, riometers (*Little and Leinbach* (1959)) provide an indication of the increased electron density in the D-layer and consequently the associated electron precipitation. The continuous monitoring by riometers is a valuable resource but its utility is vastly enhanced when used in conjunction with other instruments (e.g. *Kavanagh et al.* (2007); *Collis and Hargreaves* (1997)). The major disadvantage of riometer estimates of precipitation is the lack of information on the altitude distribution of the cosmic noise absorption (CNA); knowing the height of peak CNA can lead to an estimate of the characteristic energy of the precipitating electrons. *Terkildsen et al.* (2004) provided a means of height estimation through the use of a vertical parallax technique; this method, though successful, is limited as it requires the CNA event to have a east-west motion and it assumes a constant altitude over the course of the event.

In this chapter we use two closely located riometers with overlapping fields of view to determine a new method of estimating the height of peak CNA. We apply tomographic reconstruction to the absorption problem and also develop a method using height triangulation. These methods are evaluated using test data and compared with the method of *Terkildsen et al.* (2004). A case where incoherent scatter radar data were available is shown; this provides an independent check on the two techniques.

Stauning (1996) describes various absorption processes which can be observed by a riometer. The location of the riometer dictates which type of absorption phenomena are seen. IRIS at Kilpisjärvi and ARIES are located at auroral al-

titudes. We apply the techniques to three separate case studies employing data from October - December 2007; these events show differing characteristics and are categorized by *Stauning* (1996) as a) a slowly varying absorption event, b) a substorm, and c) an afternoon absorption spike. The characteristic energy of the precipitating electrons based on the height estimate is calculated for each event.

3.2 Instrumentation

Observations of the CNA events have been provided by the Advanced Rio-Imaging Experiment in Scandinavia (ARIES) and the Imaging Riometer for Ionospheric Studies (IRIS) at Kilpisjärvi. These two riometers have been chosen because of their overlapping fields of view. Figure 3.1 shows the overlapping fields of view, at 90km. There is significant overlap between 18.5°-23° longitude and 68.4°-70° latitude.

Measurements obtained from the co-located incoherent scatter radar, EISCAT (*Rishbeth and van Eyken* (1993)) marked as a star in figure 3.1 are also utilized as a validity check on the techniques for height determination.

3.3 Methods

3.3.1 Height Triangulation

Using the recorded absorption in the beams of the two riometers, a spatial image of the absorption can be produced for both ARIES and IRIS. The pointing direction of each beam is used to calculate the location at heights between 70 and 150km. At each height the values of absorption are interpolated onto a 2 dimensional grid. Linear interpolation is used to populate the gaps between the beam centers

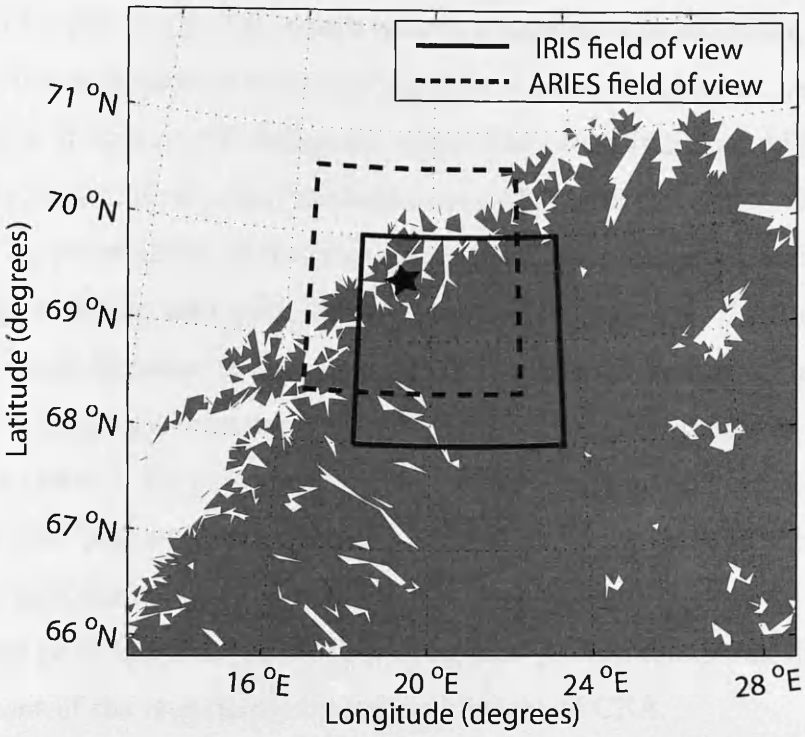

Figure 3.1: Plot showing the overlapping fields of view of ARIES and IRIS at 90km altitude. Star: Location of EISCAT mainland radar.

and create the absorption image. This is achieved using the Multi Instrument Analysis Toolkit (MIA) (*Marple and Honary* (2004)). An assumption is made that the recorded power is located at the beam center. In the case of IRIS the corner beams have ill defined main lobes and significant sidelobes and thus not used in the creation of the images, and with ARIES the central 556 beams are used.

Setting a spatial grid on which the absorption values of both riometers are calculated, direct comparison of the two images can be made. A spatial grid between 66.5-71.5° N (with 0.05° increments) and 13.5-26.5° E (with 0.10° increments) is used. By projecting the images to heights between 70 and 150km, with a 2km increment, the linear cross correlation of the two images at each height can be calculated. The height of best correlation corresponds to the best estimate of the

peak height of CNA. Only results that have a correlation greater than 0.6 will be considered for this study. This cutoff value is a heuristic choice, giving a trade off between number of resolved events and confidence value of the result. A resolution of 10 seconds is used for the absorption values taken from IRIS and ARIES, unless otherwise stated. The standard deviation associated with the height estimation is generated by uncertainties in the cross correlation. These uncertainties encompass such things as height ambiguity, vertical extent of the peak etc. This is expressed as the standard deviation in the cross correlation for each altitude. The standard deviation in the height triangulation is obtained in the same manner as in (*Ashrafi and Kosch* (2004)). For each cross correlation value, a new cross correlation value is created that falls within the normal distribution of the original value. A second order polynomial curve is fitted to the new values. The curves maximum value is the peak height of CNA. Repeating this process numerous times allows measurement of the uncertainty on the peak height of CNA.

3.3.2 Tomography

The second method employed is to create a 3D reconstruction of the absorption using tomographic methods. Tomography is the process of recreating the internal structure of an object using intensity data from the integral along the line of sight through the object (*Gustavsson* (2000)). Recently tomographic methods have been applied to emission processes in the upper atmosphere. Data from measurements of total electron content (TEC) between satellites and ground receivers to create 2D maps of electron density in the ionosphere have been widely investigated (*Fougere* (1995); *Bhuyan et al.* (2002)). Related work reconstructing the optical emissions in the ionosphere using ground based cameras have been implemented in (*Gustavsson* (2000); *Semeter and Mendillo* (1997)). Tomography is implemented in this study to reconstruct the 3D structure of CNA in the D-region ionosphere

using 2D absorption images recorded by imaging riometers. Figure 3.2 illustrates the geometry of the problem.

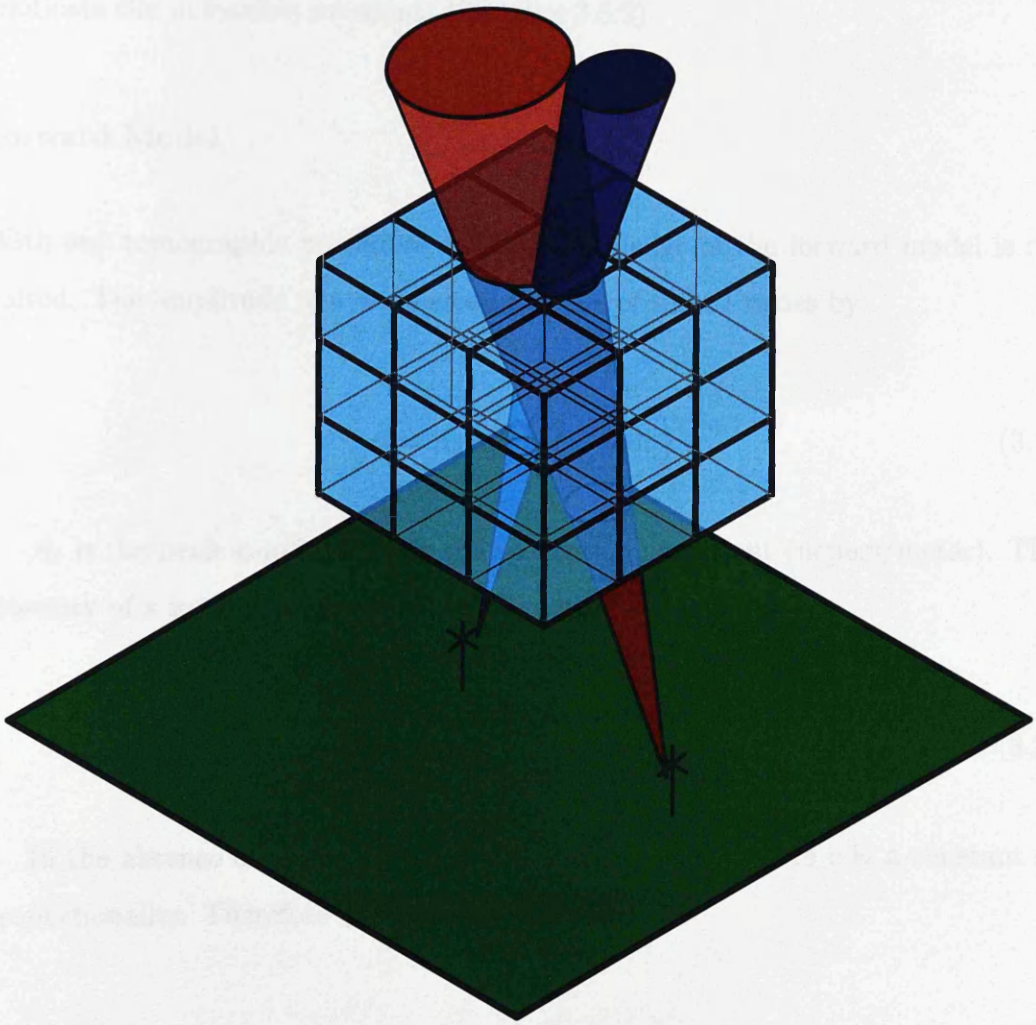

Figure 3.2: Tomographic problem for CNA. voxels are discretized between 69°-70.4° degree in latitude, 18.5°-22.7° degree in longitude and 55-120 km in altitude. They are spaced 0.2° 0.64° and 5km respectively. For this volume element 18 IRIS beams, (example beam shown in red) and 306 ARIES beams (example beam shown in purple) are used.

The absorption volume is discretized into small volume elements called 'voxels'. With a volume constructed with a relatively conservative number of voxels (7x7x13) the problem still has more degrees of freedom than is supported by the data (637 voxels compared to 324 beams). This leads to what is known as an 'ill

posed' problem. Ill-posed problems suffer from having numerous solutions, where only a portion are feasible solutions. Thus the problem needs to be regularized to eradicate the unfeasible solutions. (Sections 3.3.2)

Forward Model

With any tomographic procedure detailed knowledge of the forward model is required. The amplitude of a wave along the line of sight l varies by:

$$A = A_0 \exp\left(\int_0^l -\kappa \mathrm{d}l\right) \tag{3.1}$$

A_0 is the peak amplitude. κ is the absorption coefficient (nepers/meter). The intensity of a wave is proportional to the amplitude squared.

$$I \propto \left[A_0 \exp\left(\int_0^l -\kappa \mathrm{d}l)\right)\right]^2 \tag{3.2}$$

In the absence of of absorption $\kappa = 0$ and $I_0 = cA_0^2$. where c is a constant of proportionality. Therefore the intensity becomes,

$$I = I_0 \exp\left(\int_0^l -2\kappa \mathrm{d}l\right) \tag{3.3}$$

The cosmic noise absorption measured by a riometer is a measure of the noise power, P compared to the quiet noise power P_Q, the power if there was no absorption. Absorption measured by a riometer in decibels is Absorption=-$10\log_{10}(P/P_Q)$. The received RF power in a given direction is proportional to the square of the directivity (the gain) (*Detrick and Rosenberg* (1990)) multiplied by the sky noise intensity. Thus the total power received by the riometer is then the integral of the intensity of the wave in all solid angles (Ω), weighted by the gain.

$$P = c \int_{\Omega} G(\Omega) I_0(\Omega) \exp\left(\int_0^l -2\kappa(l,\Omega) \mathrm{d}l \mathrm{d}\Omega \right) \tag{3.4}$$

Where c is a constant of proportionality. Thus the absorption in a riometer becomes, noting power on a quiet day means $\kappa = 0$.

$$\text{Absorption} = -10\log_{10} \left[\frac{c \int_{\Omega} G(\Omega) I_0(\Omega) \exp\left(\int_0^l -2\kappa(l,\Omega) \right) \mathrm{d}l \mathrm{d}\Omega}{c \int_{\Omega} G(\Omega) I_0(\Omega) \mathrm{d}\Omega} \right] \tag{3.5}$$

Assuming I_0 doesn't vary greatly across the sky, and voxelizing the field of view of the riometer, equation 3.5 can be written as:

$$\text{Absorption} = -10\log_{10} \left[\frac{\sum_{i=0}^{I} G_i \Delta\Omega_i \exp(-2 \sum_{j=0}^{J} \kappa_j l_{ij})}{\sum_{i=0}^{I} G_i \Delta\Omega_i} \right] \tag{3.6}$$

The integral over solid angle, is numerically represented by a summation of solid angle $\Delta\Omega_i$ for a set of ray directions i, with gain G_i. The ray directions are evenly spaced over all directions from the riometer in steps of 2 degrees in zenith and azimuth, giving 8100 rays. κ_j represents the absorption coefficient in voxel j. l_{ij} is the intersect length of ray i with voxel j. Equation 3.6 clearly shows that this is not a linear problem, therefore linear tomographic methods used in many tomographic applications will not work and a non-linear method will have to be implemented.

Occam's inversion

Occam's inversion is a popular method for solving nonlinear inversion problems and was first introduced by *Constable et al.* (1987). The inversion is an iterative algorithm which searches for the smoothest fit to the model $H(\kappa)$, subject to an appropriate fit to the data. This can be represented as

$$min\{\|WH(\kappa) - Wd\|^2 - \alpha\|L(\kappa)\|^2\} \tag{3.7}$$

This is similar to Tikhonov regularization of linear inversion problems (*Aster et al.* (2005)). Alpha represents the regularization parameter, $\alpha > 0$. $H(\kappa)$ is the forward model, equation 3.6 described in section 3.3.2. d is the data vector (absorption values for IRIS and ARIES). W is the diagonal matrix of weighting factors of the data.

$$W = diag\{1/\sigma_1, 1/\sigma_2, ...1/\sigma_X\}. \tag{3.8}$$

These are the data variances of the beams, given by 0.05 for IRIS and 0.3 for ARIES. The difference in weighting factors stops the ARIES data dominating over the IRIS data. L is the roughening matrix which takes different forms for different orders of regularization. For zero order regularization L=I, where I is the identity matrix. L is implemented to be 3D finite difference solution of the laplacian for κ, given by:

$$\begin{aligned} \nabla^2\kappa(x,y,z) \;=\; & \frac{1}{h^2}[\kappa(x+h,y,z) + \kappa(x-h,y,z) + \kappa(x,y+h,z) \\ & +\kappa(x,y-h,z) + \kappa(x,y,z+h) \\ & +\kappa(x,y,z-h) - 6\kappa(x,y,z)] \end{aligned} \tag{3.9}$$

This constrains κ to be smooth in the x, y and z directions (longitude, latitude and altitude). Occam's inversion implements an iterative local lineralization (*Aster*

et al. (2005)). For a model guess κ^k, Taylor's theorem is applied to determine the local linearization.

$$H(\kappa^k + \Delta\kappa) \approx H(\kappa^k) + J(\kappa^k)\Delta(\kappa) \tag{3.10}$$

J(κ^k) is the Jacobian of the forward model H(κ^k). Substituting equation 3.10 into equation 3.7 gives:

$$min\{\|WH(\kappa^k)) + WJ(\kappa^k)\Delta\kappa - Wd\|^2 - \alpha\|L(\kappa^k + \Delta\kappa)\|^2\} \tag{3.11}$$

Reformulating the problem so that $m^{k+1} = m^k + \Delta m$, and letting

$$\hat{d}(\kappa^k) = d - H(\kappa^k) + J(\kappa^k)\kappa^k \tag{3.12}$$

gives

$$min\{\|WJ(\kappa^k)\kappa^{k+1} - W\hat{d}(\kappa^k)\| + \|L\kappa^{k+1}\|^2\} \tag{3.13}$$

The iterative step to solving equation 3.13, from linear theory is given by:

$$\kappa^{k+1} = [\{WJ(\kappa^k)\}^T WJ(\kappa^k) + \alpha^2 L^T L]^{-1}[WJ(m^k)]^T \hat{d}(\kappa^k) \tag{3.14}$$

A starting value of κ=0.001 for all voxels is used to start the iteration process. (k=1, where k is the iteration number). The iteration of κ is performed by use of equation 3.14.

The goodness of fit between the model and data is assessed using the χ^2 least squares criteria

$$\chi^2 = \sum(WH(\kappa) - Wd)^2 \tag{3.15}$$

Unlike many regularization regimes where α is constant and set before the optimization, Occam's inversion dynamically adjusts α at each iteration so that the χ^2 value of the solution does not exceed a threshold value (δ). If a value does not exist, the α that minimizes the solution most is chosen. It is assumed that the noise on the data is uncorrelated and due to a Gaussian process then δ is

the number of data points (*deGroot Hedlin and Constable* (1990)). The drawback to this method is that it allows negative values for κ, where in reality negative absorption does not occur. A full description of the Occam's inversion algorithm can be found in *Constable et al.* (1987) and *Aster et al.* (2005).

Although the inversion procedure used for this tomographic work was already established, all the code for the tomographic procedure, including the forward model, ray tracing algorithm, and inversion program was written from scratch for this work.

3.3.3 Vertical Parallax Technique

Terkildsen et al. (2004) developed the vertical parallax method to estimate the height of greatest CNA. The vertical parallax method calculates the time lag between observing a moving patch of absorption in a single beam of one imaging riometer, and the same event in an intersecting beam of the second riometer. The relationship between the time lag and height of the absorption event is:

$$T = \left(\frac{H - Z}{Z}\right)\frac{L}{V} \tag{3.16}$$

where V is apparent velocity of the absorption patch between the two instruments, H is event altitude, Z is altitude of the beam intersection and L is horizontal distance between the two riometers. Figure 3.3 shows a representation of the absorption measured in intersecting beams of the two riometers for three cases; A. when the moving absorption patch is below the intersection point. B. The absorption patch is at the intersection point and C. the absorption patch is above the intersection point. Plotting time lag against beam intersection altitude will allow calculation of the event altitude. Fitting a curve to the result, where the curve passes through 0 time lag is the event altitude. Only beam-pair cross corre-

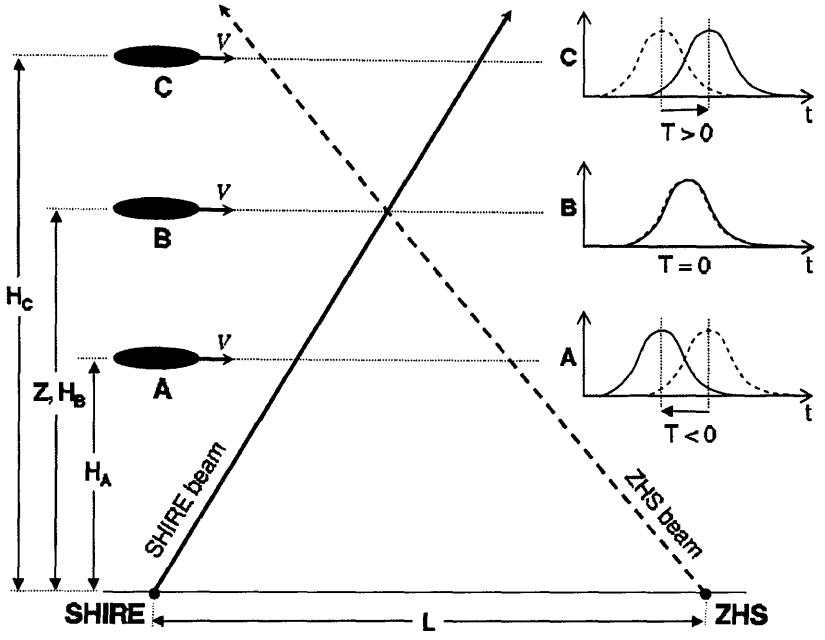

Figure 3.3: Schematic showing the relative response between individual beams of two overlapping riometers. The three cases are for an absorption event A. Passing below the intersection point of the two beams. B. Passing at the intersection point of the two beams and C. Passing above the intersection point of the two beams. The dotted and solid lines in A, B and C represent the absorption as seen in the two beams, and the lag or lack of, between the two responses. (After *Terkildsen et al.* (2004))

lations of 0.9 or greater are used in this study. For a full description of the vertical parallax method see *Terkildsen et al.* (2004).

The assumptions and requirements for the vertical parallax method to work are; firstly the absorption patch moves across the field of view of the two imaging riometers. Secondly over the segments of the event (a moving feature) the height of the absorption event doesn't change.

3.4 Test Data

Using the forward model described in section 3.3.2 it is possible to create data with which to test the height triangulation, vertical parallax and 3D reconstruction methods. Such data are referred to as phantoms in tomographic literature, such as *Fougere* (1995) and we follow this convention here. Figure 3.4 shows 3 test phantoms. Phantom A is a layer of absorption at 100km with a vertical extent of 8km. Phantom B is an 'arc' along 69.3° latitude, at 85km, with a Gaussian profile in the vertical and longitudinal direction of 8km and 0.1° respectively. Phantom C is a patch of absorption at 90km altitude; location 69.5° N, 19.5° E with a vertical extent of 8km, a longitudinal extent of 0.1° and latitudinal extent of 0.9°. Each phantom has a peak of 0.001dB/m. The reconstructed phantoms are seen on the right of figure 3.4, D: reconstructed layer, E: reconstructed arc and F: reconstructed patch. A more quantitative representation is shown in Figure 3.5, where a vertical profile of the phantoms taken through the center of each absorption patch are compared with the reconstructed profile. The solid lines represent the phantom (red: arc. green: patch. black: layer) and the dotted lines the reconstruction.

Figure 3.6, shows the results of the height triangulation on the phantoms. The red crosses represent the cross correlation of the arc phantom at each projected height, the green stars the patch phantom. The height triangulation is able to triangulate the height for both phantom B and C, correctly having a maximum in cross correlation at 85km for the arc phantom and 100km for the patch phantom. The height triangulation relies on there being spatial features for the process to work, so it is unsurprising that it unable to determine the height of maximum CNA for phantom A, as phantom A is a diffuse layer, and as such does not have any spatial features.

Modifying the arc and patch phantoms to move in time across the field of view of the riometers the vertical parallax method can also be tested. The two phantoms are modified to move across 1° in latitude at a speed of 0.01° s^{-1} over

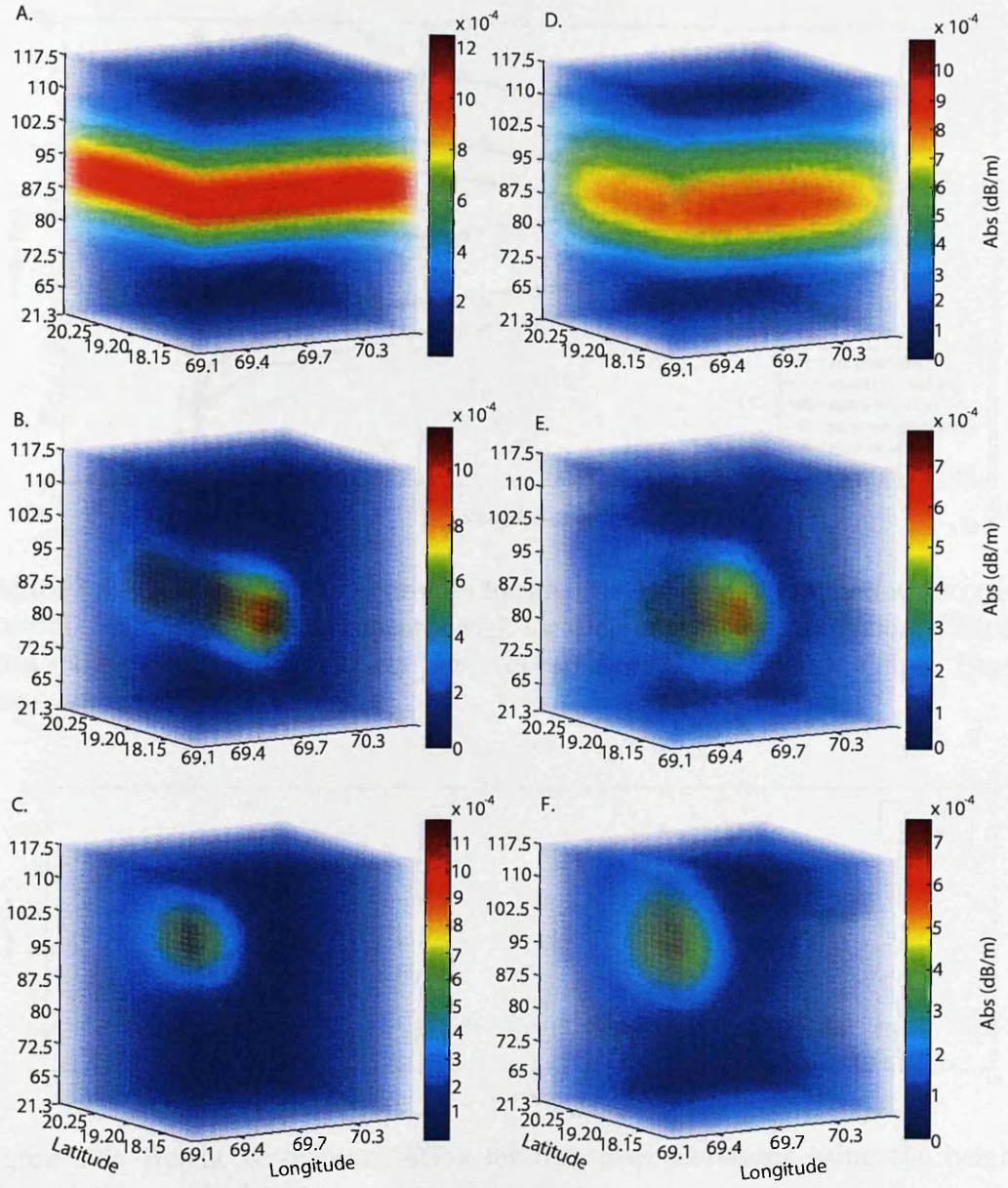

Figure 3.4: Left: Phantom data created to test inversion. A 'Layer' at 90km. B. 'Arc' at 85km, along 69.3° (0.1° width) latitude. C. Absorption patch with Gaussian form in longitude, latitude and height at 100km. (69.5° N, 19.5° E. With widths of 0.1° and 0.9° respectively.) All phantoms have a max CNA of 0.001 dB/m and vertical extent of 8km. Right: Reconstructed images of the 3 phantoms using Occam's inversion. D Layer. E. Gaussian arc. F. Gaussian patch.

the field of view of the riometers. Plot A of figure 3.7 shows the lag-height result for the arc phantom, while figure B shows the result for the patch. The plot shows

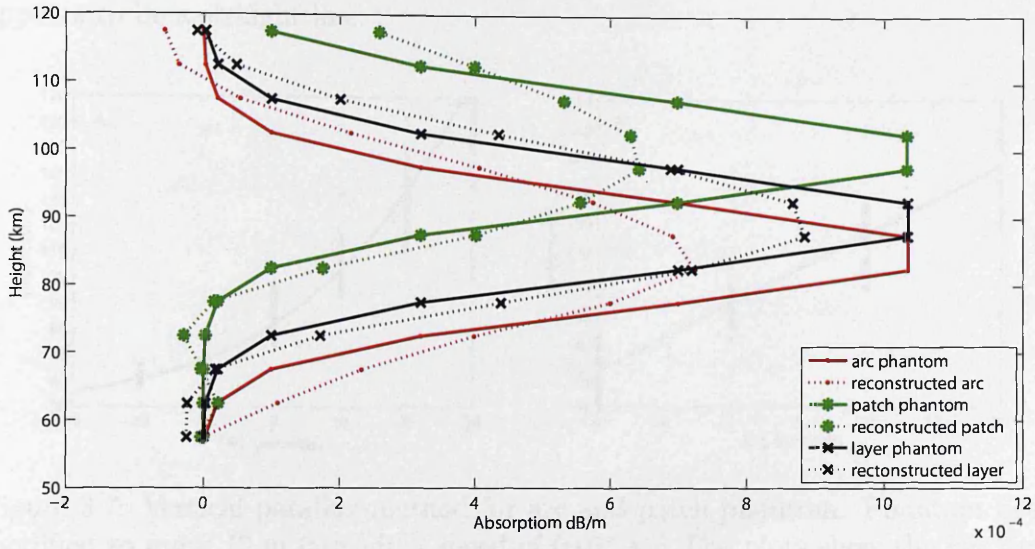

Figure 3.5: Vertical absorption profiles for phantom and reconstructed absorption objects. Solid lines are phantoms through location of greatest absorption. Dotted lines show reconstructed artifacts. Red (dots): Arc. Green (stars): Patch. Black (crosses): Layer.

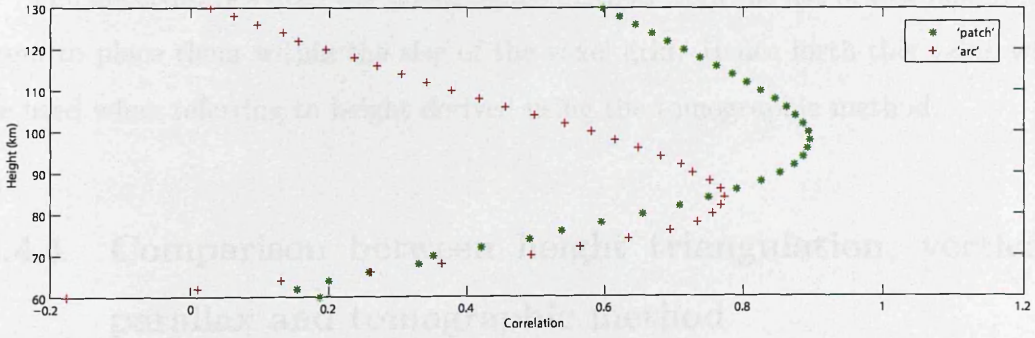

Figure 3.6: Height versus correlation for the three phantoms using the height triangulation method.

the lag time of absorption observed by intersecting beams of ARIES and IRIS as a function of their intersection height. A second order curve is fitted to the results, for the arc patch in plot A the curve passes through zero lag at 85 km. For the patch phantom in Panel B the curve crosses zero lag at 100km, thus correctly identifying the height of maximum CNA. The best fit to the data seems to be a second degree polynomial curve, however panel b is not near the turning point so

appears to be a straight line.

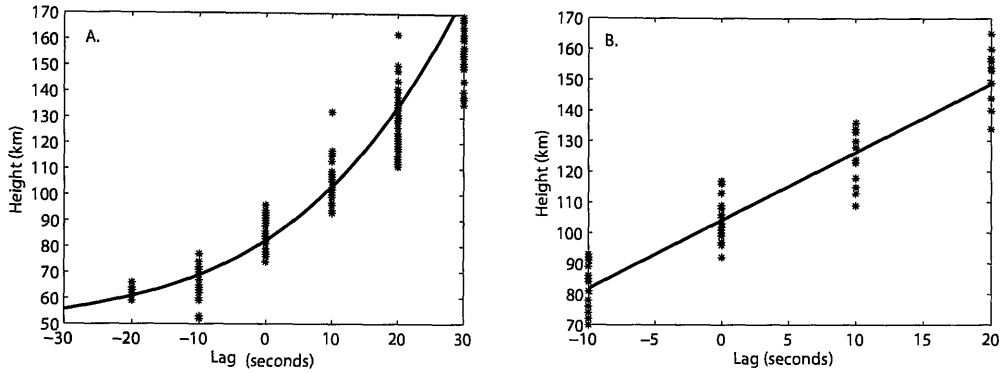

Figure 3.7: Vertical parallax method for arc and patch phantom. Phantom been modified to move 1° in latitude a speed of 0.01° s^{-1} The plots show the lag time of observed absorption between intersecting ARIES and IRIS beams versus the intersection height of the beams. A. Time lag versus height for arc at 80km. B. Time lag versus height for patch at 100km.

The uncertainties from the tomographic method from the use of test phantoms seem to place them within the size of the voxel grid. Hence forth this value will be used when referring to height derived using the tomographic method.

3.4.1 Comparison between height triangulation, vertical parallax and tomographic method

Table 3.1: Results from the three height estimation routines for the three test phantoms. Ticks represent successful estimation of the height of peak CNA. Crosses represent failure to estimate the height of peak CNA.

Height Method	Patch	Arc	Layer
Tomographic	√	√	√
Height Triangulation	√	√	×
Vertical Parallax	√	√	×

Table 3.1 shows the results of the three height routines on the three test phantoms. The best results are from the tomographic reconstruction which estimates

the height of maximum CNA for all three test phantoms. Due to the limited viewing angle of the two riometers the regularization required means the reconstruction underestimates and smooths the absolute values. Both the height triangulation and vertical parallax method reconstruct the height of peak CNA for two out of three of the phantoms. However looking at the assumptions and requirements for each method, the new height triangulation method has advantages over the vertical parallax method. Firstly the vertical parallax method can only measure one value for the height of max CNA over a segment of the event (a moving feature), with events lasting from minutes to tens of minutes; whereas the height triangulation method can measure the rapidly changing absorption structure of the order of tens of seconds (this resolution allows for noise in the data to be averaged out). Secondly the vertical parallax method has the requirement of a moving absorption patch; an assumption not required for the height triangulation method. The height triangulation method can calculate the height estimates for an absorption event relatively quickly (30 seconds - 1 minute) compared to the tomographic method (3-5 minutes). However the height triangulation assumes the absorption event occurs at a constant height across the field of view, an assumption that the tomographic method does not require.

The tomographic reconstruction and height triangulation offer improvements over the vertical parallax method, with the tomographic reconstruction offering the greatest versatility. Due to the fact that the height triangulation and tomography offer a superior diagnostic tool, not relying on absorption events moving during the course of the event and being able to calculate more than one value for an event, these will be the methods applied during the comparison with EISCAT and the case studies.

3.4.2 Reliability of Tomographic Method

Through analysis of the tomographic reconstruction, it is clear that the method is unable to accurately measure the absolute values of the differential absorption, but does show the correct shape of the absorption events. This can be seen in figure 3.5 where the absolute values of the absorption events is being smoothed out, but with the shape of the absorption event being maintained. To better understand the limitations of the tomographic method, numerous runs using phantom data has been carried out, comparing the reconstruction with the phantom using the cross correlation coefficient. This was chosen as it represents the linear dependence between the reconstruction and the phantom data. As long as the reconstruction retains the shape of the original phantom then the correlation will be high and thus we can have confidence in the estimation of the height of maximum CNA. To understand how the reliability alters across the field of view, multiple parameters of the layer, arc and patch phantom are varied and the cross correlation calculated. All runs used a max values of CNA of 0.001 dB. Each variation uses a Gaussian structure to represent vertical shape, and horizontal shapes for the patch and arc. When referring to the extent, this refers to the Gaussian parameter that determines the width of the Gaussian shape.

Figure 3.8 shows the cross correlation for the layer phantom when varying the height of the absorption event and the vertical extent of the Gaussian profile. Panel A, shows the cross correlation between the original layer phantom and the reconstruction for different altitudes. The altitude of the layer ranges from 55km to 110km, incrementing in 2.5km steps. The vertical extent was set to 8km for these phantoms. The cross correlation is above 0.6 for all altitudes, indicating that the reconstruction of the layer is accurate across the field view of the reconstruction area. The greatest correlation is between 60 and 75km, with values ranging from 0.84 to 0.92. The correlation drops to its lowest value of 0.62 at 87.5km and then rises again to 0.81 at 100km. The correlation would be expected to be the greatest

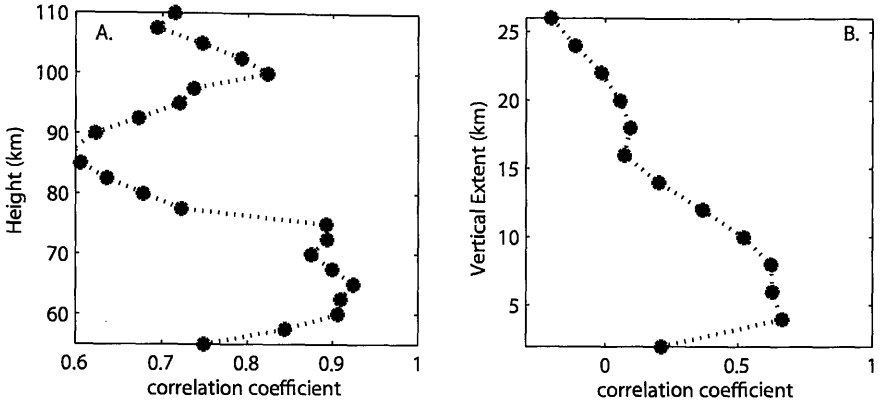

Figure 3.8: Cross correlation between Layer phantom and tomographic reconstruction. Panel A: Cross correlation between the Gaussian layer phantom and the 3D reconstruction for varying altitudes. (Vertical extent: 8km) Panel B: Cross correlation between the Gaussian layer phantom and the 3D reconstruction for varying vertical extents (Height of layer: 90km)

the lower in altitude the absorption event occurs, as the angle between the two instruments is greater. The minimum at 87.5km might indicate a decrease in coverage of beams at this altitude, however the correlation is sufficient enough to have confidence for estimations of the height of maximum CNA. Panel B of figure 3.8 shows how the cross correlation varies as the vertical extent of the Gaussian profile is altered. The phantom was set at 90km with a max CNA of 0.01dB. The vertical extent of the Gaussian profile was increased from 2km to 26km in 2km increments. The greatest correlation occurs between 4km and 10km, with the correlation steadily decreasing between 10km and 25km. The low correlation for a vertical extent of 2km indicates that reconstructions would be unreliable for these events.

Figure 3.9 shows how the cross correlation value varies for the arc phantom. Panel A shows how the height of Maximum CNA for an arc affects the cross correlation (Other parameters: Vertical Extent: 8km. Latitudinal Extent 0.2°. Latitudinal Position: 69.4°). Much like the results for the layer, the cross correlation is high for all values, starting at 0.75 at 55km, rising to a maximum at 100km

of 0.94. Like the layer there is a local minimum at 85 km 0f 0.86. However this is still a very high cross correlation.

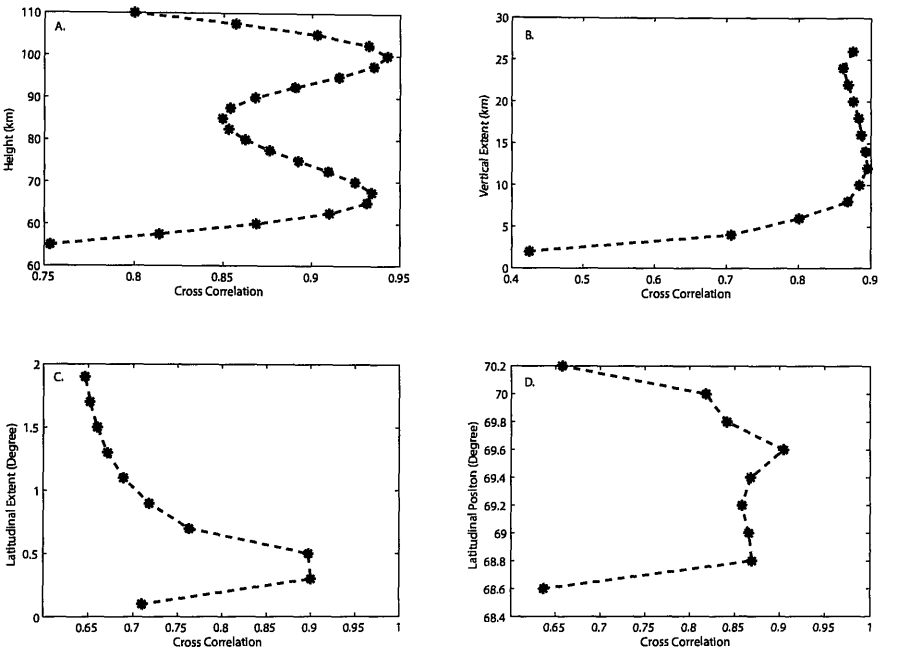

Figure 3.9: Cross correlation between Gaussian arc phantom and tomographic reconstruction. Panel A: Cross correlation between the phantom and reconstructed model for varying height of maximum CNA (Vertical Extent: 8km. Latitudinal Extent 0.2°. Latitudinal Position: 69.4°.) Panel B: Cross correlation between the phantom and reconstructed model for varying vertical extent (Height of Max CNA: 90km. Latitudinal Extent 0.2°. Latitudinal Position: 69.4°). Panel C: Cross correlation between the phantom and reconstructed model for varying latitudinal extent (Height of Max CNA: 90km. Vertical Extent: 8km Latitudinal Position: 69.4°.) Panel D: Cross correlation between the phantom and reconstructed model for varying latitudinal position (Height of Max CNA: 90km. Vertical Extent: 8km. Latitudinal Extent: 0.4°.)

Panel B shows how the vertical extent affects the cross correlation. (Other parameters: Height of Max CNA: 90km. Latitudinal Extent 0.2°. Latitudinal Position: 69.4°.) Below 5km the cross correlation is low, dropping to 0.43 as the vertical extent decreases, above 5km the cross correlation stays high, above 0.8. This indicates that for arc like structures the vertical extent is required to be greater than 3km for a reliable result. The variation of the latitudinal extent is displayed in Panel C, (Other Parameters: Height of Max CNA: 90km. Vertical

Extent: 8km Latitudinal Position: 69.4°). There is a maximum correlation between 0.3° and 0.5°, with a high of 0.9. As the arc approaches a more layer like shape (as the latitudinal extent increases), the correlation steadily decreases to 0.65. This panel indicates that for arc like structures there will be a high correlation, as long as there is a reasonable vertical extent. Finally Panel D shows how the cross correlation varies depending on the latitude of the arc (other parameters: Height of Max CNA: 90km. Vertical Extent: 8km. Latitudinal Extent: 0.4°.) The correlation is consistently high with values over 0.85 for all but the values on the edge of the reconstruction area. At the edges, 68.6° and 70.2° the cross correlation drops to 0.64 and 0.66 respectively. The results from figure 3.9 indicate that for arc like structures, as long as there is some latitudinal extent and a vertical extent greater than 4km the reconstruction will reproduce the shape of the absorption patch to a reliable degree.

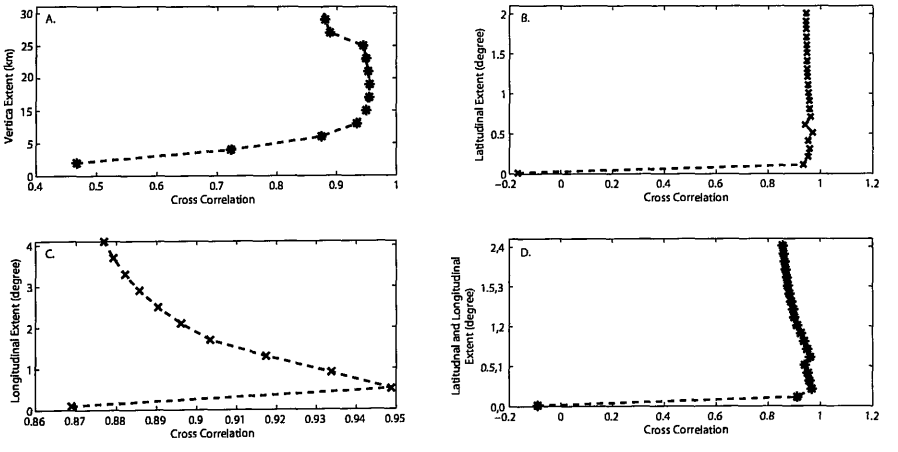

Figure 3.10: Cross correlation between Gaussian patch phantom and tomographic reconstruction. Each patch is at 100km, 69.5° latitude, 19.5° longitude. Panel A: Cross correlation between the phantom and reconstructed model for varying vertical extent (Longitudinal Extent: 0.4° Latitudinal Extent 0.2°.) Panel B: Cross correlation between the phantom and reconstructed model for varying Latitudinal extent (Vertical Extent: 8km, Longitudinal Extent 0.4°.). Panel C: Cross correlation between the phantom and reconstructed model for varying longitudinal extent (Vertical Extent: 8km Latitudinal Extent: 0.2°.) Panel D: Cross correlation between the phantom and reconstructed model for varying latitudinal and Longitudinal Extent (Vertical Extent: 8km)

Finally, figure 3.10 shows how varying the shape of the patch affects the cross correlation. Each patch is located at 69.5° latitude, 19.5° longitude, and at an altitude of 100km. If not being altered the vertical extent is 8km, longitudinal extent is 0.4° and the latitudinal extent is 0.2°. Panel A shows how the vertical extent of the patch affects the cross correlation. The highest correlation is between 10 and 25km with a correlation over 0.9. Below 10 km the correlation drops to a low of 0.47. Panel B shows how the latitudinal extent affects the cross correlation, between 0.11° and 1.1° the correlation is very low, indicating that for events with very small latitudinal extent they will not be resolved well. Above 1.1° the correlation is very high, indicating a good reconstruction. Panel C shows the effect of the longitudinal extent. The longitudinal extent has less effect, with all the values being greater than 0.86. Finally, Panel D shows a varying longitudinal and latitudinal extent. for latitudinal extent below 1.1 and longitudinal extent of 2.1 the correlation is between 0 and 0.8, indicating poor reconstruction. Above 1.1 and 2.1 the cross correlation is once again high, above 0.9.

While this is not a complete investigation of all the ways to vary the test phantoms, the tests carried out give some good indication into the reliability of the tomographic reconstruction. Starting with the layer phantom, as long as the vertical extent is not too great, between 2-10km the reconstruction should be reliable. With regards to the arc, again the vertical extent seems to be the controlling factor on the reconstruction, with a smaller vertical extent the reconstruction is the less reliable. The patch phantom has the most variability, in that if the longitudinal and latitudinal extent is below 1.1 and 2.1 respectively the patch will not be reconstructed.

3.5 Comparison with EISCAT

Between 14 and 24UT on the 22nd May 2008 the EISCAT VHF antenna was running the 'beata' program. This program measures electron densities down to the lower D-region. For this run the antenna was pointing near vertical. The electron density profile measured by EISCAT is converted to an absorption profile by the use of equation 1.46. It is assumed that the absorbed radio wave propagates nearly parallel to the magnetic field lines so the angle is 0° and X mode is selected to match observations.

Panel 1 of figure 3.11 shows the electron density profile measured by EISCAT between 19:00UT-20:00UT and 21:45UT-22:15UT. Enhanced electron density in the D-region can be observed between 19:05UT-19:30UT; 19:40-19:50UT and 21:50UT-22:15UT. Panel 2 shows the absorption profile derived from the electron densities. The height of maximum CNA as measured by EISCAT and calculated by the height triangulation and tomographic methods are shown in panel 4. The vertical parallax method failed to produce any results. During the absorption event between 19:00 UT and 19:30 UT the correlation between the three measurements falls within errors, estimating it to be on average 74 ± 5km. The height triangulation and tomography also reconstruct the absorption event between 21:45 UT and 22:15 UT. Between 19:40 and 19:50UT EISCAT observes a patch of absorption that none of the height estimation techniques can pick out. One possibility for this omission could be that this is a small scale event that cannot be resolved by the techniques, which is indicated by the analysis using test phantoms, which showed that for small patches, of scales of 0.1-0.2° are not well reconstructed. Panel 3 of figure 3.11 shows absorption plots of IRIS beam 9 and ARIES beam 656. These two beams intersect at 71km. Between 19:00 and 19:40 UT they show a similar pattern of absorption, consistent with the tomography and height triangulation results that indicate the height of peak CNA is 75km. Between 19:40-20:00UT ARIES records lesser absorption, consistent with

the EISCAT absorption values given the geometry of the overlapping IRIS, ARIES and EISCAT beams. The larger beam width (and hence vertical extent) of IRIS explains why it observes absorption at that time.

Figure 3.11: From top to bottom: 1. EISCAT Electron density. (log10(m^{-3})) 2. Absorption Profile using EISCAT Electron Density (dB/km). 3. Absorption in beam 9 of IRIS (solid line) and beam 656 of ARIES (dashed line) (dB). These beams intersect at 71km. 4. Vertical absorption profiles using the tomographic method (69.5° latitude, 19.2° longitude) with the peak height of CNA marked on in black from EISCAT. Error bars generated using the length of the range gate. Height triangulation method is marked in white (only cross correlation values over 0.6), 22nd May 2008, 19:00-22:30UT. Between 20:00 UT and 21:45 UT is not shown as there was no activity.

3.6 Estimating the characteristic energy

Estimates of the characteristic energy of the precipitating electrons are obtained by relating the height of maximum CNA to an assumed flux spectrum ϕ. Absorption is related to electron density by equation 1.46. The steady state ion production rate is given by $q = \alpha n^2$ (*Semeter and Kamalabadi* (2005)), or $n = \sqrt{q/\alpha}$, where n is the ion density, and α is the effective recombination rate.

3.6.1 Ion production rate

Described here is the procedure for calculating the ion production rate, q. Electrons with initial energy E > 300eV will follow a convoluted path until stopped. *Rees* (1989) states that this effective range can be expressed by the empirical formula:

$$R(E) = 4.30 \times 10^{-3} + 5.36 \times 10^{-2} E^{1.67} \tag{3.17}$$

where E is in Kev and $R(E)$ is measured in mass distance, kg m^{-2}. Secondly the atmospheric scattering depth s (kg m^-2) is given by the formula:

$$s = \int_z^\infty \rho dz \tag{3.18}$$

where ρ is the atmospheric mass density. For this study ρ is calculated using the Mass Spectrometer and Incoherent Scatter (MSIS 90) model. The electrons traveling along their range R(E) do not distribute their energy uniformly along the range but reaches a maximum at some point from the source. This can be represented by the energy dissipation distribution, Λ, which is a function of the fractional range s/R. Table 1 of *Semeter and Kamalabadi* (2005) lists the values of Λ for an Isotropic Pitch angle distribution. Electrons of greater than a few Kev have an isotropic distribution and provide the best description of the dynamic aurora (*Semeter and Kamalabadi* (2005)).

The energy deposition function is the rate of energy loss per unit volume as a function of altitude and energy with units (eV m^{-3} s^{-1}). For monoenergetic electrons at Energy E, this can be expressed by

$$\varepsilon(z, E) = q(z)\Delta\varepsilon_{ion} = \frac{FE\Lambda\rho}{R} \tag{3.19}$$

F is electron number flux (m^{-2} s^{-1}), E is the electron energy (eV), ρ is the mass density (kg m^{-3}), R is the range (kg m^{-2}) and Λ is the energy dissipation function. The energy deposition rate is a function of the ionization rate q(z) and energy loss per ion formation $\Delta\varepsilon_{ion}$. A well known empirical value for $\Delta\varepsilon_{ion}$ is ~35.5 eV. Rewriting equation (3.19) in terms of the ionization rate yields

$$q(z, E) = \frac{FE\Lambda\rho}{35.5R} \tag{3.20}$$

Equation (3.20) can be rewritten for an arbitrary electron spectra ϕ(E)

$$q(z) = \int_{E_{min}}^{E_{nax}} \frac{FE\Lambda\rho}{35.5R}\phi(E)dE \tag{3.21}$$

Semeter and Kamalabadi (2005) show that by manipulating equation (3.21) it can be written in matrix form

$$\mathbf{q} = \mathbf{A}\phi \tag{3.22}$$

where **A** has elements

$$A_{ij} = A(z_i, E_j)\Delta E_j = \frac{\Lambda(\frac{s(z_i)}{R(E_j)})\rho(z_i)E_j\Delta E_j}{35.5R(E_j)} \tag{3.23}$$

ϕ is the differential number flux, integrated over pitch angle in the downward hemisphere and has units m^{-2} $s^{-1}eV^{-1}$.

3.6.2 Flux spectrum

Various flux spectra can be used to describe the distribution of incoming electrons. A Maxwellian spectrum is used for this study, given by

$$\phi(E) = \frac{Q_0}{2E_C^3} E \exp\left(-\frac{E}{E_c}\right) \tag{3.24}$$

ϕ is the number flux directed in the downward direction for an isotropic distribution of electrons (m^{-2} s^{-1} eV^{-1}). Q_0 is the total energy flux (eV m^{-2} s^{-1}), E_c is the characteristic energy (eV) and E is the energy of the electrons (eV). A value of 6.452 x 10^{15} (eV m^{-2} s^{-1}) is used for the total energy flux, this is 1 mW/m^2, a convention used in papers such as *Senior et al.* (2007).

3.6.3 Effective recombination coefficient

The calculation of the ion density still requires the use of a suitable recombination coefficient. Due to the complicated nature of the lower ionosphere, where most auroral activity takes place, the calculation of an effective recombination coefficient is not trivial. In this study two recombination rates are used, one from *del Pozo et al.* (1997) and one from *Vickrey et al.* (1982) to give an estimation of the boundary values for the characteristic energy.

$$\alpha_{delpozo} = 2.5 \times 10^{-6} \exp(-0.0242h) + 1.63 \times 10^{11} \exp(-0.524h) \tag{3.25}$$

$$\alpha_{Vickrey} = 2.5 \times 10^{-6} \exp(-h/51.2); \tag{3.26}$$

α is the effective recombination rate (cm^3 s^{-1}), h is the height in kilometers.

3.6.4 Calculation of Absorption

The final step is to use the electron density n, to calculate the Absorption. Absorption is related to the electron density by equation 1.46.

The effective electron collision frequencies, are described by the sum of the electron-ion and electron-neutral collisions, given by *Schunk and Nagy* (1978) as:

$$v_{eff} = \langle v_{en} \rangle + \langle v_{ei} \rangle \tag{3.27}$$

electron ion frequency, v_{en} is given by the equation

$$v_{ei} = \frac{8\pi}{3} \cdot \frac{Z^2 e^4 N_i}{(2m_e\pi)^{1/2}(kT_e)^{1/2}} \cdot \ln \left[\frac{k^{3/2}}{1.78Ze^3} \cdot \left(\frac{T_e^3}{N_e\pi} \right)^{1/2} \cdot \left(\frac{T_i}{ZT_e + T_i} \right)^{1/2} \right] \tag{3.28}$$

where m_e, N_e and T_e are the electron mass number, electron density and electron temperature respectively. Z, N_i and T_i are the atomic charge, ion density and ion temperature respectively. k is the Boltzmann constant. The neutral collision frequency is derived from the sum of all the collision frequencies between the electron and neutral species of the atmosphere. The collision frequencies for the major neutral species are given by *Schunk and Nagy* (1978) as:

$$\begin{aligned}
\langle v_{eN_2} \rangle &= 2.33 \times 10^{-11} N(N_2)(1 - 1.121 \times 10^{-4} T_e) T_e \\
\langle v_{e0_2} \rangle &= 1.82 \times 10^{-10} N(O_2)(1 + 1.36 \times 10^{-2} T_e^{1/2}) T_e^{1/2} \\
\langle v_{e0} \rangle &= 8.9 \times 10^{-11} N(O)(1 + 5.7 \times 10^{-4} T_e) T_e^{1/2} \\
\langle v_{eHe} \rangle &= 4.6 \times 10^{-10} N(He) T_e^{1/2} \\
\langle v_{eH} \rangle &= 4.5 \times 10^{-9} N(H)(1 - 1.35 \times 10^{-4} T_e) T_e^{1/2}
\end{aligned} \tag{3.29}$$

Values for the ion and neutral species and temperatures are taken from the International Reference Ionosphere (IRI 2001) and MSIS90. IRI 2001 requires the variables date, time, latitude and longitude, whereas the MSIS 90 requires

additional parameters of Ap and f10.7 for the previous day and for the previous month.

To relate the height of maximum CNA to characteristic energy, absorption profiles are calculated using equation 1.46, calculating the ion production rate by the method set out above using values between 1 keV and 300 keV for the characteristic energy. The height of maximum absorption is plotted against the characteristic energy for each characteristic energy value to deduce the value of characteristic energy for a specific height of maximum CNA in each of the case studies.

3.6.5 Factors controlling a model between peak height of CNA and characteristic energy

The calculation of absorption from an assumed flux spectrum has a number of variables that need to be calculated. This section investigates how the choice of values of these variables affects the resulting height of max CNA for different energies. If otherwise stated the *del Pozo et al.* (1997) effective recombination coefficient is used, for the 12 August 2007 12:00UT.

Firstly, the choice of effective recombination coefficient is not trivial, due to the complicated nature of the lower ionosphere. Plot A of figure 3.12 shows the effective recombination coefficients of *Vickrey et al.* (1982) and *del Pozo et al.* (1997). The *Vickrey et al.* (1982) effective recombination coefficient was derived primarily for the E-region, so above 85km, whereas *del Pozo et al.* (1997) includes more of the D-region. However neither can be reliable under 80km as the chemistry of this region is so variable and hard to model. Panel B shows electron density profiles created using the different effective recombination coefficients. The electron density profile using the *Vickrey et al.* (1982) effective recombination coefficient has higher electron densities at lower altitudes, but less at higher altitudes when

compared with the electron density profile using the *del Pozo et al.* (1997) effective recombination coefficient. By plotting the height of maximum CNA against characteristic energy, figure 3.13 shows the difference the choice of recombination coefficient has. Between 100km and 85km the height of maximum CNA and characteristic energy is fairly equal between the two, however below 85km they diverge dramatically with a difference in energy of around 25keV at 80km. This shows how varying the results can be for the characteristic energy in the lower ionosphere when choosing a different recombination coefficient.

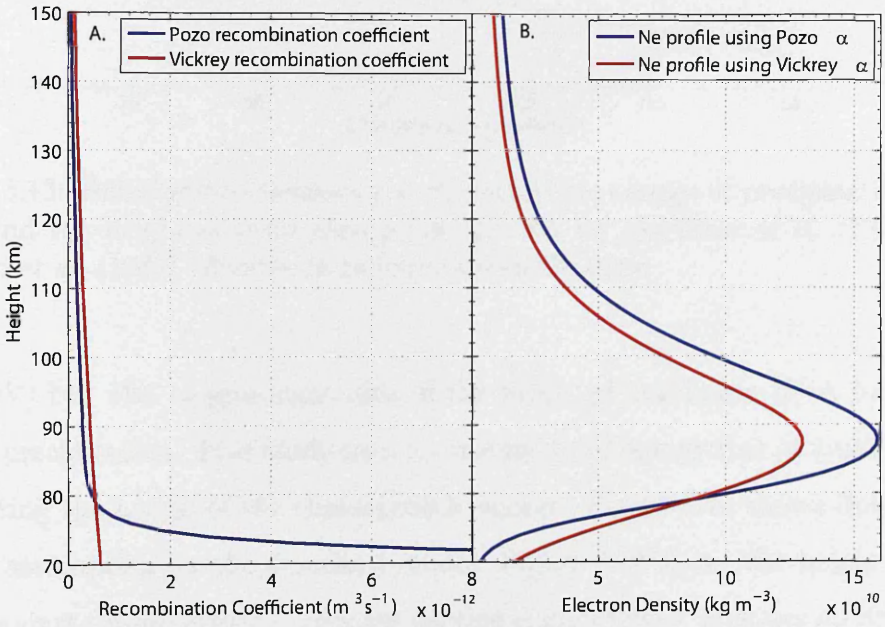

Figure 3.12: A. *del Pozo et al.* (1997) and *Vickrey et al.* (1982) effective recombination coefficient. B. Electron density profile for electrons with mean energy of 80keV for *del Pozo et al.* (1997) and *Vickrey et al.* (1982) effective recombination coefficients.

The following graphs plot characteristic energy against the height of maximum CNA. For a given characteristic energy, the flux is calculated, and then from this the absorption profile, as described in section 3.6.4. The characteristic energy used is then plotted against the height of maximum CNA from the absorption profile. Values of 1, 2, 10, 20, 40, 80 and 160keV are used for the calculations. These values were chosen to give a good spread across the main energy range of interest

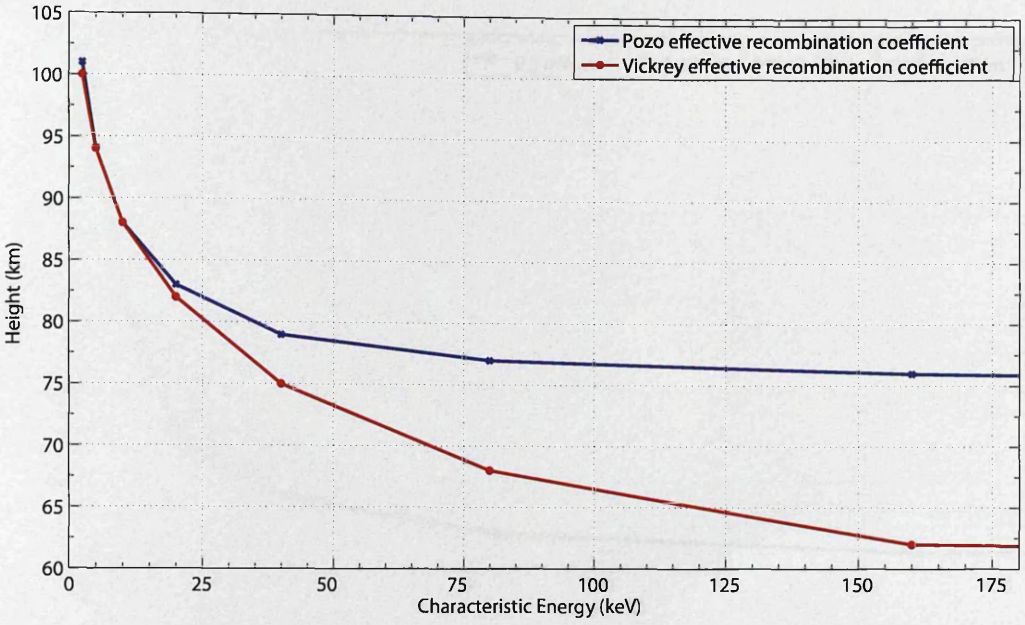

Figure 3.13: Relationship between the characteristic energy of precipitating electrons and the height of peak absorption of CNA for *del Pozo et al.* (1997) and *Vickrey et al.* (1982) effective recombination coefficients.

(1-30keV) but also to give some idea of the height of maximum CNA for higher energy precipitation. This study uses a constant total energy flux of 1mW/m^2 for calculating the height of the characteristic energy. Figure 3.14 shows that this is a valid assumption for the described model. Figure 3.14 shows the height of max CNA against characteristic energy for varying energy fluxes, it shows no difference between the height of max CNA and energy for any of the values of total energy flux.

F10.7 values are required as an input to the MSIS90 model. The MSIS 90 model provides the values for the neutral species. *Dalagarno and Henry* (1965) state the effects of solar activity, photodetachment of electrons and photodissociation of ions have little effect on D region electron temperatures, due to the far greater dominance of the collision frequency of thermal electrons, so we would expect that the value of F10.7 would have little effect on the resulting height of maximum CNA versus characteristic energy. Figure 3.15 shows the height of maximum CNA versus

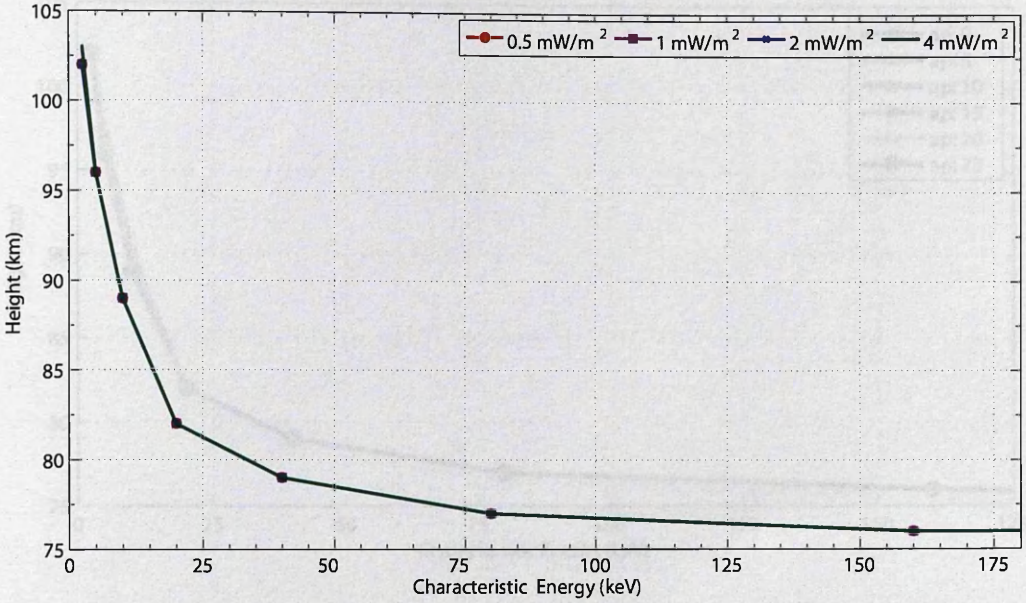

Figure 3.14: Relationship between the characteristic energy of precipitating electrons and height of peak absorption of CNA for varying electron fluxes.

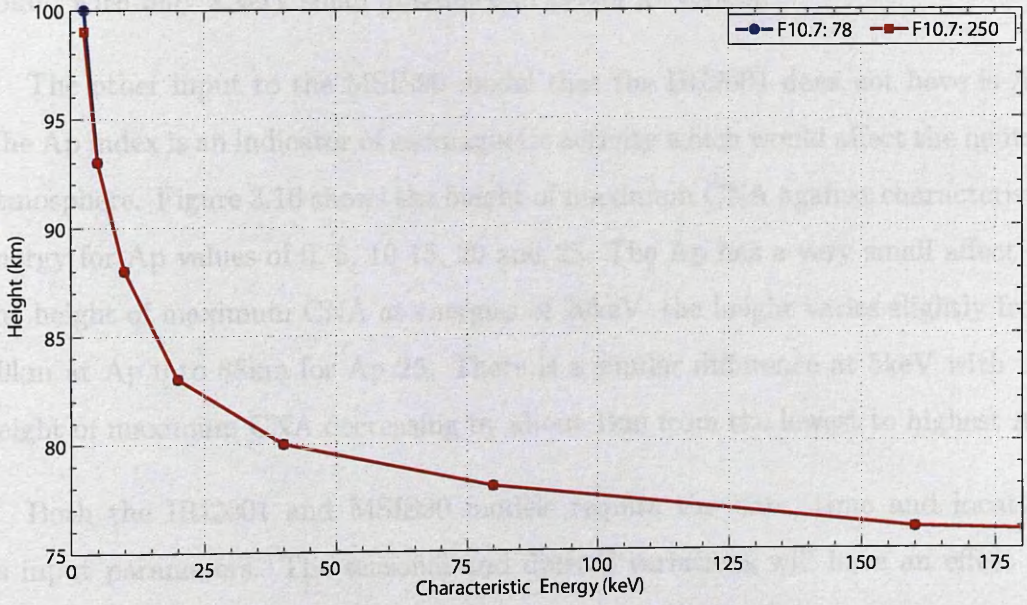

Figure 3.15: Relationship between the characteristic energy of precipitating electrons and height of peak absorption of CNA for varying levels of F10.7.

characteristic energy for two values of F10.7, an average 78 and a more extreme 250. There is no difference between the low value and high value of F10.7. below

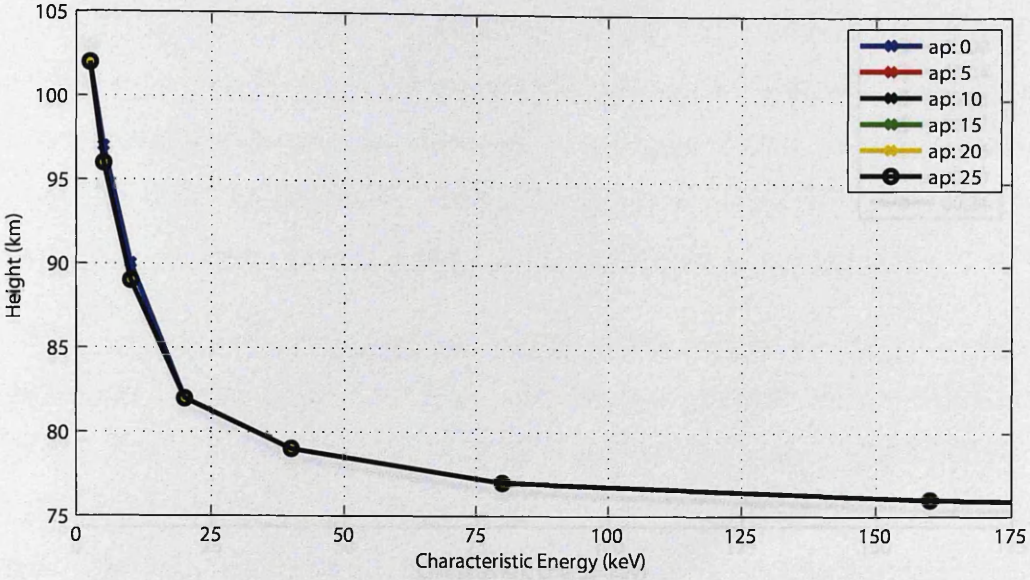

Figure 3.16: Relationship between the characteristic energy of precipitating electrons and height of peak absorption of CNA for varying levels of Ap.

95km, with only a very small difference in height at 100km.

The other input to the MSIS90 model that the IRI2001 does not have is Ap. The Ap index is an indicator of geomagnetic activity which would affect the neutral atmosphere. Figure 3.16 shows the height of maximum CNA against characteristic energy for Ap values of 0, 5, 10 15, 20 and 25. The Ap has a very small affect on the height of maximum CNA at energies of 20keV, the height varies slightly from 90km at Ap 0 to 88km for Ap 25. There is a similar difference at 5keV with the height of maximum CNA decreasing by about 1km from the lowest to highest Ap.

Both the IRI2001 and MSIS90 models require the date, time and location as input parameters. The seasonal and diurnal variations will have an effect on calculation of the effective collision frequencies as there will be variations in the electron temperatures, ion temperatures and neutral and ion species densities. Figure 3.17 shows the height of maximum CNA against characteristic energy for different times during the day. The effect of the time of day is seen above 85km. At 1keV there is a 2km difference depending on the time of day. This same difference

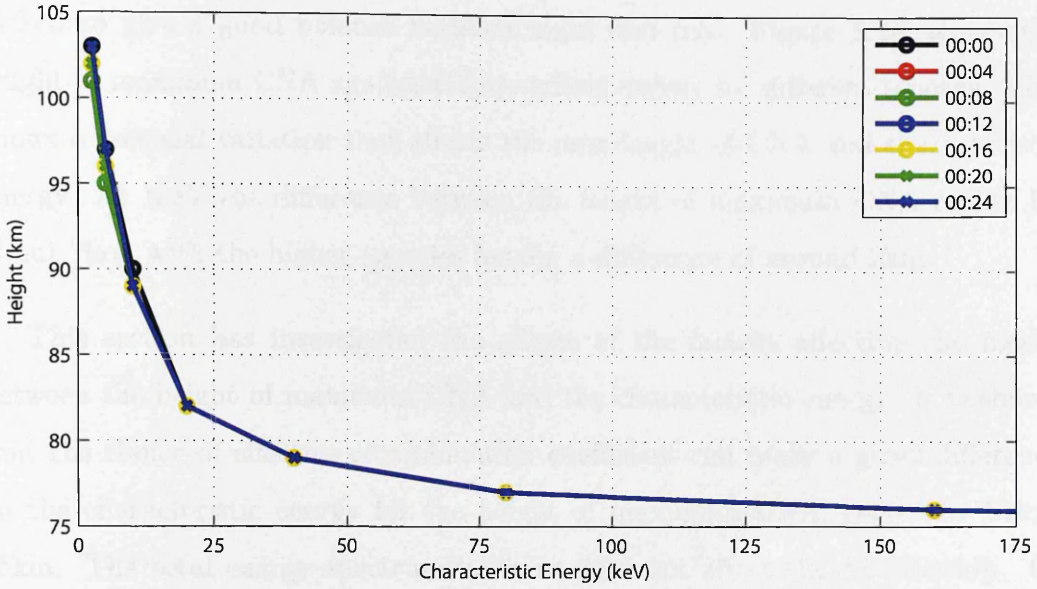

Figure 3.17: Relationship between the characteristic energy of precipitating electrons and height of peak absorption of CNA for different times of day. 17 October 2007

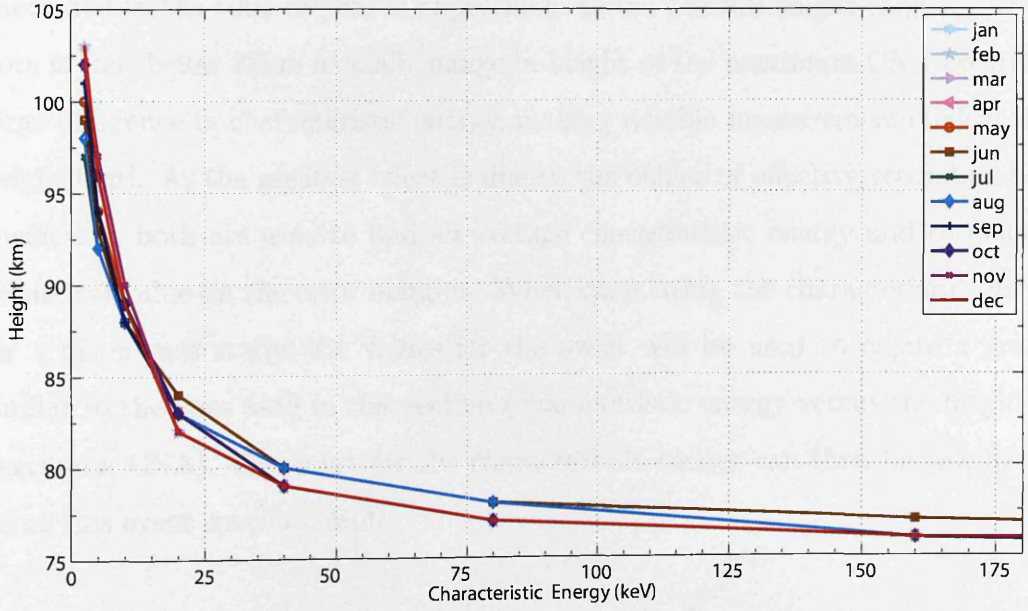

Figure 3.18: Relationship between the mean energy of precipitating electrons and height of peak absorption of CNA for different months.

of 2km is seen at 2keV, with a range between 95 and 97km. Below 85km however the time of day does not show an effect. The day was 17 October 2007, a day

picked to give a good balance between night and day. Figure 3.18, shows the height of maximum CNA against characteristic energy for different months. This shows a seasonal variation that affects the max height of CNA and characteristic energy. At 1keV the difference between the height of maximum CNA ranges by about 7km, with the higher energies having a difference of around 2km.

This section has investigated the effects of the factors affecting the model between the height of maximum CNA and the characteristic energy. It is shown that the choice of effective recombination coefficient can make a great difference on the characteristic energy for the height of maximum CNA, especially below 85km. The total energy spectrum however does not affect the relationship. Of the input parameters of the MSIS90 and IRI2001 models, only the Ap and time of year have any noticeable effect on the characteristic energy, height of maximum CNA relationship. The effect of Ap is the most prominent below 85km, while the effect due to the time of year is appreciable across the full height range. Also of note is that below 85km a small change in height of the maximum CNA creates a large difference in characteristic energy, making reliable measurements below this height hard. As the greatest effect is due to the choice of effective recombination coefficient, both are used to find an average characteristic energy and to place a numerical value on the error margins. When calculating the characteristic energy for a given case study, the values for the event will be used to create a graph similar to the ones used in this section (characteristic energy versus the height of maximum CNA). The value for the characteristic energy can then be calculated using this event specific graph.

3.7 Case Studies

In this section we apply the height triangulation and tomographic technique to three different types of CNA to examine the differences in deposition height. The

vertical absorption profiles from the tomographic methods are averaged to give a mean absorption profile for the field of view. Each event is similar to one of the phantoms discussed in section 3.

3.7.1 Substorm Spike Event

Figure 3.19 shows the AL, AU and SYM-H magnetic indices for 23rd December 2007. The SYM-H index shows a small negative deflection for the course of the day, ranging from -10nT at 12:00UT to -25nT at 21:20UT, indicating the event occurred during a weak storm time event, with the case study occurring at the same time as activity in the AU and AL index. The start of the substorm is marked on the figure by the vertical dotted line at 21:20UT. At this time there is a negative deflection in the AL index to -300nT. The substorm occurred during a period of high solar wind velocity as shown in figure 3.20. The flow speed is shown in the second panel and is fairly constant during the course of the day, slowly decreasing from 600km/s at 00:00UT to 450km/s at 24:00UT. There was a period of sustained negative Bz of around -3 nT in the interplanetary magnetic field (IMF) as identified by OMNI data set shown in the first panel, from 12:00UT the Bz was predominantly negative up to the event start at 21:20UT, this provided low but sustained coupling of the IMF to the magnetosphere and led to the onset of a substorm at 21:20 UT, observed by the IMAGE magnetometer chain seen in figure 3.21. Magnetometers are shown ranging from 78° degrees North to 58° North. The four magnetometers ranging from 67-78°N show a negative deflection of around 200nT at 21:20 indicating the presence of a substorm.

Figure 3.22 shows absorption data for the event in question. Panel (A) shows a 100 nT negative bay in the X component from the Kilpisjärvi magnetometer. IRIS measured an absorption spike (e.g. *Aminaei et al.* (2006)) in the northwest quadrant of its field of view. Panel (B) shows the absorption in beam 9 of IRIS between 21:15 and 21:30 UT with the corresponding height estimates shown in

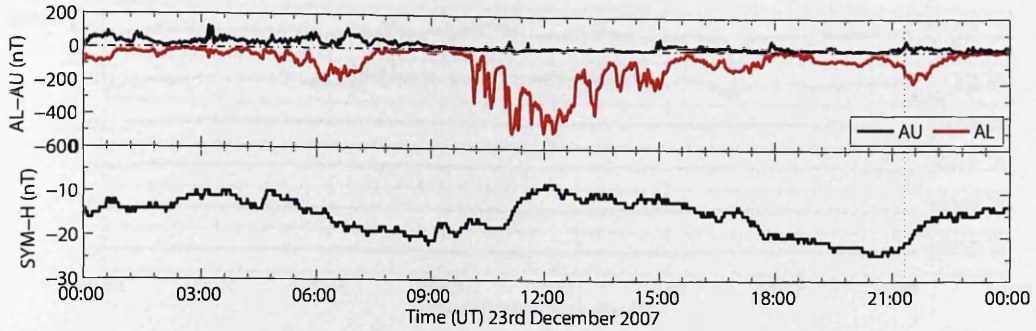

Figure 3.19: Magnetic indices for substorm spike case study. Top panel: AL (red) and AU (black) indices. Bottom panel: SYM-H index. (Vertical dotted line indicates the onset of the absorption event.)

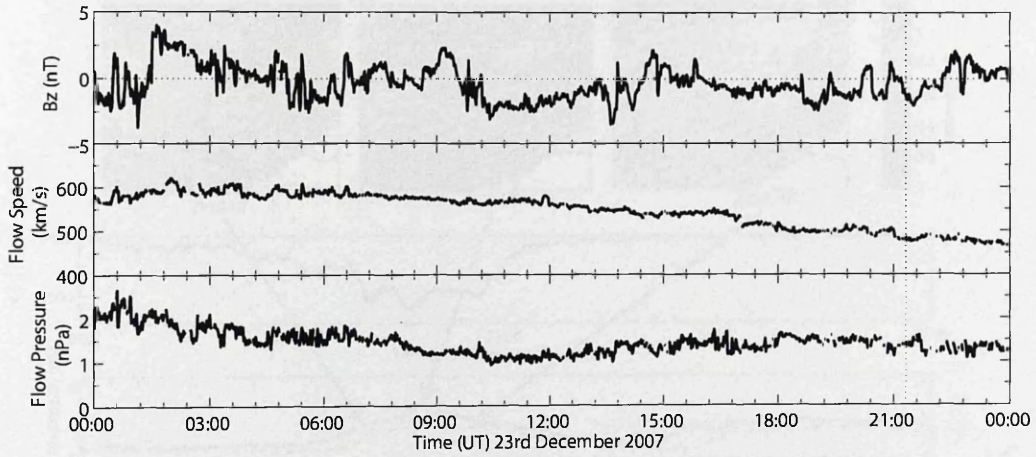

Figure 3.20: Solar Wind conditions for substorm spike case study. Top panel: Bz. Middle Panel: Solar wind velocity. Bottom Panel: Solar wind Pressure. (Vertical dotted line indicates the onset of the absorption event.)

panel (C); the duration of the spike was 5 minutes. As the event progresses the height triangulation method show a decrease in peak altitude from 100 +/-3 km to 92 +/- 3km where there is a local maximum in total absorption of 1.4 dB. The tomographic method shows a more constant height across the event at 95 +/- 3km which then decreases height to 85+/- 3km as the event continues. The characteristic energy changes from 5 keV to a peak of 14-15 keV. This variation indicates a rapid hardening of the electron spectrum during the spike event in agreement with other studies (*Collis and Hargreaves* (1997)) and suggests that the

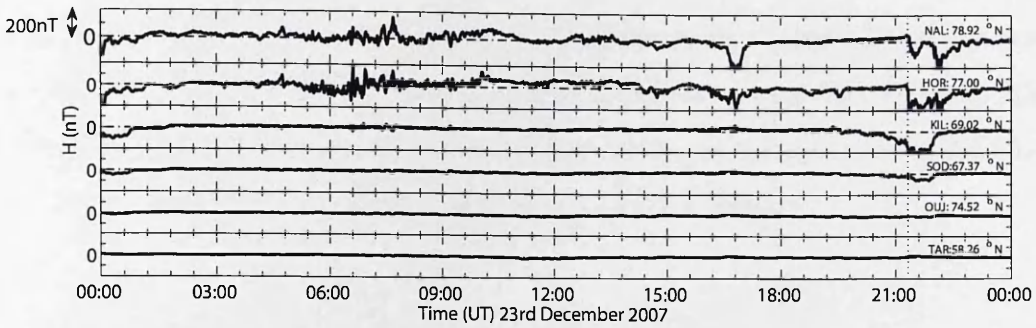

Figure 3.21: IMAGE magnetometer data for substorm spike case study Stations are plotted in descending order of latitude. (Vertical dotted line indicates the onset of the absorption event.)

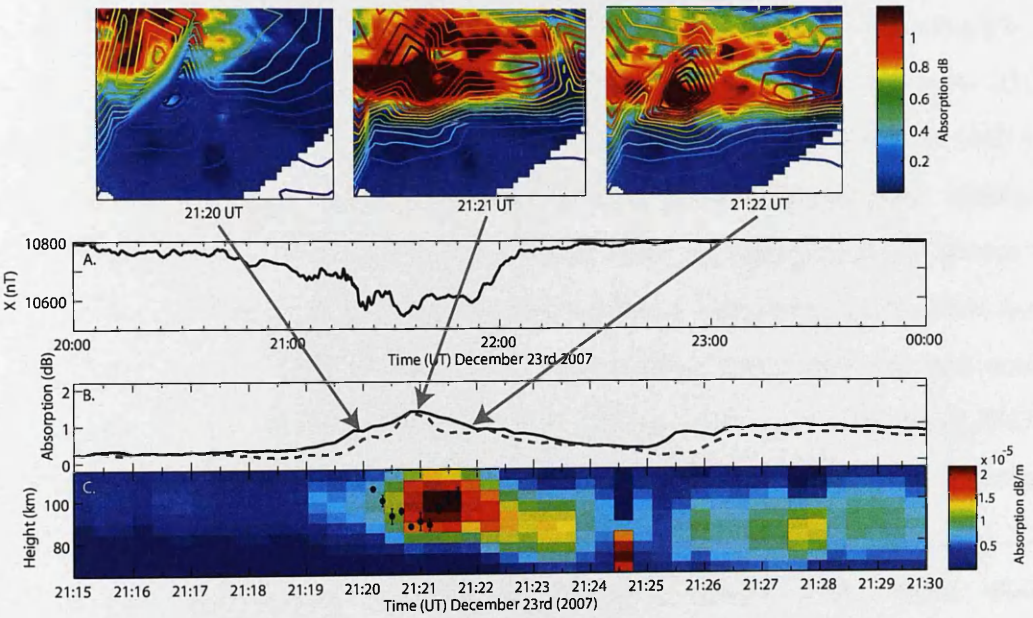

Figure 3.22: Panel plot for absorption event on the 23rd December 2007. Top: ARIES absorption images with IRIS contour plot overlaid projected to a height of 90km. Panel A shows the X-component of the IMAGE magnetometer at Kilpisjärvi between 20:00 and 00:00 UT. Panel B shows absorption between 21:15 and 21:30 UT for beam 9 in IRIS (solid line) and beam 560 in ARIES (dashed line) (dB). These two beams intersect at 85km. Panel C shows mean absorption profiles using the tomographic method, with the height of maximum CNA using the height triangulation marked on in black (cross correlation values over 0.6).

CNA associated with the spike is formed by the energetic tail of auroral electrons. Three absorption images in figure 3.22 show the evolution of the CNA patches;

at 21:21 UT there is a discrete patch which increases in magnitude as the event progresses. By 21:22 UT there are two distinct patches in the field of view. This is also the time at which the height estimation technique breaks down, most likely due to the two different patches occurring at different heights.

3.7.2 Slowly Varying Absorption (SVA)

Figure 3.23 (panel (A)) shows an example of slowly varying absorption; a common feature in the auroral zone, characterized by a smooth increase and decrease in the CNA over a period of a few hours (*Devlin et al.* (1986)). This example is from the 4 October 2007 when there was a long period of CNA between 03:30 and 06:30 UT. This is likely generated by electrons gradient-curvature drifting eastward in the magnetosphere and precipitating via interaction with whistler-mode chorus waves. Observations of the solar wind for this period are shown in figure 3.25. It shows a minor but sustained negative deflection in the IMF from midnight to around 04:00 UT, with solar wind velocity being constant just under 600km/s. Magnetic indicies for this event (figure 3.24) again show weak SYM-H, of around -20nT activity with moderate AL activity peaking at -550UT during the absorption event The IMAGE magnetometer chain, as shown in figure 3.26 observes no change in the H component during the course of this event, which is in keeping with SVA events. Figure 3.27 shows magnetometer data from the Churchill line of CARISMA network. The Gillam magnetometer shows a substorm onset just before 03:00 UT. This substorm is the probably cause of the drifting electrons.

During the onset (03:30-04:00 UT) of absorption the height of maximum CNA is 82 +/- 5km (Panel (B), figure 3.23). The top panel of figure 3.23 show how the event progressed with a discrete structure becoming steadily more diffuse. The height triangulation breaks down over the course of this transition; as the CNA becomes more diffuse the error on the height increases to +/- 20km, whereas the

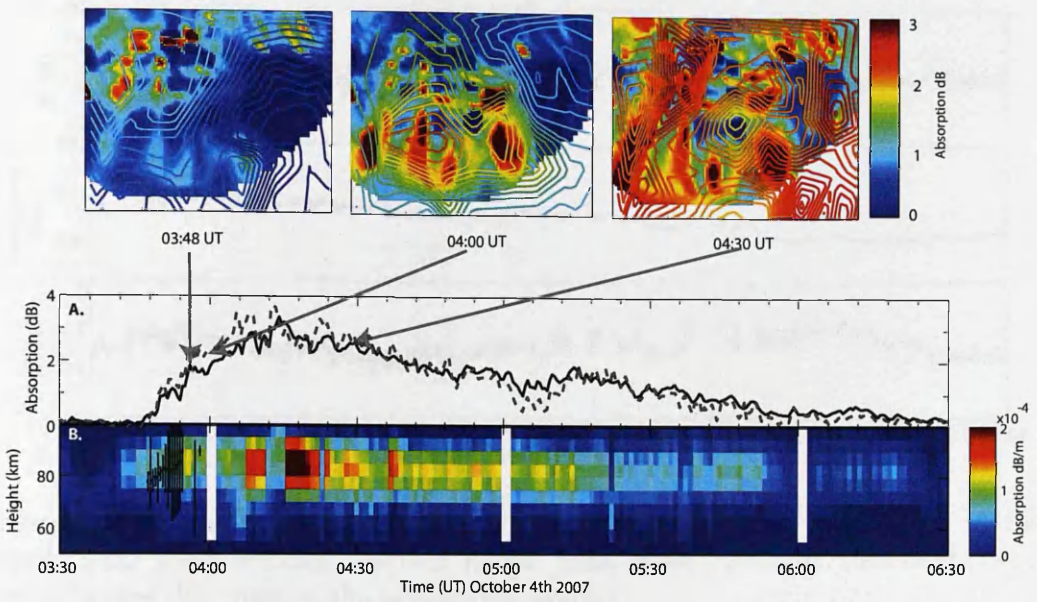

Figure 3.23: Panel plot for absorption event on the 4th October 2007. Top: ARIES absorption images with IRIS contour plot overlaid projected to a height of 85km (dB). Panel A shows absorption between 03:30 and 06:30UT in beam 25 of IRIS (solid line) and beam 792 of ARIES (dashed line) (dB). These beams intersect at 80km. Panel B shows mean absorption profiles using the tomographic method, with the height of maximum CNA using the height triangulation marked on in black (cross correlation values over 0.6).

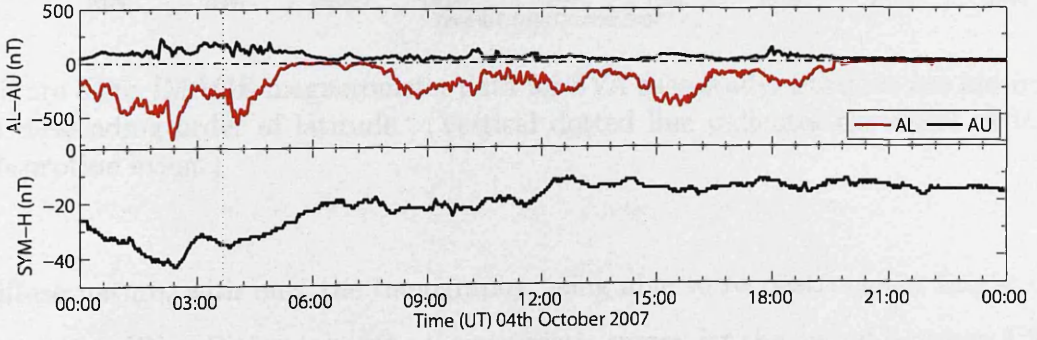

Figure 3.24: Magnetic indices for SVA case study. Top panel: AL (red) and AU (black) indices. Bottom panel: SYM-H index. (Vertical dotted line indicates the onset of the absorption event.)

tomographic method still reconstructs the event, showing an increase in the height to around 87+/-3km. This structure is similar to the stratified layer discussed in section 3, where the height triangulation method also failed to work due to its

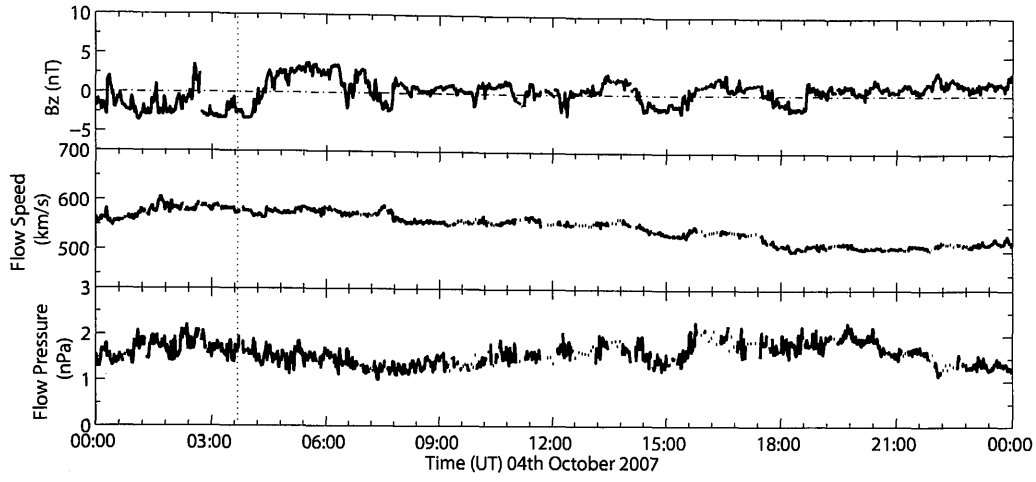

Figure 3.25: Solar Wind conditions for SVA case study. Top panel: Bz. Middle Panel: Solar wind velocity. Bottom Panel: Solar wind Pressure. (Vertical dotted line indicates the onset of the absorption event.)

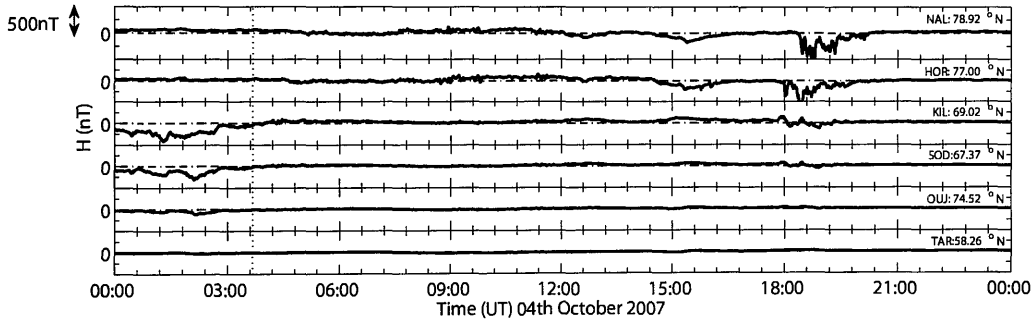

Figure 3.26: IMAGE magnetometer data for SVA case study. Stations are plotted in descending order of latitude. (Vertical dotted line indicates the onset of the absorption event.)

diffuse nature, with only the tomography being able to reconstruct the height of maximum CNA. Estimates of the characteristic energy for the period between 3:30 UT and 3:45 UT is 18-20 keV. The energy is larger than for the substorm spike in agreement with past studies (e.g. *Osepian et al.* (1996)), however a more general deduction would require a full statistical study of these types of events.

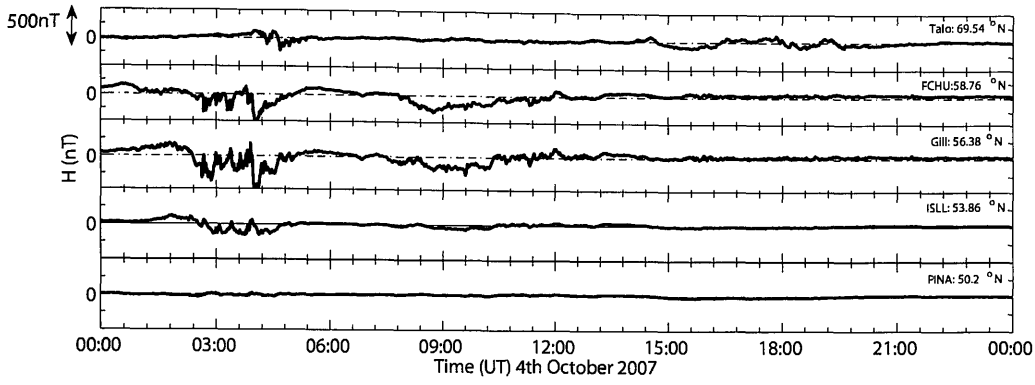

Figure 3.27: CARISMA Churchill line magnetometer data for SVA case study. Stations are plotted in descending order of latitude.

3.7.3 Afternoon CNA Spike

Figure 3.28 shows data from IRIS and ARIES for a short duration (4 minutes) spike at 14:57 UT on 4 October 2007. The local magnetometer recorded only a very small positive deflection in the H component, as can be seen in figure 3.29 and this event cannot be explained as a sudden commencement effect. One possibility is that this event is an example of a high-latitude absorption spike (*Ranta et al.* (1997)). These events are short lived with relatively low absorption ($<$ 1 dB), exhibiting horizontal structure of $\sim$180 by 130 km at 90 km altitude (*Ranta et al.* (1997)).

Observations of magnetic indices, figure 3.30 and solar wind parameters, figure 3.31 indicate this absorption event started shortly after the commencement of a geomagnetic storm. The SYM-H magnetic index shows the onset of a sudden storm commencement at around 12UT, with the afternoon absorption event occurring with the onset of the main phase of the geomagnetic storm at just before 14UT. Auroral activity at the this time is increased as shown by the AU and AL indices. The solar wind parameters show the signatures consistent with a geomagnetic storm, with the solar wind increasing from the slow solar wind speeds of around 200km/s rapidly increasing to 450km/s over a period of 9 hours, and increase of

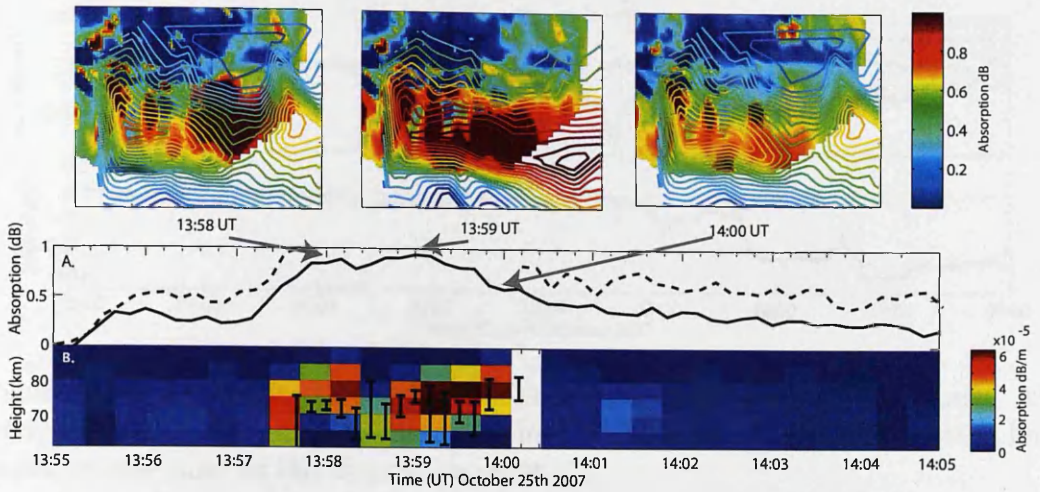

Figure 3.28: Panel Plot for absorption event on 25th October 2007. Top: ARIES absorption images with IRIS contour plot overlaid projected to a height of 75km (dB). Panel A shows absorption between 14:55 and 15:05 in beam 25 of IRIS (solid line) and beam 824 of ARIES (dashed line) (dB). These beams intersect at 72km. Panel B shows mean absorption profiles using the tomographic method, with the height of maximum CNA using the height triangulation marked on in black (cross correlation values over 0.6).

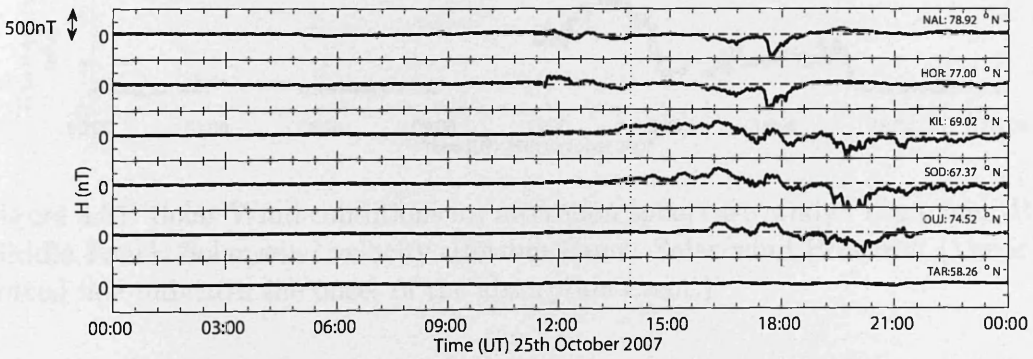

Figure 3.29: IMAGE magnetometer data for afternoon spike case study. Stations are plotted in descending order of latitude. (Vertical dotted line indicates the onset of the absorption event.)

solar wind pressure by nearly a factor 10 starting between 9-12UT.

Panel (B) of figure 3.28 shows the height estimates of this absorption event, which is centered around 75 +/- 5 km according to the height triangulation and tomographic method. The absorption images in figure 3.28 show an arc like struc-

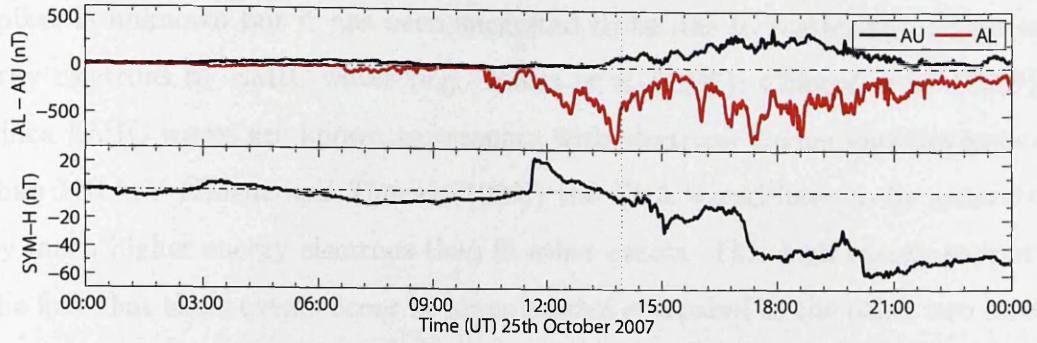

Figure 3.30: Magnetic indices for afternoon spike case study. Top panel: AL (red) and AU (black) indices. Bottom panel: SYM-H index. (Vertical dotted line indicates the onset of the absorption event.)

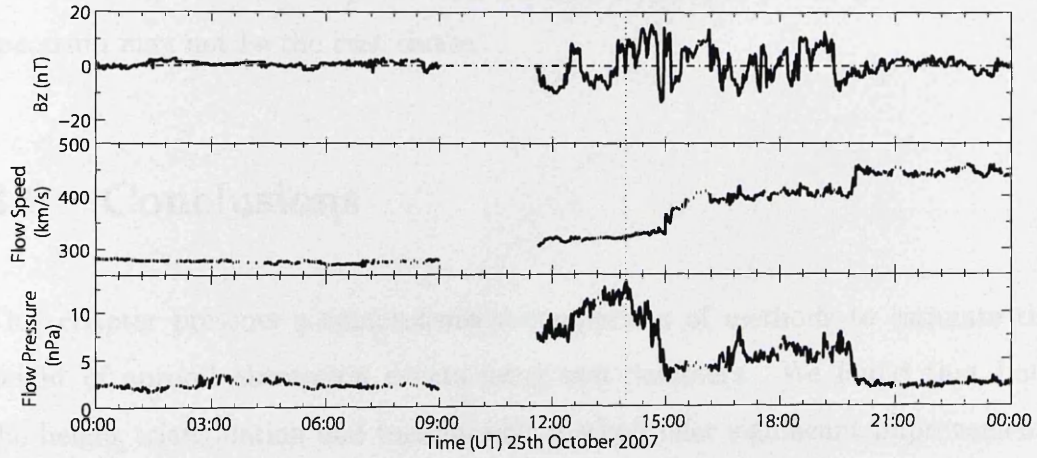

Figure 3.31: Solar Wind conditions for afternoon spike case study. Top panel: Bz. Middle Panel: Solar wind velocity. Bottom Panel: Solar wind Pressure. (Vertical dotted line indicates the onset of the absorption event.)

ture that moves across the field of view. This is similar in shape to the arc phantom in section 3.4. The match between the height triangulation and tomographic reconstruction is good for this case study, although there seems to be around a 5km difference between the two at some points, with the height triangulation being the lower value. It is a prerequisite that the patch is at a constant height across the field of view for the height triangulation to work correctly, this may bring into question this assumption for these times, especially for a case such as this where the event is short lived, intense and dynamic. The exact cause of these

spikes is unknown but it has been suggested to be due to scattering of high energy electrons by EMIC waves (e.g. *Ranta et al.* (1997); *Clilverd et al.* (2007)). Since EMIC waves are known to resonate with electrons having energies greater than 100 keV (*Horne and Thorne* (1998)) the CNA would have to be generated by much higher energy electrons than in other events. This high energy supports the fact that these events occur at lower heights compared to the other two cases. More accurate estimates of the characteristic energy cannot be specified for this event since at this altitude the composition of the ionosphere is more complicated, with greater inaccuracies in the recombination rate, coupled with the fact that the distribution of incoming electrons is largely unknown, meaning a Maxwellian spectrum may not be the best choice.

3.8 Conclusions

This chapter presents a comprehensive comparison of methods to estimate the height of auroral absorption events using two riometers. We found that both the height triangulation and tomographic method offer significant improvements over the vertical parallax method for IRIS-ARIES observations. The tomographic method provides an estimate of the height of peak CNA at the expense of the exact values of the CNA. The required smoothing of the differential absorption values retains the shape of the absorption profile but leads to an unavoidable underestimate of the integral value. This can be seen in the test phantoms. The height triangulation and tomographic methods described are successfully employed on real absorption data. Comparison with absorption plots created from electron density measurements from the EISCAT mainland radar show for this case that the height triangulation and tomographic method work for the majority of the events. The height triangulation works for discrete, single patches of absorption, however its validity is questionable when absorption is too diffuse or has multiple patches at different altitude in the field of view. This is represented in the height triangulation

normally with a cross correlation value of less than 0.6. The height triangulation and tomographic methods offer an improvement over previous methods (*Terkildsen et al.* (2004)), with ability to work on more absorption types, and give estimates on the height of maximum CNA to a resolution of ~10 seconds.

The height triangulation and tomographic methods were applied to three case studies; a spike at substorm onset, slowly varying absorption, and a daytime absorption spike. Application of the vertical parallax method were not possible on the three case studies. This is due to the fact that for each case study the absorption patch did not move across the field of view and keep a constant structure for time scales required for successful height estimates using this method. The tomographic method agreed with the height triangulation method for each event.

It can be seen in the comparison with EISCAT as well as the substorm spike event that the height triangulation begins before the tomographic method. This is due to the vertical profile chosen to represent the tomographic method. Figure 3.32 shows a diagram explaining the discrepancy. A. represents the vertical profile shown from the tomographic method. t=1 and t=10 show how the absorption event progresses over a period of time. As you can see the absorption event can begin before it is seen in the vertical profile of the tomographic method. This is why for these two cases the event beginnings do not match up as closely as the other two events described in this chapter.

Estimating the characteristic energy from the height of peak CNA is investigated. Using an assumed spectrum the characteristic energy can be estimated for different peak heights of CNA. Investigations of this relationship showed that the greatest factors that effect the energy estimations for a fixed spectrum are: the effective recombination coefficient and the time of year. The choice of effective recombination coefficient is particularly difficult for the D region due its complicated chemistry. The time of year is a model input parameter to the MSIS-90 and IRI2001 models, and is the only parameter that has a significant effect on the

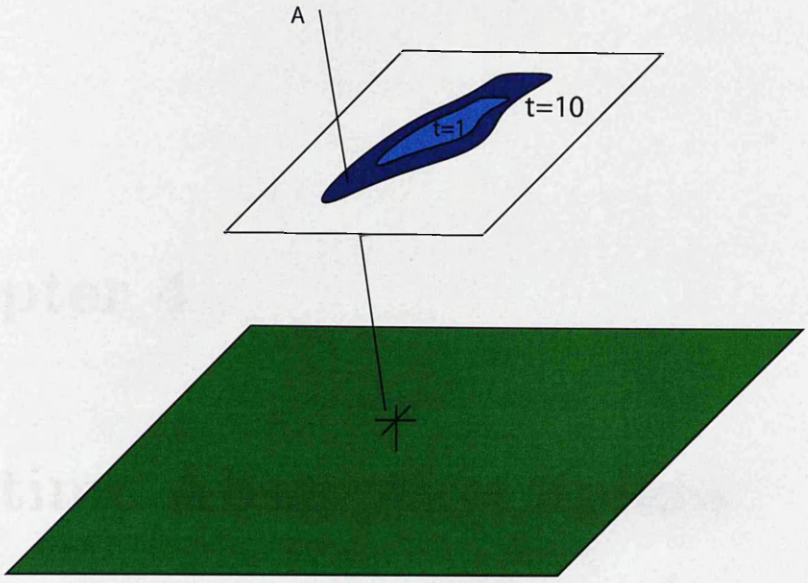

Figure 3.32: Diagram showing time discrepancy between tomographic method and height triangulation. A. Vertical profile shown from tomographic method. t=1: Beginning of absorption event at a given height. t=10 Spread of absorption event during the course of the event.

final energy estimates, with other factors such as AP, f10.7 and diurnal variation showing lessened effect below 90km.

Applying an assumed Maxwellian spectrum, estimates of the characteristic energy using the height of maximum CNA were done for the three case studies. The values for the characteristic energy for the substorm spike was 5keV and the beginning of the slowly varying absorption at 18-20keV. The energy of the afternoon spike event could not be calculated accurately using the model, due to the very low altitude of absorption, but it did indicate the electrons had a characteristic energy greater than 100keV. This fits with the theory of a daytime absorption spike, as they are thought to be due to electrons with very large energies.

Chapter 4

Daytime Absorption Spikes

This chapter investigates auroral absorption in the daytime sector. Data from IRIS at Kilpisjärvi was used to perform a 13 year statistical study of dayside absorption and secondly to study one year in greater detail. Secondary data was taken from LANL01A, LANL02A and ACE satellites; as well as ground based magnetometers and VLF observations.

4.1 Introduction

Auroral absorption as observed by riometers is primarily due to the precipitation of energetic electrons within the range of 10-100keV and can be attributed to numerous dynamic processes within the Earth's magnetosphere and solar wind. The observations of absorption follow a diurnal pattern that maximizes in the morning sector. Absorption in the dusk and night time sectors is predominately caused by the injection of electrons due to substorms, and substorm related phenomena, and has been comprehensively studied, such as *Hargreaves et al.* (1996); *Baker et al.* (1981); *Baker et al.* (1982). Absorption maximizes during the morning sector, with the major cause being the precipitation of Eastward drifting electrons from

substorm injections on the night side, *Hargreaves and Devlin* (1990), *Kavanagh et al.* (2002). During the afternoon sector absorption observed at auroral riometers decreases into a deep minimum. This is illustrated in figure 4.1; the absorption measurements from beam 25 of IRIS have been collated and the mean and median values for absorption during the course of a sidereal day are shown. Panel A. shows the median, with the interquartile range, while panel B. shows the mean with the 1st standard deviations. The median value is visibly lower than the mean values, indicating that the absorption is not normally distributed but includes absorption events of high intensity, which would account for this difference. It clearly shows a maximum in absorption in the morning sector values reaching 0.15 and 0.25 for the median and mean respectively. There is a deep minimum observed between 15-17UT which then steadily rises through the evening and night time sector (18-05UT).

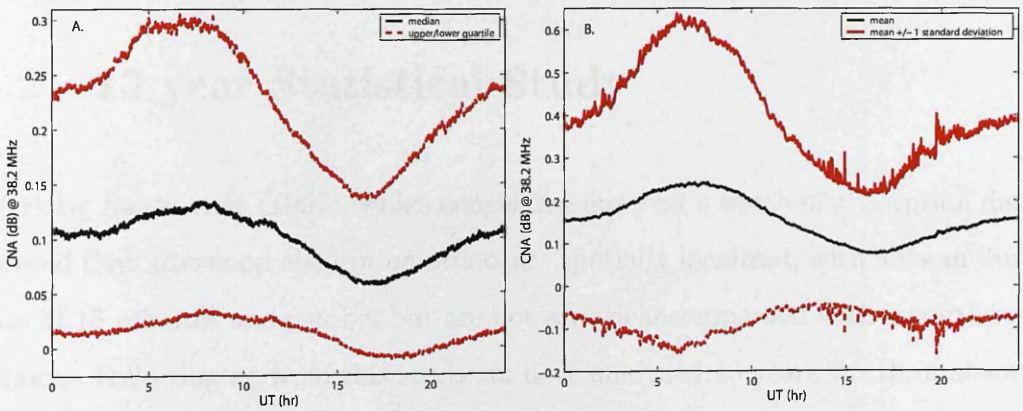

Figure 4.1: A. 1 minute averaged median values of auroral absorption in beam 25 of IRIS, with upper and lower quartiles. B. 1 minute averaged mean values of auroral absorption in beam 25 of IRIS, with +/- 1 standard deviation. Data was taken from a twelve year period between 1995 and 2006

Statistically, during the afternoon sector riometers see little absorption, however discrete cases of absorption do occur. At high latitudes in the polar cap and cusp regions, absorption spikes can occur, for example, due to 'inverted-V' structures (*Stauning and Rosenberg* (1996)) or magnetic impulse events (*Terkildsen et al.* (2001)). *Ranta et al.* (1997) observed localized absorption events that

occurred at auroral latitudes during the afternoon sector, and hypothesized that these were caused by precipitation of relativistically high energy electrons, in response to Pc1-2 waves. Pc 1-2 pulsations are generated by electromagnetic ion cyclotron instability at the equator. These waves are theoretically capable of scattering electrons of energies of 500keV and greater (*Meridth et al.* (2003); *Horne and Thorne* (1998)), and occur in the afternoon and evening sector. Observations of relativistic electron precipitation have been observed using VLF receivers (*Rodger et al.* (2008)) and X-ray detectors (*Millan et al.* (2002)).

Data from IRIS at Kilpisjärvi is used to perform a statistical analysis of absorption in the daytime sector, investigating the geomagnetic conditions. The absorption events of 2007 are studied in greater detail and 5 case studies from this year are shown.

4.2 13 year Statistical Study

Work by *Ranta et al.* (1997), which considered one year's worth of absorption data, showed that afternoon absorption events are spatially localized, with a mean duration of 15 minutes and can be, but are not always accompanied with a southward motion. Following on from this study we have analyzed 13 years worth of absorption data.

Detection of absorption events was automated; searching for peaks in the absorption data between 12-16UT which fell to the full width at half maximum point with in a two hour period. Data from beam 25 of IRIS at Kilpisjärvi was used to identify these absorption events. Days that include scintillation in beam 25 and time of polar cap of absorption are removed from the data set. From the 13 years 650 days were identified as having absorption events during the afternoon sector. 650 days of afternoon absorption accounts for 13.7% of days during this 13 year period and shows that the afternoon period is statistcally quiet but does

contain descrete events. Figure 4.2 shows the diurnal distribution of the events. 217 events, or 42.9% occur between 12UT and 13UT, with 22.7% occuring the next hour, 19.5% the following hour and finally 14.7% of events occuring in the final hour of interest. Of the 637 events, 35 have been identified as early onset substorms. These events display the negative deflections in the X-components of co-located magnetometers, which are associated with substorms. However these occur at times generally accepted as to be outside the 'normal' (18-05LT, ~16-03UT) local time period for substorm injections. (*Aminaei* (2007)). The earliest substorm events occur just before 14:00UT, with 2 events occurring around this time. The dirunal variation of the substorm events are indicated in figure 4.2 by the red bars.

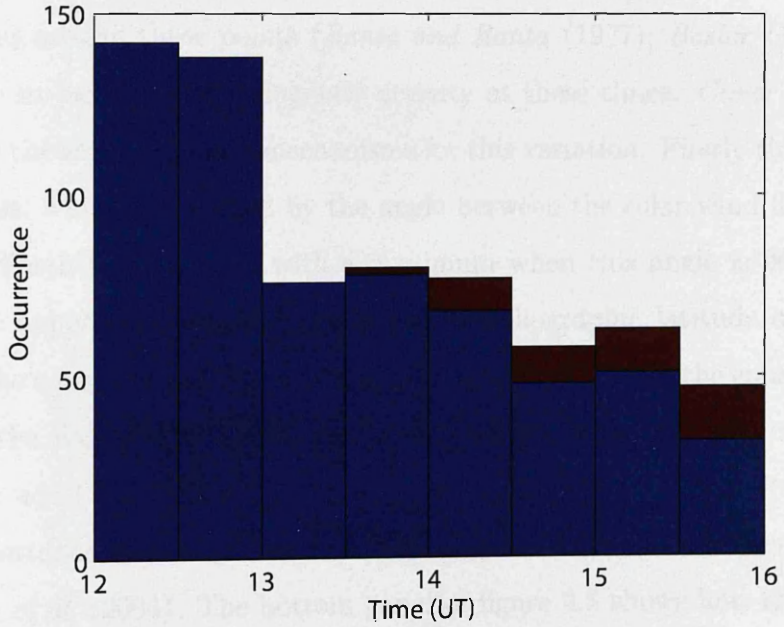

Figure 4.2: Diurnal variation of occurrence of daytime absorption spikes. Data is grouped into half hour bins. Red bars indicate the number of events that have been identified as early onset substorms.

The presence of these early onset substorms clearly are responsible for a part of the absorption observed during the afternoon sector, but do not fit the criteria of *Ranta et al.* (1997) and only make up 7.4% of the overall cases of absorption.

As these cases of afternoon absorption have been identified they are removed from further analysis. Figure 4.3 shows the diurnal, monthly and yearly variations of the afternoon absorption events. The top figure shows the dirunal variation of the absorption events with the substorm events removed. The overall trend is not altered with the removal of the substorm events. There is a peak in activity between 12-13UT, with activity levels steadily dropping during the course of the afternoon sector, reaching a minimum of just over 50 occurrences between 15:30-16:00UT. If you compare the pattern with that of the pattern seen in figure 4.1 the pattern is the same, indicating that this follows the general pattern of absorption seen during the course of a day. The seasonal variations are shown in the middle panel of figure 4.3. There is a maximum of events in March and September, around the equinox. This follows the general pattern of auroral absorption, which maximizes around these points (*Ranta and Ranta* (1977); *Basler* (1966)). This is due to an increase in geomagnetic activity at these times. *Cliver et al.* (2004) describes the three proposed mechanisms for this variation. Firstly the equinoctial hypothesis, which is governed by the angle between the solar wind flow direction and the Earth's dipole axis, with a maximum when this angle is 90^o. Secondly the axial hypothesis, which depends on the heliographic latitude of the Earth. During the equinoxes the Earth is at it's furtherest point from the equatorial plane. Thirdly the Russell-McPherron mechanism which states that magnetic fields in the solar wind have peaks in the southward component during the equinoxes. The importance of the contribution from each of these mechanisms is discussed in *Cliver et al.* (2004). The bottom panel of figure 4.3 shows how the number of daytime absorption events varies over the 13 years. The greatest number of events occur between 2003 and 2005; the declining phase of the solar cycle. *Russell* (1974) describe how the geomagnetic activity follows a 22 year cycle, but is offset so that it maximizes during the declining phase of the solar cycle, and is due to heliolatitude variation of the solar wind.

The maximum value of the absorption spikes are shown in figure 4.4. These are

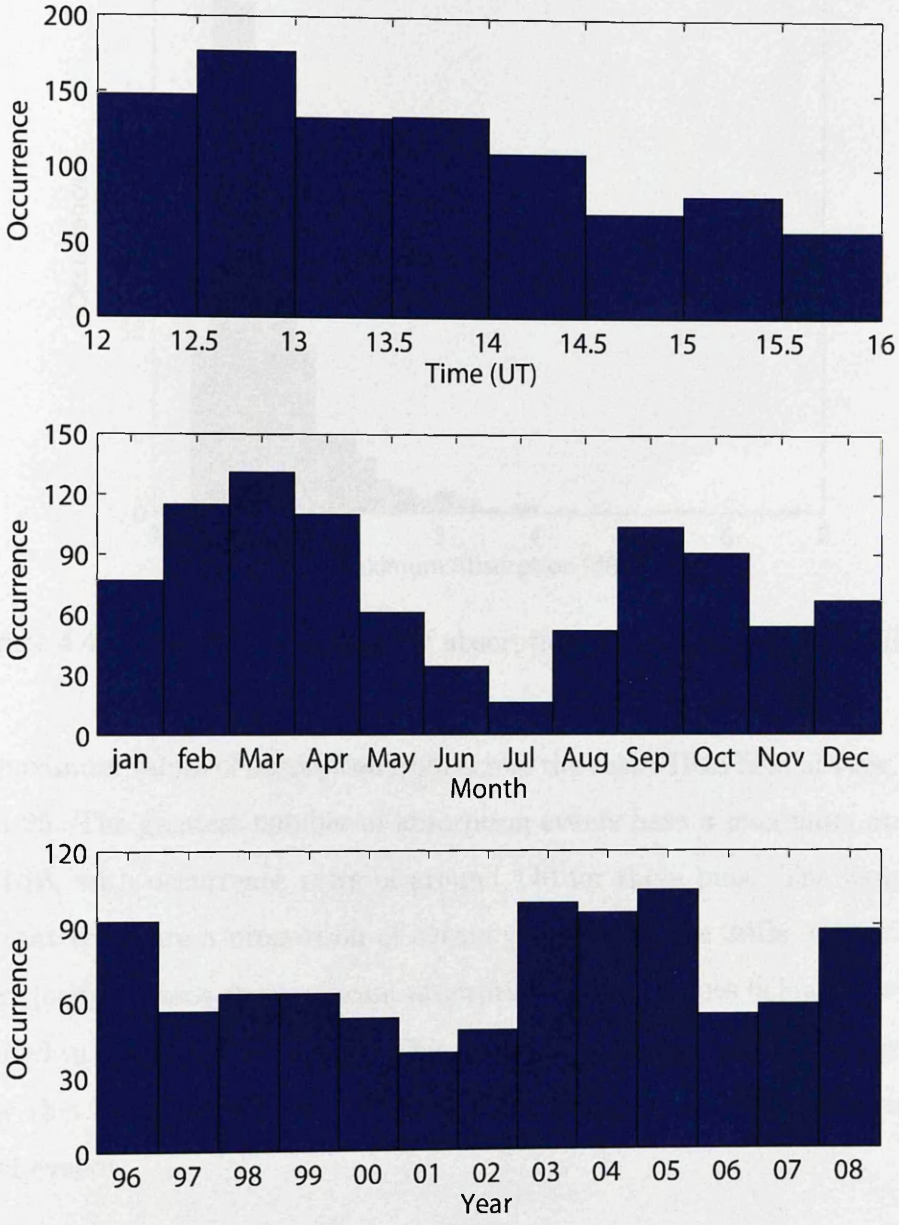

Figure 4.3: Top: Diurnal variation of occurrence of daytime absorption spikes, grouped into 30 minute bins. Middle: Occurrence of daytime absorption with respect to month. Bottom: Occurrence of daytime absorption with respect to year.

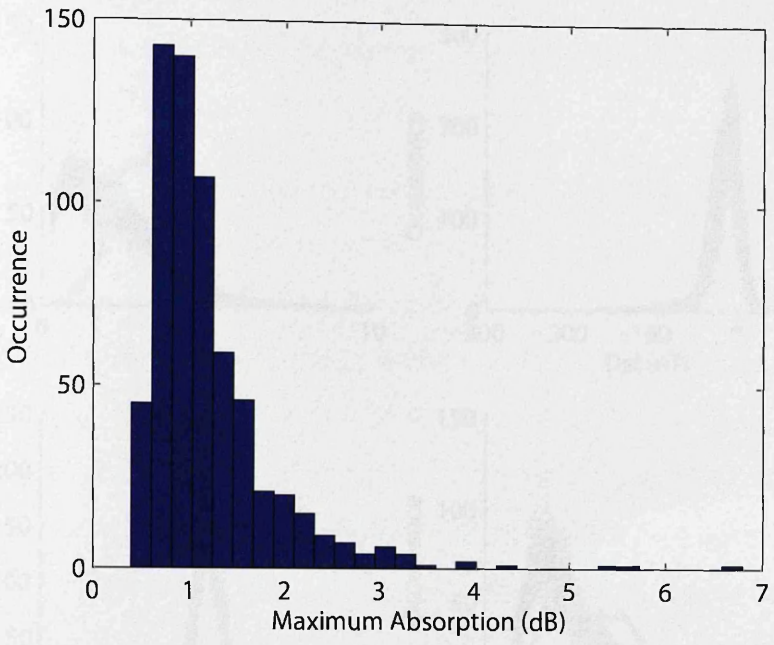

Figure 4.4: Maximum absorption of absorption spikes, grouped in 0.2dB bins.

the maximum values of absorption from across the entire IRIS field of view, not just beam 25. The greatest number of absorption events have a maximum absorption of ~1dB, with occurrence rates of around 140 for these bins. The figure shows also that there are a proportion of events greater that are 2dBs, indicating that the majority of these are significant absorption events. Values below 0.4 where not included in the selection process. This is due to the noise level of the instrument below this level makes it hard to distinguish between the instrument noise and actual events.

The corresponding solar wind parameters and magnetic indices with respect to the absorption events are shown in figure 4.5. The top two panels show the Kp and Dst indices with respect to the absorption events; with the bottom two panels showing IMF Bz and solar wind velocity. The black dashed lines on the figure represent 100 sets of 602 random time selections for this period, which give an understanding of the average conditions for this period. The Kp index indicates

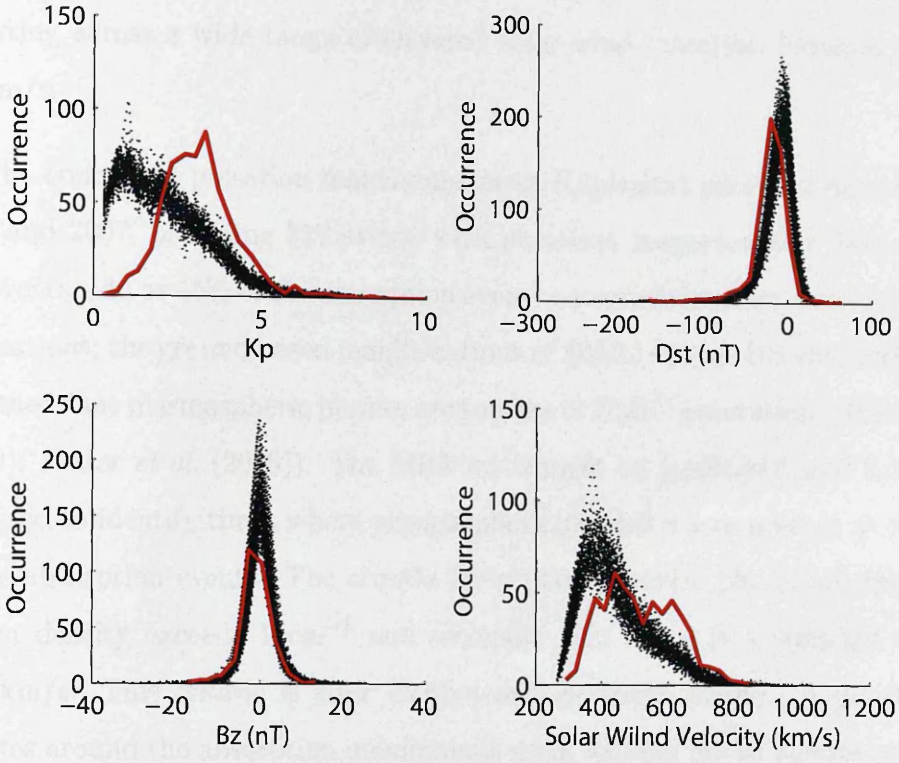

Figure 4.5: Red Line represents magnetic indices and solar wind parameters of daytime absorption spikes. Black lines represent a 100 set of 602 randomly selected times during the time period, to show the normal distributed pattern for each solar wind parameter and geomagnetic indices during this time period. Top Left: Kp values of absorption spikes. Top Right: Dst values of absorption spikes grouped in 20nT bins. Bottom Left: IMF Bz values binned in 20 nT bins. Bottom Right: Solar wind Velocity binned in 20km bins.

mild geomagnetic activity with regards to the absorption events, with most events occurring with a Kp value of ~3, above the average conditions for the time period. The occurrence rates for Dst are binned into 20nT groups, these values show little variation from average conditions, with most events occurring around -20nT, which would indicate very weak storm time conditions. The IMF Bz conditions show most absorption spikes differing only slightly from the average conditions; occurring with a slightly negative Bz value of ~-5nT, which may indicate some triggering process such as substorms. The solar wind velocity, along with the

Kp index shows the greatest variability from the average, with absorption events occurring across a wide range of elevated solar wind velocities between 400 and 800km/s.

The co-located pulsation magnetometer at Kilpisjärvi provided data between 2002 and 2007, providing 317 events with pulsation magnetometer data. Of the 317 events, 144 or 45% of the absorption events occurred simultaniously with Pc 1-2 pulsations; the ground based manifestations of EMIC waves. Recent studies have indictaed that plasmaspheric plumes are sources of EMIC generation (*Morley et al.* (2009); *Fraser et al.* (2005)). The MPA instrument on LANL01A and LANL02A was used to identify times where plasmaspheric plumes where present at the time of the absorption events. The criteria for a plasmaspheric plume are firstly, the proton density exceeds 10cm^{-3} and secondly, that there is a sunward velocity of 12km/s. This criteria is after *Denton and Borovsky* (2008). A period of 30 minutes around the absorption maximum is used, looking for 10 minutes of plume activity. 14.37% of the absorption events, occurred with at least ten minutes of plume activity, as seen from LANL01A or LANL02A.

4.2.1 Superposed Epoch Analysis

To better understand geomagnetic conditions around the time of these daytime absorption events, and not just at the exact time of the absorption event, a superposed epoch study was conducted. The zero epoch time was chosen as the beginning rise of absorption for the events. Figure 4.6 shows the superposed epoch analysis of the IRIS absorption data. The beam with greatest absorption was used for the analysis, with an hour before and after zero epoch shown. The standard deviation from the mean and the interquartile range from the median are both shown, as the standard deviation can be skewed by the presence of extreme outliers. However the mean and median values are similar, with a maximum absorption value of $\sim$ 0.8dB and 0.7dB respectively. The duration of the absorption

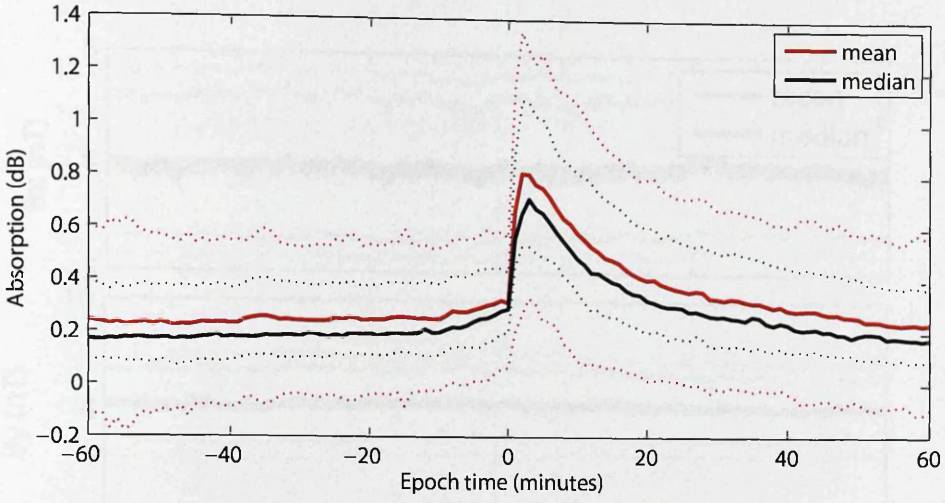

Figure 4.6: Superposed epoch analysis of absorption in IRIS of daytime absorption. Zero Epoch is the beginning of the daytime absorption events. Red dotted line is the first standard deviation point and the dotted black line is the upper and lower interquartile ranges.

events is around 20 minutes, which is in agreement with *Ranta et al.* (1997). The time to reach maximum absorption is very short, on the scale of a 1-3 minutes.

The superposed epoch analysis of the IMF, Bx, By and Bz parameters are shown in figure 4.7. This figure and the following superposed epoch figure show 24hrs before and after the zero epoch time. Again the mean and median values are shown in red and black respectively. Also shown are the first standard deviation points and the inter quartile range (red and black dotted line respectively). Like last time these measures of spread do not vary from one another greatly, indicating outliers are not skewing the values. Both the Bx and By plot (Top and middle panels respectively) show a constant 0nT level across the epoch time. The first standard deviation point and interquartile ranges are of the order of around 5nT. The bottom panel shows the Bz values, where a negative deflection is observed in the proceeding 4 hours before the zero epoch. This deflection however is very weak, with a magnitude of only -2nT. The interquartile range and standard deviation points are in the ranges of $\sim$3 and 4nT respectively.

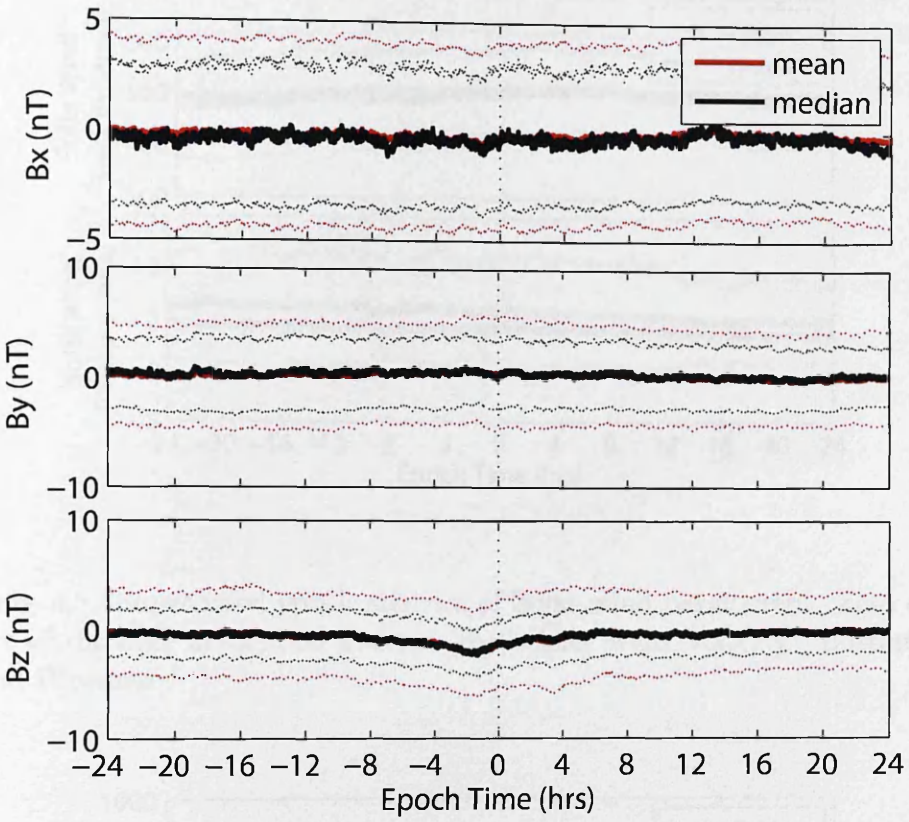

Figure 4.7: Superposed epoch of IMF magnetic field at the start of absorption event. Red lines represent mean +/- 1 standard deviation. Black lines represent median and upper and lower ranges. Zero epoch is start of daytime absorption events. Top: Bx. Middle: By. Bottom: Bz.

Figure 4.8 shows the superposed epoch analysis for solar wind velocity (top panel) and solar wind density (bottom panel). The solar wind velocity is constant across the 48 hours at 500km/s. The first standard deviation is ~100km/s and the interquartile range ~75km/s. The solar wind pressure is also constant throughout the 48 hour duration, steady at ~5nPa, with a standard deviation of around 5nPa and interquartile range of around 3nPa.

Superposed epoch analysis of the Ae and SYM-H magnetic indices, as shown

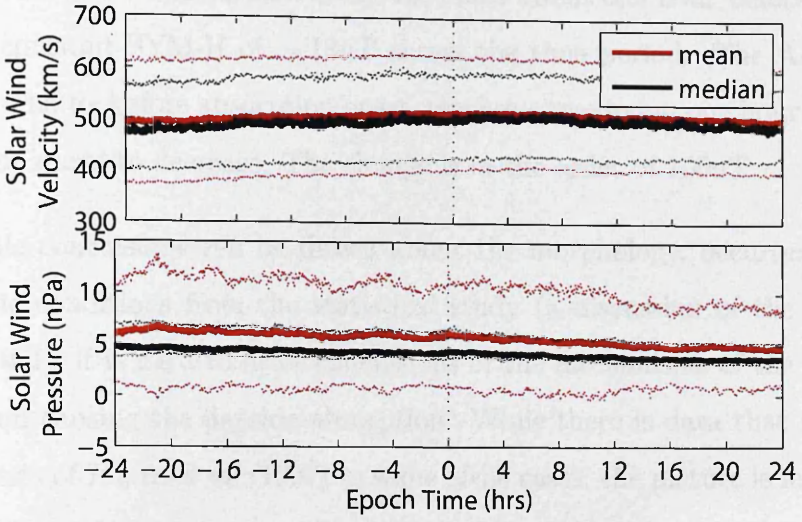

Figure 4.8: Superposed epoch analysis of Solar wind parameters. Zero epoch is start of daytime absorption events. Top: Solar wind Velocity. Bottom: Solar Wind Pressure.

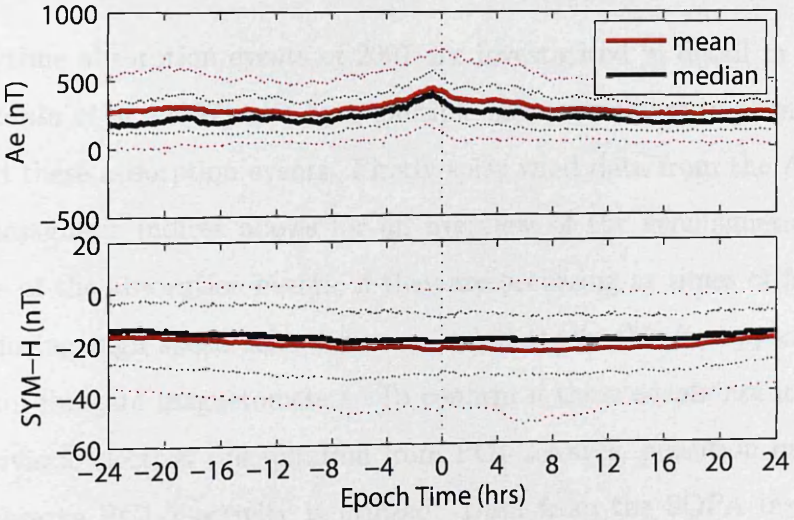

Figure 4.9: Superposed epoch Analysis of Magnetic indices. Zero epoch is start of daytime absorption events. Top: Ae index. Bottom: SYM-H index.

in figure 4.9 show a maximum in the Ae index about one hour before zero epoch, with a constant SYM-H of ~-18nT across the time period. The Ae index rises around 4 hours before absorption onset, reaches a maximum one hour before onset and then starts to decrease. The change is in the order of 100nT.

While conclusions can be drawn about the morphology, occurrence and geomagnetic conditions from the statistical study (a discussion of the results is in section 4.4), it is hard to draw conclusions of the mechanisms of the particle precipitation causing the dayside absorption. While there is data that supports the hypothesis of *Ranta et al.* (1997) in some ofthe cases, the picture is far from clear. A year from this study is considered in section 4.3, with each absorption event investigated in detail.

4.3 Daytime Absorption in 2007

The daytime absorption events of 2007 are investigated in detail in this section. Using *Ranta et al.* (1997) as a base multiple instruments are implemented to understand these absorption events. Firstly solar wind data from the ACE satellite and geomagnetic indices allows for an overview of the geomagnetic activity at the time of the absorption events, if they are occurring at times of intense activity, or during high speed solar streams. Additionally this is supplemented with data from fluxgate magnetometers. To confirm if these events are indeed caused by relativistic electron precipitation from PC1-2 waves, pulsation magnetometer which observe PC1-2 activity is utilized. Data from the SOPA instruments on the LANL01A and LANL02A provide electron flux data in the magnetosphere, showing the activity of the particle populations at the time of the event, allowing to understand if high energy or low energy precipitation is occurring. Finally some VLF data from the AARDVARK network is presented, which if the absorption is

caused by relativistic precipitation would show change in the received VLF signal strength.

Out of the 2007 dataset, only absorption events where LANL01A electron flux data was available were utilized. This left 33 days of afternoon absorption events. With respect to the hypothesis that afternoon absorption events are caused by relativistic electron dropout due to EMIC wave scattering, the events where categorized with respect to changes to the MeV signatures at geostationary orbit and the presence of Pc 1-2 waves. Of the 33 days, 17 events had no response to MeV particles at geostationary orbit, nor any Pc 1-2 activity observed by the Kilpisjärvi pulsation magnetometer. Four of the cases were found to coincide with an MeV response and Pc 1-2 activity, with two of these cases also including a low energy response at the same time. Thirdly there were 3 cases where a MeV response was seen in LANL01A and LANL02A but no Pc 1-2 activity was observed on the ground at Kilpisjärvi . Of these three cases one had a low energy response at the time of the absorption event. The final 8 cases no MeV response was observed but Pc 1-2 events were observed at the time of the absorption event.

A case study of each category is discussed, and they are as follows:

1. MeV response and Pc 1-2 activity: 25 October 2007
2. MeV response, Pc 1-2 activity and includes a low energy response: 25 August 2007
3. MeV response but no Pc 1-2 activity: 22 August 2007
4. No MeV response but Pc 1-2 activity: 7 February 2007
5. No MeV or Pc 1-2 activity: 22 December 2007

4.3.1 25 October 2007

On October 25 2007, at approximately 14:00UT an absorption spike was observed in beam 25 of IRIS. Panel A. of figure 4.10 shows the response as seen in beam 25. The event lasted for approximately 10 minutes with a peak absorption of 1dB. Image plots of the event are shown in panel B. From left to right the images are: 10 and 5 minutes before the peak, the peak and 5 and 10 minutes after the peak. The absorption event has a band like structure, that encompasses approximately half of the field view at it's maximum. Panel C and D show the H and D components of the pulsation magnetometer at Kilpisjärvi . A Pc 1-2 event was observed between approximately 12UT to 14:30UT.

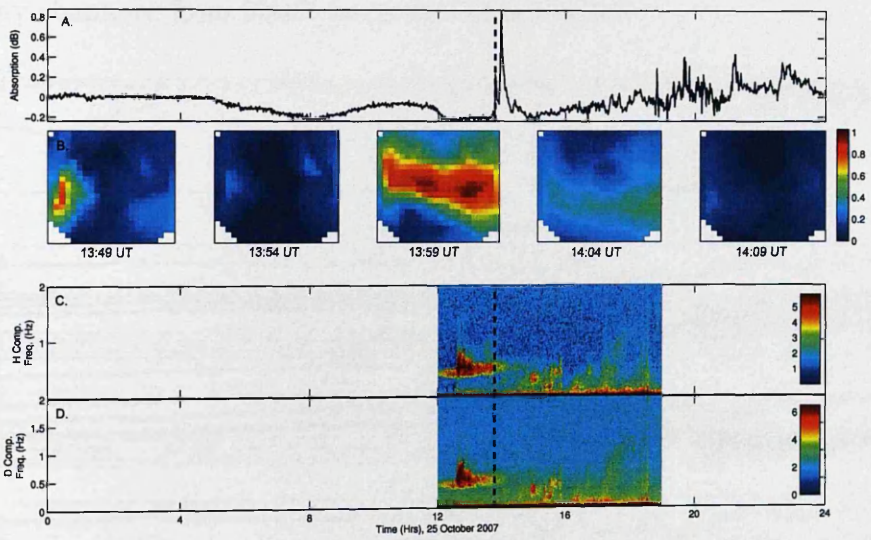

Figure 4.10: IRIS and pulsation magnetometer data at Kilpisjärvi , 25 October 2007. A: Beam 25 IRIS. B: Image plots of absorption data for duration of daytime absorption event. C: H component pulsation magnetometer data. D: D component pulsation magnetometer. Dotted line indicates the beginning of absorption event.

Observations of the electron fluxes from LANL01A and LANL02A are shown in figure 4.11. The top panel shows the integrated flux across the energy channels for LANL1A. Also shown is the Kennel-Petschek limit. This is the limit for stably trapped particles (*Kennel and Petschek* (1966)). The Kennel-Petschek limit gives

an estimate on the flux level required for particles trapped in the magnetosphere to precipitate into the atmosphere. While this treatment is for non-relativistic particles, it allows an estimate to see if the non relativistic electrons are capable of pitch angle scattering, when there is an injection of particles. If the limit is not reached then it may imply that it is not the low energy particle population that is being precipitated. The levels of integrated flux do not pass this limit during the time of the absorption event. The differential fluxes shown in the middle and bottom panels, show the electron flux levels for LANL01A and LANL02A respectively. At the start time of the absorption event, indicated by the vertical dotted line at 14:00UT, there is a substantial decrease in MeV electron channels. This is seen in both LANL satellites. This loss can be seen across the full range of energy channels, from 50keV to greater than 1.5MeV.

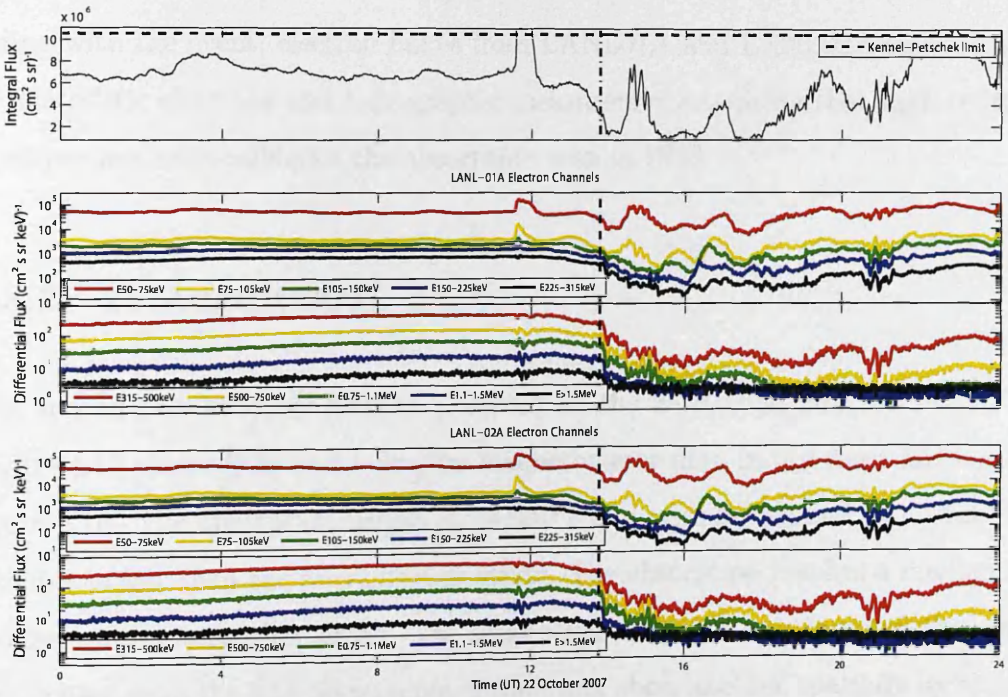

Figure 4.11: Electron fluxes for LANL01A and LANL02A, 25 October 2007. Top: Integrated flux LANL01A electron density with Kennel-Petschek limit marked. Middle: LANL01A differential electron channels Bottom: LANL02A electron Channels. Vertical dotted line indicates the beginning of absorption event.

Discussion of this event is also discussed in section 3.7.3 as a case study for

the tomographic calculation of height of absorption and characteristic energy. The solar wind conditions and magnetic activity for this event indicate that this is the beginning of a geomagnetic storm, as seen in the rise of the solar wind velocity, and characteristic signal in the SYM-H measurements. The tomographic estimations of the height of the absorption, places the height at around 70km. This altitude is far lower than the normal absorption height for 5-100keV electrons, indicating higher, relativistic energies.

With regards to the work by *Ranta et al.* (1997), this case study could be described as a typical *Ranta et al.* (1997) event. The absorption spike duration is in the order of minutes, with a spatial extent that is quite localized. There is a small positive deflection in the X-component of the Kilpisjärvi fluxgate magnetometer of ~100nT at the time of the absorption event. Pc 1-2 events are observed coinciding with the event, electron fluxes from LANL01A and LANL02A show losses of relativistic electrons and tomographic measurements indicate that high energy electrons are responsible for the absorption seen in IRIS.

4.3.2 25 August 2007

The second case study of interest occurred on the 25 August 2007 at 14:13UT. Figure 4.12 shows IRIS and pulsation magnetometer data in the same fashion as figure 4.10. The absorption begins at 14:00UT and lasts for around ~ 1 hour, 50 minutes longer than the previous case study. The absorption reaches a maximum around ten minutes after onset. The absorption images shown in panel B shows five images from the first 30 minutes of the event show another spatially localized event. PC 1-2 activity, as shown in panel C and D is present during the event, beginning at the onset of the absorption event and continuing throughout and after the event has ended, with the strongest signal occurring just after the start of the precipitation event.

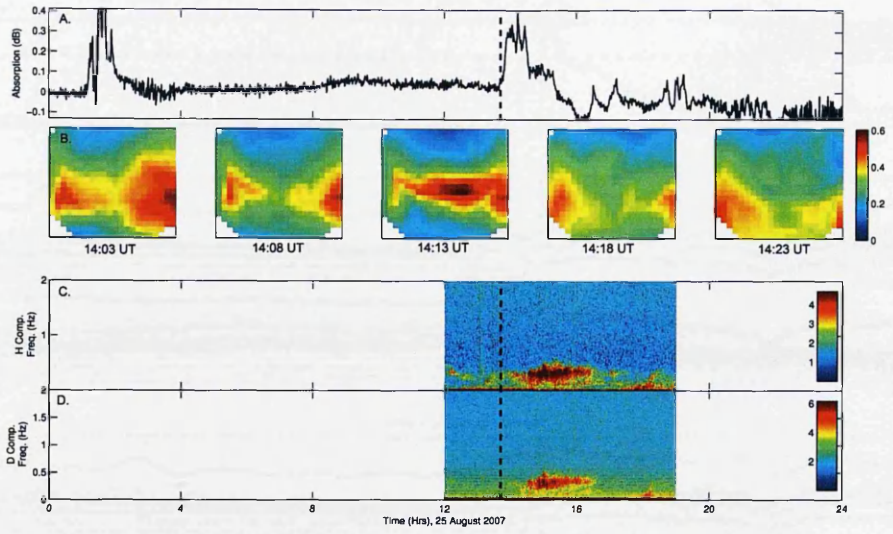

Figure 4.12: IRIS and pulsation magnetometer data at Kilpisjärvi , 25 August 2007. A: Beam 25 IRIS. B: Image plots of absorption data for duration of daytime absorption event. C: H component pulsation magnetometer data. D: D component pulsation magnetometer. Dotted line indicates the beginning of absorption event.

Observations of the electron fluxes are shown in figure 4.13 again in the same fashion of figure 4.11. Unlike the previous case study, there is a dispersed injection of low energy electrons, beginning at 12:00UT and maximizing at the same time as the absorption event. The integrated electron flux shows that it is slightly greater than the Kennel-Petschek limit at the time of the absorption event, being greater than this limit at onset and lasting for approximately an hour, before dropping below, implying that this event could be a response to low energy electrons. However in the high energy channels there is a decrease in high energy fluxes occurring at around the same time as the absorption event.

The solar wind conditions and magnetic indices are shown in figure 4.14. Panel A shows the IMF magnetic field Bz. Panel B, the solar wind velocity. Panel C the AE, AU and AL indices, and in panel D. the SYM-H index. Throughout the event the Bz index is variable throughout the day, changing from negative to positive, within the range of -7 to 10nT. The solar wind velocity is increasing from slow velocities of $\sim$ 300km/s, increasing during the event at 14:00UT and for the rest

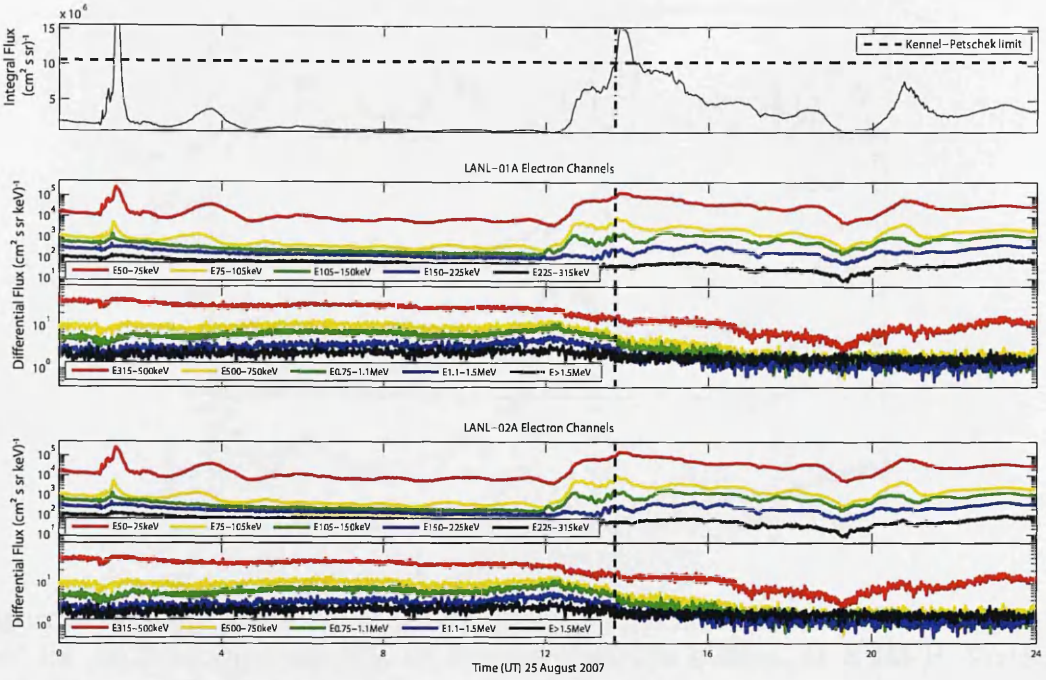

Figure 4.13: Electron fluxes for LANL01A and LANL02A, 25 August 2007. Top: Integrated flux LANL01A electron density with Kennel-Petschek limit marked. Middle: LANL01A differential electron channels Bottom: LANL02A electron Channels. Vertical dotted line indicates the beginning of absorption event.

of the day to $\sim$ 400km/s. The SYM-H index drops from 10nT at 12:00UT to negative values through the course of the absorption event minimizing at 20:00UT with a value of -15nT. This could indicate that this event, like the previous one occurred during the beginning of a geomagnetic storm. The AE index indicates that the absorption event occurred following a peak in auroral electrojet activity, at 12:00UT , with a value over 500nT.

As with the previous example there is a small positive deflection in the X-component of the Kilpisjärvi fluxgate magnetometer, as shown in the bottom panel of figure 4.15. The magnetometer rises from 0nT at 12:00UT to just over 80nT before the absorption event, and then decreases again to around 30nT at 16:00UT. The top panel of figure 4.15 shows data from the AARDDVARK VLF network. The data shown is of the signal strength of the NAA VLF transmitter, received at Sodankylä. This VLF path has the advantage that it passes through

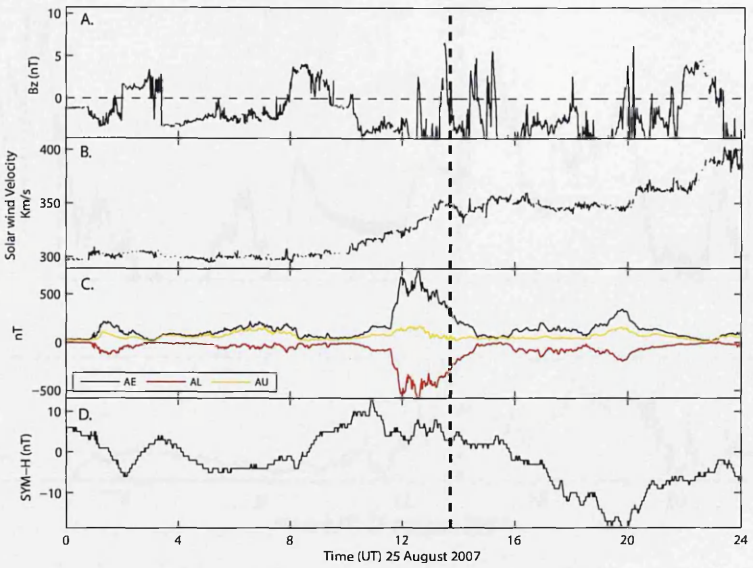

Figure 4.14: Solar wind and Magnetic Indices, 25 August 2007. A: IMF magnetic field Bz. B: Solar wind velocity. C: Auroral electrojet indices. D. SYM-H. Vertical dotted line represents beginning of absorption event.

the central beams of IRIS. Attenuation in the VLF signal indicates modulation of the ionosphere below 80km. The VLF plot shows an increase in the signal level during the absorption event, between 14:00UT and 16:00UT that could indicate relativistic electron precipitation at the time of the event.

4.3.3 22 August 2007

The absorption event on August 22 2007 occurs at 14:54 UT and has a duration of ~20 minutes, as can be seen in figure 4.16. The absorption event reaches a maximum of 1dB. The absorption images in panel B, however show that the absorption event begins earlier, and reaches a maximum in the southern corner of the IRIS field of view. At the time of the absorption event no Pc1-2 activity is seen in either the H or D components of the pulsation magnetometer, shown in panels C and D, however there is some activity that occurs after the event just before 16:00UT.

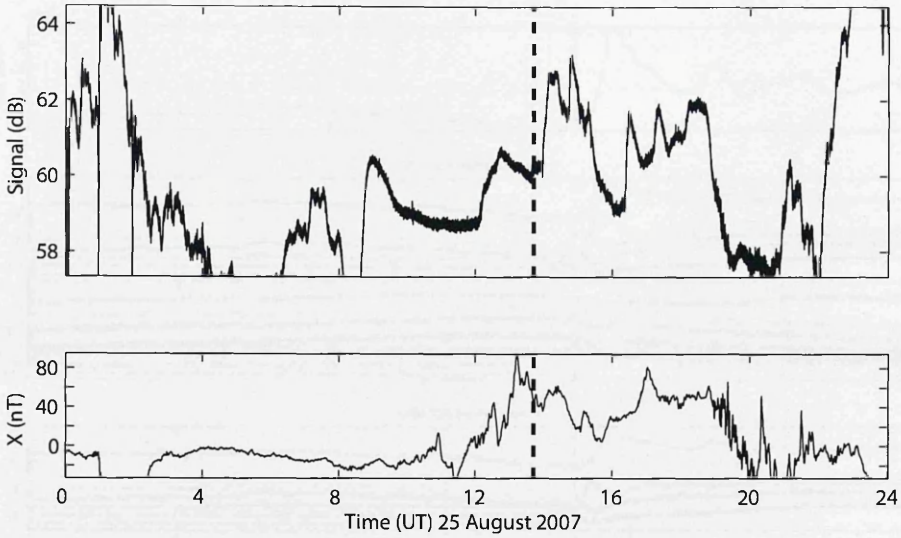

Figure 4.15: Top: VLF signal data from NAA transmitter received at Sodankyla Bottom: X-component IMAGE magnetometer at Kilpisjärvi . Daily mean has been removed. Vertical dotted line represents beginning of absorption event. 25 August 2007

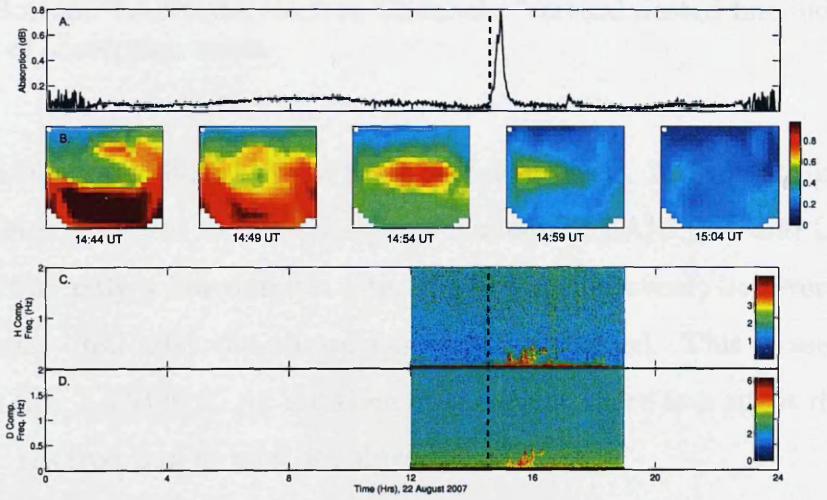

Figure 4.16: IRIS and pulsation magnetometer data at Kilpisjärvi , 22 August 2007. A: Beam 25 IRIS. B: Image plots of absorption data for duration of daytime absorption event. C: H component pulsation magnetometer data. D: D component pulsation magnetometer. Dotted line indicates the beginning of absorption event.

The Kennel-Petschek is not reached by the integrated flux of LANL01A, this is demonstrated by the fact that the limit is not seen on the top panel of figure

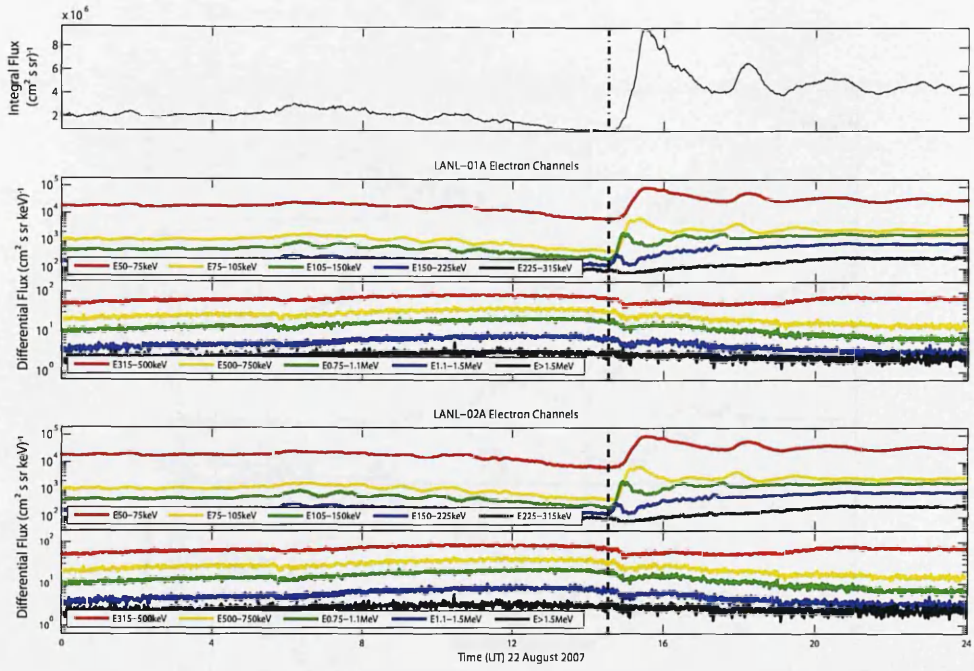

Figure 4.17: Electron fluxes for LANL01A and LANL02A, 22 August 2007. Top: Integrated flux LANL01A electron density. Middle: LANL01A differential electron channels Bottom: LANL02A electron Channels. Vertical dotted line indicates the beginning of absorption event.

4.17 as the integrated flux does not reach sufficient levels. A dispersed injection is observed after the event in the low energy channels of LANL01A and LANL02A, seen occurring only a few minutes after the absorption event, however this does not maximize until after the absorption event has passed. This is seen in both LANL01A and LANL02A. At the time of the event there is a slight decrease in relativistic electron flux in both satellites.

The solar wind conditions and magnetic indices are shown in figure 4.18. The absorption event occurs during a sustained but weak negative Bz, shown in panel A. Between 08:00UT and 18:00UT Bz fluxuates between 0 and -2nT. The AE index between 08:00Ut and 20:00UT, seen in Panel C is elevated at around 200nT, indicating mild auroral activity throughout this period. The solar wind velocity in panel B is steady around between 310km/s and 340km/s, indicating that this event occurred during a period of slow solar wind velocity, so did not occur during a

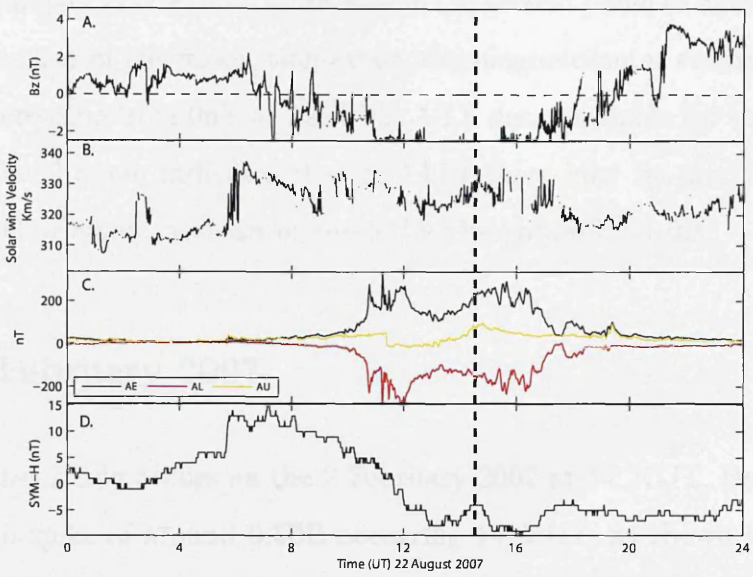

Figure 4.18: Solar wind and Magnetic Indices, 22 August 2007. A: IMF magnetic field Bz. B: Solar wind velocity. C: Auroral electrojet indices. D. SYM-H. Vertical dotted line represents beginning of absorption event.

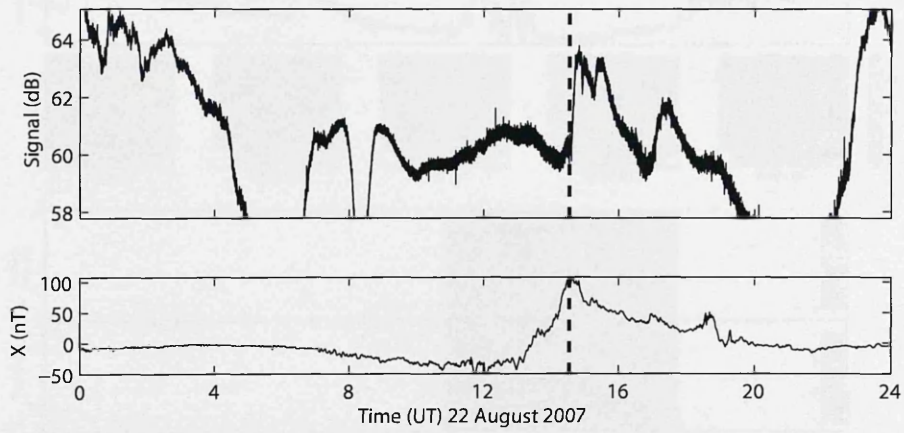

Figure 4.19: Top: VLF signal data from NAA transmitter received at Sodankyla Bottom: X-component IMAGE magnetometer at Kilpisjärvi . Daily mean has been removed. 22 August 2007

geomagnetic storm. Panel D shows he SYM-H values At the time of the absorption there is negative deflection of -5nT, which had decreased from 10nT at 08:00UT. These values indicate that this event occurred during weak geomagnetic activity.

Like the previous two case studies there is a small positive deflection of the X-component fluxgate magnetic field, as seen in the second panel of figure 4.19 At the 14:54UT, the time of the absorption event, the magnetometer reading maximizes ad 100nT, increasing from 0nT at 12:30UT. VLF data available for this day shown in the first panel again indicates that at 14:54 there may be modulation of the ionosphere below 80km, with an increase the absorption by 4 dB.

4.3.4 7 February 2007

The fourth case study occurs on the 7 February 2007 at 14:27UT. Beam 25 shows an absorption spike of around 0.5dB occurring 14:20UT, as shown in panel A of figure 4.20. This is proceeded by 2 hours of absorption events of a similar magnitude. Like the previous case studies this absorption event is localized spatially as

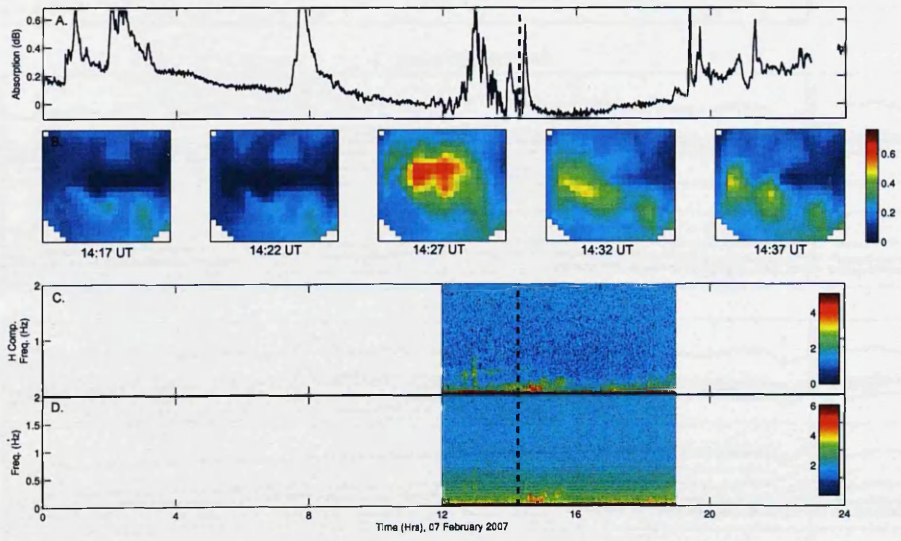

Figure 4.20: IRIS and pulsation magnetometer data at Kilpisjärvi , 7 February 2007. A: Beam 25 IRIS. B: Image plots of absorption data for duration of daytime absorption event. C: H component pulsation magnetometer data. D: D component pulsation magnetometer. Dotted line indicates the beginning of absorption event.

shown in the image plots of panel B. The highest absorption is seen in the third absorption image at 14:27UT. The event is localized to the center of the field of

view. The absorption event has a duration of less than an hour. Pc1-2 activity is observed in the Kilpisjärvi pulsation magnetometer at the time of the absorption event, as shown in panels C and D of figure 4.20.

However unlike the previous case study events, that show an MeV electron response at geostationary orbit, there is no MeV response seen in the two LANL satellites (figure 4.21). What is observed in both satellites is a dispersed injection that maximizes at the time of the absorption event. There are numerous dispersed injections seen in the low energy electron channels (50-150keV), one at 07:00UT, 11:00UT and at the time of the absorption event at 14:00UT. The integrated flux is constantly above the Kennel-Petschek limit for trapped radiation between 07:00UT and 16:00UT.

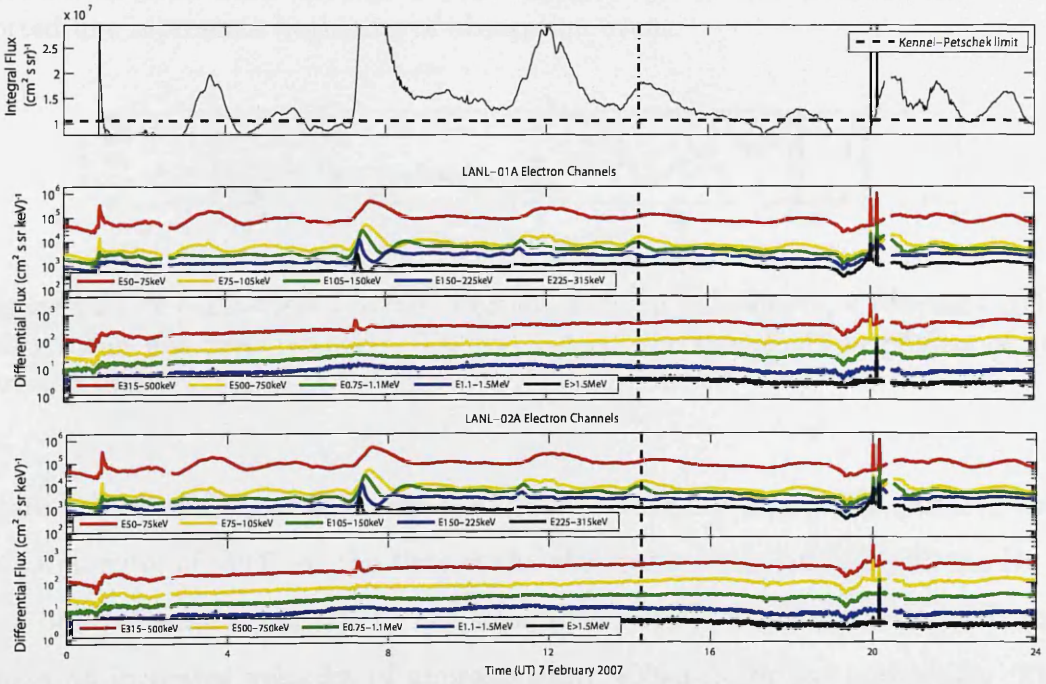

Figure 4.21: Electron fluxes for LANL01A and LANL02A, 7 February 2007. Top: Integrated flux LANL01A electron density with Kennel-Petschek limit marked. Middle: LANL01A differential electron channels Bottom: LANL02A electron Channels. Vertical dotted line indicates the beginning of absorption event.

The solar wind conditions at the time of this absorption event are shown in

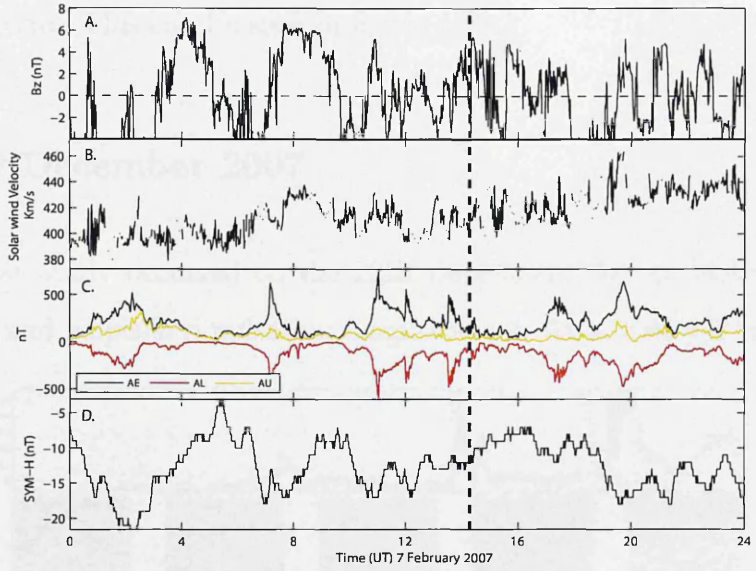

Figure 4.22: Solar wind and Magnetic Indices, 22 August 2007. A: IMF magnetic field Bz. B: Solar wind velocity. C: Auroral electrojet indices. D. SYM-H. Vertical dotted line represents beginning of absorption event.

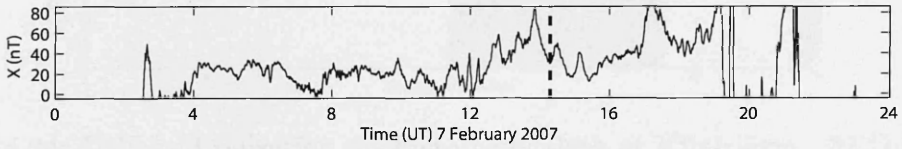

Figure 4.23: X-component IMAGE magnetometer at Kilpisjärvi , 7 February 2007. Daily mean has been removed. Vertical dotted line represents beginning of absorption event.

figure 4.22. Panel A shows a very variable Bz, changing between at positive 6nT to a minimum of -3nT. At the time of the absorption event at 14:00UT the Bz is in a positive state around 4nT. The solar wind velocity is shown in panel B and shows an increased velocity, of approximately 400km/s for the entire day. The auroral electrojet values are shown in panel C. The absorption event takes place at the end of three spikes in auroral electrojet indices. The SYM-H index shows a sustained negative value between -5nT and -20nT for the entire day. The X-component of the fluxgate magnetometer shows a small positive deflection just before the absorption event of 80nT at 13:30UT, just over 30 minutes before the

absorption event. This can be seen in figure 4.23.

4.3.5 22 December 2007

The final case study occurred on the 22th December 2007 at 14.49UT. IRIS riometer data and Kilpisjärvi pulsation magnetometer data is shown in figure 4.24.

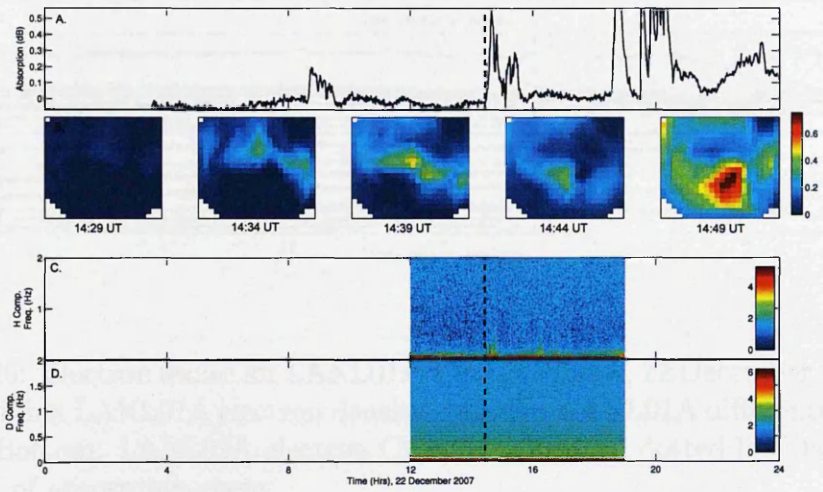

Figure 4.24: IRIS and pulsation magnetometer data at Kilpisjärvi , 22 December 2007. A: Beam 25 IRIS. B: Image plots of absorption data for duration of daytime absorption event. C: H component pulsation magnetometer data. D: D component pulsation magnetometer. Dotted line indicates the beginning of absorption event.

The event is the most localized of the 5 events and has a duration of approximately 30 minutes. The absorption event, seen from beam 25 of IRIS is shown in panel A. The event begins at 14:30UT and peaks 20 minutes later at 0.5dB. The absorption images shown in panel B between 14:29UT and 14:49 show a very localized event, occurring in the center of the field of view. The H and D component of the pulsation magnetometer shown in panels C and D show no Pc 1-2 activity at the time of the absorption event.

At the time of the absorption event the low energy electron fluxes in LANL01A and LANL02A show a dispersed injection which maximizes at the time of the

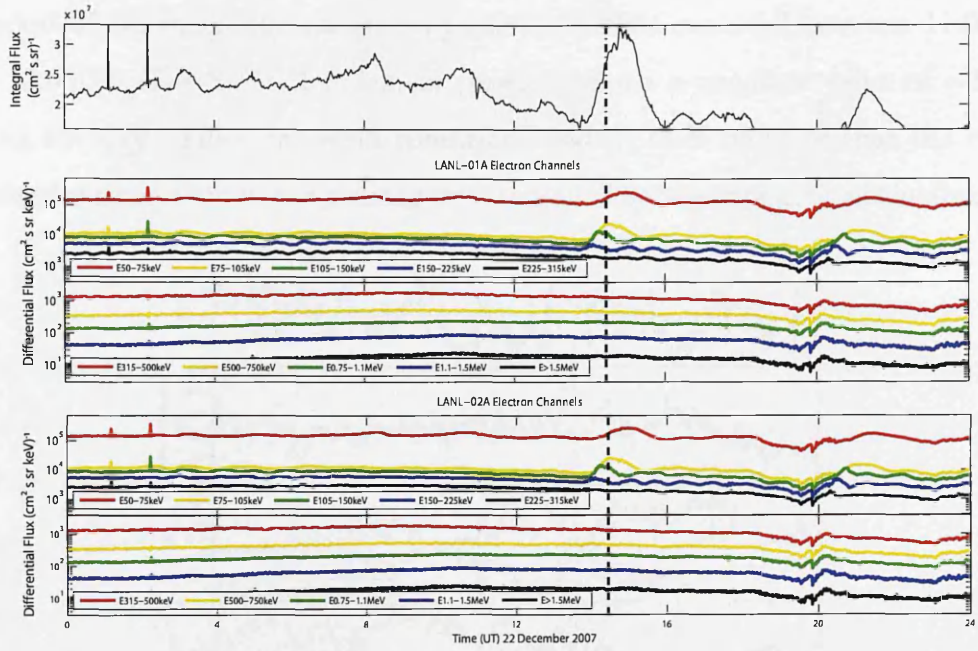

Figure 4.25: Electron fluxes for LANL01A and LANL02A, 22 December 2007. Top: Integrated flux LANL01A electron density. Middle: LANL01A differential electron channels Bottom: LANL02A electron Channels. Vertical dotted line indicates the beginning of absorption event.

absorption event as can be seen in bottom 4 panels of figure 4.25. The injection begins around 14:00UT and maximizes after the start of the absorption event at 14:50UT. There is no MeV response at either satellite, with the fluxes of energies greater than 225keV remaining constant during the course of the event. The integrated flux shows that it is greater than the Kennel-Petschek limit for the entire day.

Solar wind conditions and geomagnetic indices are shown in figure 4.26. Panel A shows that during the course of the absorption event the IMF Bz was changing between positive (4 nT) and negative (-2nT) Bz. At the time of the absorption event the IMF Bz was slightly positive, at 1 nT. The solar wind velocity, shown in panel B was constant at a high 600km/s for the course of the event and day. The AE index shown in panel C, indicates the absorption event occurred after

a period of enhanced auroral electrojet activity that occurred between 11:00UT and 13:00UT. The SYM-H index, in panel D shows a negative value of ~15nT during the day. The solar wind conditions and SYM-H indicate that the event occurred during a moderate geomagnetic storm. The x-component of the fluxgate

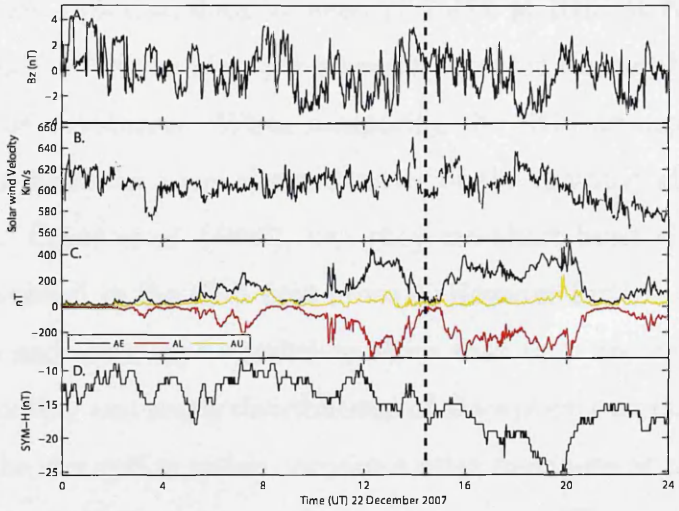

Figure 4.26: Solar wind and Magnetic Indices, 22 December 2007. A: IMF magnetic field Bz. B: Solar wind velocity. C: Auroral electrojet indices. D. SYM-H. Vertical dotted line represents beginning of absorption event.

magnetometer for this event, shows a very slight increase in intensity, ~20nT just prior to the absorption event. This can be seen in figure 4.27.

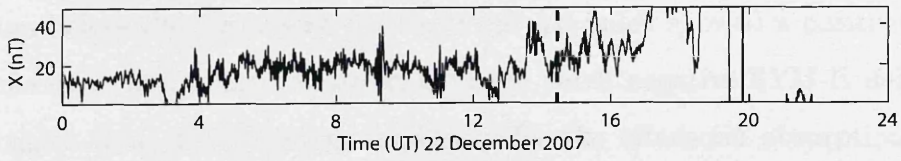

Figure 4.27: X-component IMAGE magnetometer at Kilpisjärvi , 22 December 2007. Daily mean has been removed. Vertical dotted line represents beginning of absorption event.

4.4 Discussion and Conclusions

The last two sections show the results from a 12 year statistical study of daytime absorption events and the analysis of one years worth of data from the study. The 12 year study looked at data between 12-16UT at IRIS at Kilpisjärvi . The study found that 7.4% of the absorption events observed during this period where infact early onset substorms. When comparing the IRIS absorption data these substorm onsets have the same characteristics of the daytime absorption spikes as described by *Ranta et al.* (1997), i.e. they are short lived ~20 minutes and are spatially localized to the IRIS field of view. However further analysis of local magnetometers and solar wind conditions show that they are indeed substorms. The diurnal, monthly and yearly distributions of absorption events, shown in figure 4.3 show that the absorption spikes occurance rates maximise at the same time as the generally accepted times for maximum absorption. The major pertubations of solar wind parameters and magnetic indices are the solar wind velocity and Kp index.

To understand the prevailing conditions; before, during and after the absorption events a superposed epoch study was conducted. Solar wind velocities across the events was constant at 500km/s (figure 4.8). IMF Bz showed a small negative deflection before the zero epoch time and the AE index showed a positive deflection before the zero epoch. Coupled with the small negative SYM-H deflection, they suggest that the prevailing conditions for the afternoon absorption events are during high speed solar wind velocity, during weak magnetic storms. The AE index indicates that the absorption events occur after a period of substorm injections; which indicates that the events be both the precipitation of drifting electrons and also could be relativistic electron precipitation, as EMIC waves require a source of protons; which would be gained by the substorm injections on the nightside. To further investigate the credence that the absorption events were the result of precipitation by EMIC waves, Pc 1-2 data from the collocated pul-

sation magnetometer was used to look for signatures occurring at the same time as the absorption events. During the 7 year period where data was available 45% occurred with accompanying Pc 1-2 events. Supplementary to this the occurrance of plasmaspheric plumes at the time of the absorption events was investigated, as plasmaspheric plumes are associated with EMIC generation. Of the available data, $\sim$ 13% of the absorption events had a plamaspheric plume occurring at the same time as observed by LANL01A and LANL02A. This is an indication that some of the events may be caused by EMIC scattering but perhaps other processes account for some of the events. Superposed analysis of the spikes themselves shows an average lifetime of 20 minutes, and an average absorption value of 0.8 dB (figure 4.6). These results are in line with the previous study of *Ranta et al.* (1997).

The statistical analysis showed the prevailing conditions for the daytime absorption events without defining the processes and mechanism responsible for the precipitation events. Preliminary evidence supports *Ranta et al.* (1997) in certain cases. The further analysis of daytime absorption events from 2007 was undertaken to try better define the precipitation mechanisms. Using electron flux data from the LANL01A and LANL02A satellites and pulsation magnetometer data 5 different responses in the electron fluxes and pulsation magnetometer were observed. Firstly the MeV flux dropout, with corresponding Pc 1-2 signature in the pulsation magnetometer. Secondly an MeV response and low energy dispersed injection that occurred with a Pc1-2 signature. Thirdly an MeV response without a Pc 1-2 signature, fourthly no MeV response with Pc 1-2 response and finally no MeV response and no Pc 1-2 signature. Comparisons of the ground based signatures of these absorption events show little difference between the five events, indicating that the prevailing conditions for each event is similar. Figures 4.10, 4.12, 4.16, 4.20 and 4.24 show the response to the absorption events in IRIS. Each absorption event has a duration between 15 minutes and an hour, and is a spatially localized, never filling the IRIS field of view. Of the five events the most localized absorption event is the event that has no MeV response or Pc 1-2 signature. Each

case study shows a small positive deflection in the X-component of the fluxgate magnetometer (seen in figures 3.23, 4.15, 4.19, 4.23 and 4.27).

For the three events that occur with an MeV response, (Figures: 3.23, 4.15, 4.19) the deflection is between 60-100nT and occurs at the same time as the absorption event. For the two events that do not see a MeV response at the time of the absorption event the deflection is smaller, ~40nT, with the maximum occurring before the absorption event occurs. Each event has similar SYM-H characteristics (figures: 3.27, 4.14, 4.18, 4.22, 4.26) with a small ~-5nT deflection, apart from 25 August 2007, which has a positive SYM-H value of ~ 5nT, which may indicate that the majority of the events occur during geomagnetic storms to some degree. All absorption events occur after an increase in AE activity, which may indicate that the events are dayside responses to substorms that has occurred earlier on the night side. This is apart from the absorption event that occurred on 25 October where the absorption events occurs at a time of peak AE activity (figure 3.27),

While the ground based instruments place events in similar regime of geomagnetic activity, the satellite observations of the five case study events show more variation between events, indicating different particle energies are responsible for the absorption (figures 3.28 4.14, 4.18, 4.22, 4.26). The solar wind velocity for two of the three events that show MeV response in electron fluxes, 25 October 2007 (figure 3.31) and August 25 (figure 4.18) show the solar wind velocities increasing from slow solar wind conditions to high solar wind speeds. These two events seem to be at the beginning of two mild geomagnetic storms. The third event that has an MeV response, August22nd 2007 occurred during the a period of slow slow wind velocity, ~300km/s. The two events that show no MeV responses occur at periods of high solar wind velocity, 400km/s and 600km/s. There does not seem to be coherent pattern to the events that have MeV response and those that do not.

The only major differences between the spike events that can be deduced using the current data sets is in the LANL01A and LANL02A electron flux data. For 25 October 2007, there is a sudden decrease in the electron fluxes across all the electron channels, making it hard to deduce if the response in IRIS is due to the lower energy or high energy counterparts. However the tomographic technique of chapter 3, indicates that this IRIS response is to relativistic electron precipitation. The second most convincing case of relativistic precipitation is the 22nd August 2007, at the time absorption event there is a decrease in MeV fluxes at LANL01A and LANL02A. For this case VLF data shows a perturbation in the signal strength which could indicate highly energetic electrons, (figure 4.19). The 25th August shows both an decrease in MeV electrons at the time of the absorption event but also a dispersed injection of low energy electrons, making a firm conclusion about the absorption type hard, however, again VLF data (figure 4.15) shows a perturbation that could indicate very high energy precipitating electrons. Without modeling the electron density from the VLF data it is not a certainty. The final two events, 7 February 2007 and 22 December 2007 show no MeV response and a dispersed injection at the time of the absorption spike, (figures 4.21 and 4.25). It is reasonable to conclude that these events are signatures of precipitation of drifting electrons, which is further reinforced from the time of the absorption spike with a maximum in AE values. From the ground based measurements these two events are almost identical to the other 3 events but are not related to relativistic electron precipitation. Of the 2007 events only 6 events had an MeV response. The rest showed no response in the MeV electron fluxes, and are most likely cases of 'morning' absorption that are occurring in the afternoon sector.

In conclusion, we have identified that there are numerous different mechanisms for the precipitation of electron during daytime absorption events. Firstly, early onset substorms which accounted for 7.4% of all events during the 13 statistical study. Secondly extension of morning absorption; that is the precipitation of drifting electrons from nightime substorm injections. Thirdly there is also strong

evidence for relativistic electron precipitation events, however it is inconclusive of which events definatley fall into this category. The situation is complicated by ground based measurements being similar for this and drift electron precipitation. Evidence indicates that Pc 1-2 waves can be present for both types of event, and be absent as well, with no differentiation between fluxgate magnetometer mearuements of either type.

Chapter 5

Conclusions and Future Work

This thesis has investigated the dynamic nature of electron precipitation from the point of view of observations of cosmic noise absorption by imaging riometers. Chapter 4 describes 2 new methods of calculating the height of cosmic noise absorption from two imaging riometers with overlapping fields of view. Firstly, through a height triangulation method and secondly through tomographic reconstruction of the 3D absorption structure. These methods were compared to the previously published methods of *Terkildsen et al.* (2004) and found to be an improvement over the previous method. Estimates of the characteristic energies for three case studies was carried out. The input factors controlling the characteristic energies were also investigated, showing that the greatest effect was due to the time of year, second only to the choice of flux spectrum. The three case studies, a substorm spike, a morning drift event and an afternoon absorption spike were found to have characteristic energies of 5keV, 17-20keV and greater than 100keV respectively.

Chapter 5 investigated daytime absorption spikes between 12-16UT in IRIS at Kilpisjärvi . A 13 year statistical study was carried out, as well as a detailed investigation of the daytime absorption spikes of 2007. 7.4% of these absorption events were early onset substorms. These events occurred between 14-16UT. The

statistical study of the remaining events showed that the daytime absorption events have a duration ranging from a few minutes to an hour, with an average duration of 20 minutes. They occur predominatley during mildly negative SYM-H, and at high solar wind indicating weak geomagnetic storms and after peaks in the AE index, indicating they occur around 30 minutes after substorm onsets. On investigation of 5 case studies, two were found to have strong evidence that suggests that these events are the result of reltavistic precipitation events. A third event showed signs of dropouts of high energy electron fluxes at geostationary orbit but at the same time as a dispersed injection With the current data it is impossible to determine what energy electrons are causing this precipitation event, however ther eis evidence to suggeest that it is reltavistic electrons. The final two cases show no response in the high energy electron flux channels but a dispersed injection of lower energy elctrons. For these cases it seems the absorption is caused by precipitation of these lower energy electrons. Of the daytime absorption cases this seems to be the major cause of daytime absorption events, with subtorm spikes and reltavistic electrons contributing to afternoon absorption events to a lesser extent.

5.0.1 Future Work

Unfortunately ARIES was decommissioned in August 2008. However this does not mean there is not scope for further work using the tomographic reconstruction. The process will work for any riometer systems that have overlapping fields of view. For example an 8x8 filled array Imaging riometer began operating at Ny-Ålesund, Svalbard, that has a large percentage of its beams overlapping with an already established imaging riometer at Longyearbyen, Svalbard. These two riometers would bring new absorption events to perform the tomographic reconstruction on as they are located at a higher latitude than IRIS and ARIES, allowing measurements of polar cusp events. Improvements to the reconstruction methods could be made including using tessellation for the rays, simplifying calculations. Secondly

a reconstruction method that disallows negative values may lead to better reconstruction results. Using a maximum entropy method for example could increase accuracy and lead to better results. If the accuracy was increased direct inversion of the electron density, using equation 1.45 could be performed. Direct inversion to the flux spectrum might even be possible. Every step though Absorption-Electron Density-flux spectrum, adds unknown parameters, uncertainties, and decreases the accuracy of the result. Ideally a system of multiple overlapping riometers would be deployed, in a fashion similar to the ALIS tomography work for visible auroras *Steen et al.* (1997). However this would be most likely be unfeasible due to the expense and space requirements for so many imaging riometer systems.

There are many avenues for future work from the work discussed in chapter 5. Firstly the statistical analysis could be extended to include superposed epoch analysis of absorption events that coincide with plamsaspheric plumes only, and analysis of events that occur at the same time as PC 1-2 waves to look for differences in the solar wind and geomagnetic conditions for these cases. Secondly the VLF data from the AARDDVARK network be best utilized if profiles of the electron density could be created for the case study events, using modeling techniques involving the long wave propagation code, and assumed electron spectra. NASA's radiation belt storm probes, due for launch in 2012 will be excellently placed to observe the energies of the precipitating electrons causing the absorption seen in IRIS and the still debated loss mechanisms that are responsible for the electron precipitation.

References

Akasofu, S. [1964] The development of the auroral substorm. *Planetary and Space Science*, 12 (4), 273-282.

Aminaei, A. [2007] *Characteristics of Night Time Absorption Spike Events as Signatures of Magnetosphere Ionosphere (M-I) Coupling. PhD thesis.* Ph.D. thesis, Lancaster University.

Aminaei, A., F. Honary, A. J. Kavanagh, E. Spanswick and A. Viljanen [2006] Characteristics of night-time absorption spike events. *Annales Geophysicae - Atmospheres, Hydrospheres and Space Sciences*, 24(7):1887–1904.

Araki, T., K. Schlegel and H. Luhr [1989] Geomagnetic effects of the hall and pedersen current flowing in the auroral ionosphere. *Journal of Geophysical Research*, 94(A12), 17185-17199.

Arnoldy, R. L. and K. W. Chan [1969] Particle substorms observed at the geostationary orbit. *Journal of Geophysical Research - Space Physics*, 74(21):50195028.

Ashrafi, M. and M. Kosch [2004] Height triangulation of artificial optical emissions in the f-layer. In *31st Annual European Meeting on Atmospheric Studies by Optical Methods, and 1st International Riometer Workshop, 22-28 August 2004.*

Aster, R., B. Borchers and H. Clifford [2005] *Parameter Estimation and Inverse Problems.* Elsevier Academic Press.

Axford, W. and C. Hines [1961] A unifying theory of high-latitude geophysical phenomena and geomagnetic storms. *Canadian Journal of Physics.*, 39:1433-1464, 10.1139/p61-172.

Baker, D., E. Hones, P. Higbie and R. Belian [1981] Global properties of the magnetosphere during a substorm growth phase: A case study. *Journal of Geophysical Research*, 86(A11), 8941-8956.

Baker, D., E. W. Hones, R. Belian and P. Higbie [1982] Multiple-spacecraft and correlated riometer study of magnetospheric substorm phenomena. *Journal of Geophysical Research*, 87(A8), 61216136,.

Baker, D., T. Pulkkinen, V. Angelopoulos, W. Baumjohann and R. Mcpherron [1996] Neutral line model of substorms: Past results and present view. *Journal of Geophysical Research - Space Physics*, 101(A6), 12975-13010.

Bame, S. J., D. J. McComas, M. F. Thomsen, B. L. Barraclough, R. C. Elphic, J. P. Glore, J. T. Gosling, J. C. Chavez, E. P. Evans and F. J. Wymer [1993] Magnetospheric plasma analyzer for spacecraft with constrained resources. *Review of Scientific Instruments*, 64(4), 1026-1033.

Banks, P. [1966] Collision frequencies and energy transfer, electrons. *Planetary and Space Science*, 1085-1103.

Bartels, J., N. H. Heck and H. F. Johnston [1939] The three-hour range index measuring geomagnteic activity. *Terrestrial magnetism and atmospheric electricity*, 44(4), 411454, doi:10.1029/TE044i004p00411.

Basler, R. P. [1966] Annual variation of auroral absorption. *Journal of Geophysical Research*, 71(3), 982984, doi:10.1029/JZ071i003p00982.

Baumjohann, W., G. Paschmann and C. Cattell [1989] Average plasma properties in the central plasma sheet. *Journal of Geophysical Research - Space Physics*, 94(A6), 6597-6606.

Belenkaya, E. [1998] High latitude ionospheric convection patterns dependent on the variable imf orientation. *Journal of Atmospheric and Solar-Terrestrial Physics*, 60 (13), 1343-1354.

Belian, R. D., G. R. Gisler, T. Cayton and C. R. [1992] High-z energetic particles at geosynchronous orbit during the great solar proton event series of october 1989. *Journal of Geophysical Research - Space Physics*, 97(A11), 16,89716,906, doi:10.1029/92JA01139.

Berkey, F. [1968] Coordinated measurements of auroral absorption and luminosity using the narrow beam technique. *Journal of Geophysical Research, Space Physics*, 73(1), 319337, doi:10.1029/JA073i001p00319.

Bhuyan, K., S. Singh and P. Bhuyan [2002] Tomographic reconstruction of the ionosphere using generalized singular value decomposition. *Current Science*, 83:1117–1120.

Birkeland, K. [1908] *The Norwegian aurora polaris expedition, 1902-1903.* H. Aschehoug & Co.

Bowles, K. L. [1958] Observations of vertical incidence scatter from the ionosphere at 41 mc/sec. *Physical Review Letters*, vol. 1, pp. 454-455.

Brovosky, J. and M. Denton [2006] Differences between cme-driven storms and cir-driven storms. *Journal of Geohpysical Research*, 111, A07S08, doi:10.1029/2005JA011447.

Brown, R., H. T.R., B. Landmark, H. Leinbach and J. Ortner [1961] Large scale electron bombardment of the atmosphere at the sudden commencement of a geomagnetic storm. *Journal of Geophysical Research*, 66(4), 1035-1041.

Browne, S., J. K. Hargreaves and B. Honary [1995] An imaging riometer for ionospheric studies. *Electronics and Communication Engineering Journal*, ISSN 0954–0695. 7(5), 209–217.

Campbell, W. H. [2004] Failure of dst index fields to represent a ring current. *Space Weather*, 2, S08002, doi:10.1029/2003SW000041.

Carpenter, D. [1963] Whistler evidence of a knee in the magnetospheric ionization density profile,. *Journal of Geophyiscal Research*, 68(6), 1675-1682.

Carpenter, D. [1970] Whistler evidence of the dynamic behavior of the duskside bulge in the plasmasphere. *Journal of Geophyiscal Research*, 75(19), 3837-3847.

Chernouss, S., V. R. Tagirov, M. A. Chernouss, J. Kangas, J. Leinonen and M. Kivinen [1985] Auroral and magnetic pulsations in the morning sector of the auroral zone. *Geophysica*, vol(21), pp19-37.

Clilverd, M., R. C. J., R. M. Milan, J. G. Sample, M. Kokorowski, M. P. McCarthy, T. Ulich, T. Raita, A. J. Kavanagh and E. Spanswick [2007] Energetic particle precipitation into the middle atmosphere triggered by a coronal mass ejection. *Journal of Geophysical Research - Space Physics*, 112:A12206, doi:10.1029/2007JA012395.

Clilverd, M. A., C. J. Rodger, N. R. Thomson, J. B. Brundell, T. Ulich, J. Lichtenberger, N. Cobbet, A. B. Collier, F. W. Menk, A. Seppala, P. T. Verronen and E. Turunen [2009] Remote sensing space weather events: Antarctic-arctic radiation-belt (dynamic) deposition-vlf atmospheric research knosortium network. *Space Weather*, S04001, doi:10.1029/2008SW000412.

Clilverd, M. A., C. J. Rodger and T. Ulich [2006a] The importance of atmospheric precipitation in storm-time relativistic electron flux drop outs. *Geophysical Research Letters*, 33, L01102, doi:10.1029/2005GL024661.

Clilverd, M. A., C. J. Rodger, T. Ulich, A. Seppala, E. Turunen, A. Botman and N. R. Thomson [2005] Modeling a large solar proton event in the southern polar cap,. *Journal of geophysical research*, 110, A09307, doi:10.1029/2004JA010922.

Clilverd, M. A., A. Seppl, C. J. Rodger, P. Verronen and N. R. Thomson [2006b] Ionospheric evidence of thermosphere-to-stratosphere descent of polar nox. *Geophysical Research Letters*, 33, L19811, doi:10.1029/2006GL026727.

Cliver, E. W., L. Svalgaard and A. G. Ling [2004] Origins of the semiannual variation of geomagnetic activity in 1954 and 1996. *Annales Geophysicae*, vol. 22, Issue 1, pp.93-100.

Collis, P. and J. Hargreaves [1997] Co-ordinated studies using imaging riometer and incoherent scatter radar. *Journal of atmospheric and solar-terrestrial physics*, 59(8):873–890.

Constable, S., R. Parker and G. Constable [1987] Occams inversion: A practical algorithm for generating smooth models from electromagnetic sounding data. *Geophysics*, 52(3):289–300.

Coroniti, F. V. and C. Kennel [1970] Electron precipitation pulsations. *Journal of Geophyiscal Research - Space Physics*, 75(7), 12791289, doi:10.1029/JA075i007p01279.

Dalagarno, A. and R. Henry [1965] Electron temperatures in the d region. *Proceedings of the Royal Society of London, Series A, Mathematical and Physical Sciences,*, 288(1415):521–530.

Danilkin, N., P. Denisenko, B. Barabashov and G. Vertogradov [2005] Electron collision frequency and hf waves attenuation in the ionosphere. *International Journal of Geomagnetism and Aeronomy*, 5, GI3009, doi:10.1029/2004GI000081.

Davis, T. N. and M. Sugiura [1966] Auroral electrojet activity index ae and its universal time variations. *Journal of geophysical research.*, 71(3), 785801, doi:10.1029/JZ071i003p00785.

deGroot Hedlin, C. and S. Constable [1990] Occams inversion to generate smooth, two-dimensional models from magnetotelluric data. *Geophysics*, 55:1613–1624.

del Pozo, C., J. Hargreaves and A. Alyward [1997] Ion composition and effective recombination rate in the nighttime auroral lower ionosphere. *Journal of Atmospheric and terrestrial Physics*, 59:1919–1943.

Denton, M. H. and J. E. Borovsky [2008] Superposed epoch analysis of high-speed-stream effects at geosynchronous orbit: Hot plasma, cold plasma, and the solar wind. *Superposed epoch analysis of high-speed-stream effects at geosynchronous orbit: Hot plasma, cold plasma, and the solar wind*, 113, A07216, doi:10.1029/2007JA012998.

Detrick, D. and T. Rosenberg [1990] A phased array radiowave imager for studies of cosmic noise absorption. *Radio Science*, 25(4), 325–338. doi:10.1029/RS025i004p00325.

Devlin, T., J. Hargreaves and P. Collis [1986] Eiscat observations of the ionospheric d-region during auroral radio absorption events. *Journal of Atmospheric and terrestrial Physics*, 48:795–805.

Drevin, G. R. and P. H. Stoker [1990] Riometer quiet day curves determined by the maximum density method. *Radio Science*, 25:1159–1166.

Dungey, J. [1963] The structure of the exosphere or adventures in velocity space. *Geophysics, The Earth's Enviroment.*

Dungey, J. W. [1961] Interplanetary magnetic field and the auroral zones. *Physical Review Letters*, 47–48.

Evans, J. V. [1968] Theory and practice of ionosphere study be thomson scatter radar. *Proceedings of the IEEE*, vol 57. pp 496-530.

Ferguson, F. A. [1998] Computer programs for long wavelength radion communictations, version 2. *Technial Document.*

Forbes, T., J. M. Malherbe and E. Priest [1988] The formation of flare loops by magnetic reconnection and chromspheric avlation. *Solar Physics*, 120(2), 285-307.

Fougere, P. [1995] Ionospheric radio tomography using maximum entropy. i: Theory and simulation studies. *Radio Science*, 30:429–444.

Fraser, B. J., H. J. Singer, M. L. Adrian, D. L. Gallagher and M. F. Thomsen [2005] The relationship between plasma density structure and emic waves at geosynchronous orbit. *in Inner Magnetosphere Interactions: New Perspectives From Imaging, Geophys. Monogr. Ser*, vol. 159, edited by J. L. Burch, M. Schulz, and H. Spence, pp. 5570, AGU, Washington, D. C., doi:10.1029/159GM04.

Gonzalez, W., J. Joselyn, Y. Kamide, H. Kroehl, G. Rostoker, B. Tsurutani and V. Vasyliunas [1994] What is a geomagnetic storm? *Journal of Geophysical Research - Space Physics*, 99(A4), 5771-5792.

Gordon, W. E. [1958] Incoherent scattering of radio waves by free electrons with applications to space exploration by radar. *Proceedings of the IRE*, Vol. 46, pp 1824-1839, November 1958.

Grill, M. [June 2007] *Technological Advances in Imaging Riometry.* Ph.D. thesis, Lancaster University.

Grill, M., F. Honary, E. Nielsen, T. Hagfors, G. Dekoulis, P. Chapman and H. Yamagishi [2003] A new imaging riometer based on mills cross technique. In *7th International Symposium on Communication Theory and Applications. Ambleside, UK.*

Gubbins, D. [1974] Theories of the geomagnetic and solar dynamo. *Review of Geophysics*, 12(2), 137–154, doi:10.1029/RG012i002p00137.

Gubbins, D. and E. Herro-Bervera [2007] *Encyclopedia of geomagnetism and paleomagnetism.* Springer.

Gustavsson, B. [2000] *Three dimensional Imaging of Aurora and Airglow.* Ph.D. thesis, Swedish Institute of Space Physics, Kiruna.

Hargreaves, J., S. Browne, H. Ranta, A. Ranta, T. Rosenberg and D. Detrick [1996] A study of substorm-associated nightside spike events in auroral absorption using imaging riometers at south pole and kilpisjrvi. *Journal of Atmospheric and terrestrial Physics*, 59(8):853–872.

Hargreaves, J. and T. Devlin [1990] Morning sector electron precipitation events observed by incoherent scatter radar. *Jorunal of Atmospheric and Terrestrial Physics*, 52(3) 193-203.

Hargreaves, J. K. [1970] Conjugate and closely-spaced observations of auroral radio absorptioniv: The movement of simple features. *Planetary and Space Science*, Volume 18, Issue 12, pp 1691-1705.

Hargreaves, J. K. [1992] *The solar-terrestrial environment.* Cambridge University Press.

Heikkila, W. J. and J. D. Winningham [1971] Penetration of magnetosheath plasma to low altitudes through the dayside magnetospheric cusps. *Journal of Geophysical Research*, 6(4), 883891.

Henderson, M., G. Reeves, R. Belian and J. Murphree [1996] Observations of magnetospheric substorms occurring with no apparent solar wind/imf trigger. *Journal of Geophysical Research - Space Physics*, 101(A5), 10773-10791.

Heppner, J. and N. Maynard [1987] Empirical high-latitude electric field models. *Journal of Geophysical Research - Space Physics*, 92(A5), 4467-4489.

Hess, W. [1968] *Radiation Belt and Magnetosphere.* Blaisdell.

Holzer, T. [1979, p103] *Solar system plasma physics. Volume 1 - Solar and solar wind plasma physics.* Amsterdam, North-Holland Publishing Co.

Honary, F., P. Chapman, M. Grill, K. Barratt, S. Marple, E. Nielsen and T. Hagfors [2005] Advanced rio-imaging experiment in scandinavia (aries:) system specification and scientific goals. In *Proceedings of the URSI XXVIII General Assembly. New Delhi, India.*

Honary, F., S. Marple, K. Barratt, P. Chapman, M. Grill and E. Nielson [2011] Invited article: Digital beam-formin imaging riometer systems. *Review of Scientific Instruments*, 82, 031301.

Hones, E. [1984] Plasma sheet behaviour during substorms,. *Magnetic Reconnection in Space and Laboratory, American Geophysical Union Monograph 30, Washington,*, 178.

Horne, R. B. and R. M. Thorne [1998] Potential waves for relativistic electron scattering and stochastic acceleration during magnetic storms. *Geophysical Research Letters*, 25(15), 30113014, doi:10.1029/98GL01002.

Hsu, T. and R. McPherron [2004] Average characteristics of triggered and nontriggered substorms. *Journal of Geophysical Research - Space Physics*, 109, A07208, doi:10.1029/2003JA009933.

Hudson, H. S. [2010] Global properties of solar flares. *Space Science Reviews*, 158 (1), 5-41.

Iijima, T. and T. Potemra [1978] Large-scale characteristics of field-aligned currents associated with substorms. *Journal of Geophysical Research*, 83(A2), 599615, doi:10.1029/JA083iA02p00599.

Kavanagh, A., F. Honary, I. McCrea, E. Donovan, J. Woodfield, E.E. amd Manninen and P. Anderson [2002] Substorm related changes in precipitation in the dayside auroral zone a multi instrument case study. *Annales Geophysicae*, 20: 13211334.

Kavanagh, A., G. Lu, E. Donovan, G. Reeves, F. Honary, J. Manninen and T. Immel [2007] Energetic electron precipitation during sawtooth injections. *Annales Geophysicae*, 25:1199–1214.

Kavanagh, A., S. Marple, F. Honary, I. McCrea and A. Senior [2004a] On solar protons and polar cap absorption: constraints on an empirical relationship. *Annales Geophysicae*, 22: 11331147.

Kavanagh, A., J. A. Wild and F. Honary [2009] Observations of omega bands using an imaging riometer. *Annales Geophysicae*, 27 (11). pp. 4183-4195.

Kavanagh, A. J., M. Kosch, F. Honary, A. Senior, S. R. Marple, E. E. Woodfield and I. W. McCrea [2004b] The statistical dependence of auroral absorption on geomagnetic and solar wind parameters. *Annales Geophysicae*, 22:877–887.

Kennel, C. F. and H. Petschek [1966] Limit on stably trapped particle fluxes. *Journal of Geophysical Research*, 71(1), 128, doi:10.1029/JZ071i001p00001.

Kivelson, M. and C. Russell [1995] *Introduction to space physics.* Cambridge University Press.

Krishnaswamy, S., D. L. Detrick and T. J. Rosenberg [1985] The inflection point method of determining riometer quiet day curves. *Radio Science*, 20:123–136.

Kusano, K., T. Maeshiro, T. Yokoyama and T. Sakurai [2004] The trigger mechanism of solar flares in a coronal arcade with reversed magnetic shear. *The Astrophysical Journal*, 610:537-549.

Lemaire, J. [1982] A brief panorama. *Advance in Space Research*, 2, 3.

Little, C. and H. Leinbach [1958] Some measurements of high-latitude ionospheric absorption using extraterrestrial radio waves. In *Proceedings of the IRE.*

Little, C. G. and H. Leinbach [1959] The riometer-a device for the continuous measurement of ionospheric absorption. *Proceedings of the IRE*, 47(2), 315–320.

Longden, N., M. H. Denton and F. Honary [2008] Particle precipitation during icme-driven and cir-driven geomagnetic storms. *Journal of Geophysical Research - Space Physics,*, 113, A06205, doi:10.1029/2007JA012752.

Lui, A. [1991] A synthesis of magnetospheric substorm models. *Journal of Geophysical Research - Space Physics*, 96(A2), 18491856, doi:10.1029/90JA02430.

Lui, A. [2000] Tutorial on geomagnetic storms and substorms. *Plasma Science, IEEE Transactions on*, 28 (6), 1854-1866.

Lyons, L., G. Blanchard, J. Samson, R. Lepping, T. Yamamoto and T. Moretto [1997] Coordinated observations demonstrating external substorm triggering. *Journal of Geohpysical Research - Space Physics*, 102(A12), 27,03927,051, doi:10.1029/97JA02639.

Maeda, K. [1977] Conductivity and drifts in the ionosphere. *Journal of Atmospheric and Solar-Terrestrial Physics*, 39(9-10) 1041-1053.

Marple, S. and F. Honary [2004] A multi-instrument data analysis toolbox. *Advances in Polar Upper Atmosphere Research*, ISSN 1345-1065(18):120–130.

Mcllwain, C. E. [1961] Coordinates for mapping the distribution of magnetically trapped particles. *Journal of Geophysical Research*, 66(11), 36813691, doi:10.1029/JZ066i011p03681.

Menvielle, M. and A. Berthelier [1991] The k-derived planetary indices: Description and availability. *Reviews of geophysics*, 29(3), 415432, doi:10.1029/91RG00994.

Meridth, N. P., R. M. Thorne, R. Horne, D. Summers, B. Fraser and R. Anderson [2003] Statistical analysis of relativistic electron energies for cyclotron resonance with emic waves observed on crres. *Journal of Geophysical Research*, 108, 1250, doi:10.1029/2002JA009700.

Millan, R., L. R.P. and S. D.M. [2002] X-ray observations of mev electron precipitation with a balloon-borne germanium spectrometer. *Geophysical Research Letters*, 29(24), 2194, doi:10.1029/2002GL015922.

Morley, S. K., S. T. Ables, M. D. Sciffer and B. Fraser [2009] Multipoint observations of pc1-2 waves in the afternoon sector. *Journal of Geophysical Research - Space Physics*, 114, A09205, doi:10.1029/2009JA014162.

Nose, M., T. Iyemori, M. Takeda, T. Kameri, D. K. Milling, D. Orr, H. Singer, E. Worthington and N. Sumitomo [1998] Automated detection of pi 2 pulsations using wavelet analysis: 1. method and an application for substorm monitoring. *Earth Planets Space*, vol 50, pp 773-783.

Olsen, W. P. [1982] The geomagnetic field and its extension into space. *Advances in Space Research*, vol. 2, no. 1, 1982, p. 13-17.

Ortner, J., B. Hultqvist, R. Brown, T. Hartz, O. Holt, B. Landmark, J. Hook and H. Leinbach [1962] Cosmic noise absorption accompanying geomagnetic storm sudden commencements. *Journal of Geophysical Research*, 67(11), 41694186.

Osepian, A. and S. Kirkwood [2004] Cosmic radio-noise absorption bursts caused by solar wind shocks. *Annales Geophysicae*, 22: 29732987.

Osepian, A., S. Kirkwood and N. Smirnova [1996] Energetic electron precipitation during auroral events observed by incoherrent scatter radar. *Advance in Space Research*, 17:149–115.

Parker, E. N. [1958] Dynamics of the inerplanetary gas and magnetic field. *Astrophysical Journal*, 128, 664-676.

Perrone, L., L. Alfonsi, V. Romano and G. Franceschi [2004] Polar cap absorption events of november 2001 at terra nova bay, antarctic. *Annales Geophysicae*, 22: 16331648.

Piel, A. [2010] *Plasma Physics: An Introduction to Laboratory, Space, and Fusion Plasmas.* Springer.

Potemra, T., L. Zanetti, P. Bythrow, A. Lui and T. Iijima [1984] By dependent convection patterns during northward interplanetary magnetic field. *Journal of Geophysical Research - Space Physics*, 89(A11), 9753-9760.

Ranta, H. and A. Ranta [1977] Daily variation of absorption in the d-region using riometer data at high latitudes. *Journal of Atmospheric and Solar-Terrestrial Physics*, 309-312.

Ranta, H., A. Ranta, J. Hargreaves and S. Browne [1997] Localized absorption events in the afternoon sector. *Journal of Atmospheric and terrestrial Physics*, 59:891–902.

Ratcliffe, J. A. [1959] *The magneto-ionic theory and its applications to the ionosphere.* Cambridge University Press.

Rees, M. [1963] Auroral ionization and excitation by incident energetic electrons. *Planetary and Space Science*, 11(10), 1209-1218.

Rees, M. [1989] *Physics and chemistry of the upper atmosphere.* Cambridge University Press.

Reid, G. [1974] Polar-cap absorption - observations and theory. *Fundamentals of Cosmic Physics*, 1(3), 167-200.

Rishbeth, H. and A. van Eyken [1993] Eiscat: early history and the first ten years of operation. *Journal of Atmospheric and Terrestrial Physics*, 55:525–542.

Rishbeth, H. and P. J. S. Williams [1985] The eiscat ionoshperic radar: The system and its early results. *Royal Astronomical Society, Quarterly Journal*, vol 85. pp 478-512.

Ritchie, S. and F. Honary [2009] Observed characteristics of sudden commencement absorption. *Journal of Atmospheric and Solar-Terrestrial Physics*, 71 (5):609–617. ISSN 1364–6826.

Rodger, T., C.J.and Raita, M. A. Clilverd, A. seppala, S. Dietrich and N. R. a. Thomson [2008] Observations of relativistic electron precipitation from the radiation belts driven by emic waves. *Geophysical Research Letters*, 35, L16106, doi:10.1029/2008GL034804.

Roederer, J. [1970] *Dynamics of Geomagnetically Trapped Radiation.* Springer.

Russell, C. [1974] On the heliographic latitude dependence of the interplanetary magnetic field as deduced from the 22-year cycle of geomagnetic activity. *Geophysical Research Letters*, Vol 1, No 1.

Russell, C. [1999] Polar eyes of the cusp. *Cluster-II Workshop: Multiscale/Multipoint Plasma Measurements, Proceedings of the Workshop held at Imperial College, London, UK,*, 47–55.

Schunk, R. and A. Nagy [1978] Electron temperatures in the f-region of the ionosphere: Theory and observations. *Journal of geophysics and space physics*, 335–397.

Schunk, R. W. and A. Nagy [2000] *Ionospheres, Physics, Plasma Physics, and Chemistry.* Cambridge University Press.

Sellers, B., F. Hanser, M. Stroscio and G. Yates [1977] The night and day relationships between polar cap riometer absorption and solar protons. *Radio Science*, 12(5), 779-789.

Semeter, J. and F. Kamalabadi [2005] Determination of primary electron spectra from incoherent scatter radar measurements of the auroral e region. *Radio Science*, 40(RS2006):doi:10.1029/2004RS003042.

Semeter, J. and M. Mendillo [1997] A nonlinear optimization technique for ground-based atmospheric emission tomography. *Geoscience and Remote Sensing, IEEE Transactions on*, 35:1105–1116.

Senior, A., A. Kavanagh, M. Kosch and F. Honary [2007] Statistical relationships between cosmic radio noise absorption and ionospheric electrical conductances in the auroral zone. *Journal of Geophysical Research*, 112, A11301, doi:10.1029/2007JA012519.

Shirley, J. and R. Fainbridge [1997] *Encyclopedia of Planetary Sciences.* Chapman and Hall, New York.

Smets, R., D. Delcourt, G. Chanteur and T. Moore [2002] On the incidence of kelvin-helmholtz instability for mass exchange process at the earths magnetopause. *Annales Geophysicae*, 20, 757-769, doi:10.5194/angeo-20-757-2002.

Solanki, S. K., B. Inhester and M. Schussler [2006] The solar magnetic field. *Reports on Progress in Physics*, 69(3), 562-668.

Stauning, P. [1996] Investigations of ionospheric radio wave absorption processes using imaging riometer techniques. *Journal of Atmospheric and Terrestrial Physics*, 58:753–764.

Stauning, P. and T. J. Rosenberg [1996] High-latitude daytime absorption spike events. *Journal of Geophysical Research*, 101(A2), 23772396, doi:10.1029/95JA03125.

Steen, r., U. Brändström, B. Gustavsson and T. Aso [1997] Alis- a multi-station imaging system at high latitudes with multi-disciplinary scientific objectives. *European Rocket and Balloon Programmes and Related Research, Proceedings of the 13th ESA Symposium in Öland, Sweden.*

Stone, E. C., A. M. Frandsen, R. A. Mewoldt, E. R. Christian, D. Margolies, J. F. Ormes and F. Snow [1998] The advanced composition explorer. *Space Science Reviews*, 86, 1.

Tanskanen, E. I. [2009] A comprehensive high-throughput analysis of substorms observed by image magnetometer network: Years 19932003 examined. *Journal of Geophysical Research, Space Physics*, 114, A05204, doi:10.1029/2008JA013682.

Terkildsen, M., B. Fraser, F. Menk and R. Morris [2001] Imaging riometer observations of absorption patches accosiated with magnetic impluse events. *ANARE Reports*, No. 146. 165180.

Terkildsen, M., B. Fraser and H. Yamagishi [2004] Determination of the altitude peak of cosmic noise absorption using a vertical parallax technique. *Geophysical Research Letters*.

Tobias, S. M. [2002] The solar dynamo. *Philosophical Transactions of the Royal Society*, 360, 2741-2756, doi:10.1098/rsta.2002.1090.

Van Allen, J. A. [1959] The geomagnetically trapped corpuscular radiation. *Journal of Geophysical Research*, 64(11), 16831689, doi:10.1029/JZ064i011p01683.

Vasyliunas, V. M. [1983] Large-scale morphology of the magnetosphere. *Solar-terrestrial physics: Principles and theoretical foundations; Proceedings of the Theory Institute, Chestnut Hill, MA, August 9-26,*, 243–254.

Vickrey, J. F., R. R. Vondrak and S. J. Mathews [1982] Energy deposition by precipitating particles and joule dissipation in the auroral ionosphere. *Journal of Geophysical Research*, 87(A7):5184–5196.

Wanliss, J. A. and K. M. Showalter [2006] High-resolution global storm index: Dst versus sym-h. *Journal of geophysical research - space physics*, 111, A02202, doi:10.1029/2005JA011034.

Yohsuke, K. and C. Abraham [2007] *Handbook of the Solar-Terrestrial Environment*. Springer.

Zhang, M. and B. C. Low [2005] The hydromagnetic nature of solar coronal mass ejections. *Annual Review of Astronomy and Astrophysics*, 43:103-137.

Zhou, X. W., C. T. Russell, G. Le, S. A. Fuselier and J. D. Scudder [2000] Solar wind control of the polar cusp at high altitud. *Journal of Geophysical Research - Space Physics*, 105(A1), 245251, doi:10.1029/1999JA900412.